Dipartimento di / Department of

Chemistry

Dottorato di Ricerca in / PhD program Chemical Sciences and Technology   Ciclo / Cycle XXXI

Curriculum in (se presente / if it is) Chemistry

Development of Reliable Experimental Models for the Study of the Biological Behavior of Drug Nanocarriers

Cognome / Surname   Rotem   Nome / Name   Rany

Matricola / Registration number   802712

Tutore / Tutor: Prof. Davide Prosperi

Cotutore / Co-tutor: Dr. Miriam Colombo

Coordinatore / Coordinator: Prof. claudio Greco
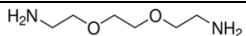
ANNO ACCADEMICO / ACADEMIC YEAR   2017/18

Table of Contents

Abstract

The curative effectiveness of current and new drugs is often limited by poor pharmacokinetics in-vivo. The use of nanoparticles as drug carriers seems promising in solving this problem. In this work we aimed to further explore and improve common drug delivery components and techniques. Starting with the synthesis of nanoparticles with a controlled number of molecular recognition ligands, we used bulky ligands and gel separation to obtain nanoparticles with a discrete number of chemical functional groups, used later to conjugate the same number of molecular recognition ligands. These nanoparticles later showed substantial difference in the *in-vivo* behavior. A second project focused on the in-depth characterization of the relationship between hydrophobic inorganic nanoparticles and the polymer surfactants used to enable their water dispersibility, as well enabling their functionalization. This investigation was done through separate quantification of polymer and inorganic nanoparticles and assessment of stability. Our results showed that the removal of excess polymer from such systems can result in loss of colloidal stability. A third project was aimed to describe the mechanism of polymeric nanoparticle's endosomal escape and provide a platform for qualitative investigation and enhancement of this process. This goal was accomplished through two complementary *in-vitro* experiments testing two proposed mechanisms of endosomal escape. These results raised a key consideration when matching a particle capable of endosomal escape to a specific cell type as well as methods reduce interaction with serum proteins. A fourth project focused on developing an assay to quantify cytosolic delivery of nanoparticles and theoretically assessed the possibility of using fluorescence resonance energy transfer (FRET) - which was found to be not practical in this case - as well as implementing a pro-fluorophore to generate a measurable signal. Our preliminary results indicate this method might indeed be useful for this purpose in the future.

Abbreviations

Abbreviations	Meaning	Formula / comment
NP, NPs	Nanoparticle, nanoparticles	
Ab, Abs	Antibody, Antibodies	
nm	Nanometer	10^{-9} meter
#d, 1d, 2d	Number of dimensions	
E+	Exponent	$*10^{\wedge}$
UV	Ultra-violate light	
AO, MO	Atomic orbital, molecular orbital	
HOMO	Highest occupied molecular orbital	
LUMO	Lowest unoccupied molecular orbital	
TEM	Transmission electron microscopy	
PMA	Poly(isobutylene-*alt*-maleic anhydride)	
HRTEM	High resolution TEM	
DLS	Dynamic light scattering	
PBS	Phosphate buffered saline	
EDBE	Ethylenedioxy bis(ethylamine)	
BFP	Blue fluorescent protein	
THF	tetrahydrofuran	
PEG	Poly ethylene glycol	
EDC	N-(3-Dimethylaminopropyl)-N'-ethylcarbodiimide	
TBE buffer	Tris/Borate/EDTA buffer	
MOPS buffer	(3-(N-morpholino)propanesulfonic acid)	
FBS	Fetal Bovine Serum	
RCF	Relative centrifugal force	
RBC	Red blood cell	
RPM	Rounds per minute	
FACS	Fluorescence activated cell sorting	

Chapter 1: Introduction

The aim of this work was to advance the use of nanomaterials as drug delivery agents. We focused on two systems, namely – Poly(isobutylene-alt-maleic anhydride) (PMA) polymer micelles for cytoplasmic delivery and functionalized gold NPs for tumor tissue penetration. Accordingly, the following introduction will cover three main topics: "Synthesis and properties of nanomaterials", "Challenges of drug delivery" and "Application of NPs in medicine". The first part will focus on preparation methods of nanomaterials and their relevant properties; the second part will discuss current challenges and limitations of current drugs and treatments; and the last part will introduce the application of nanomaterials to improve current treatment methods in medicine.

1.A - Synthesis and properties of nanomaterials

A nanomaterial can be defined as any material, having at least one dimension limited to the range of 1-1000nm, i.e. thin sheets (2D), wires (1D) or spheres (0D). A second definition could be materials whose intrinsic properties change as function of the material size[1,2]. These changes originate from a transition between individual atoms to bulk material, quantum confinement of free electrons, or a change in the surface area to volume ratio of a crystal[2,3] (Figure 1, left). In relation to biology, nanomaterials are important because they are the right size to infiltrate and interact with biological systems[4,5] (i.e., similar size as proteins. Figure 1, right). Examples for size-property dependence include increase in catalytic activity, melting point, magnetism, change in color of absorption and emission, and electrical conductivity[2,3,6].
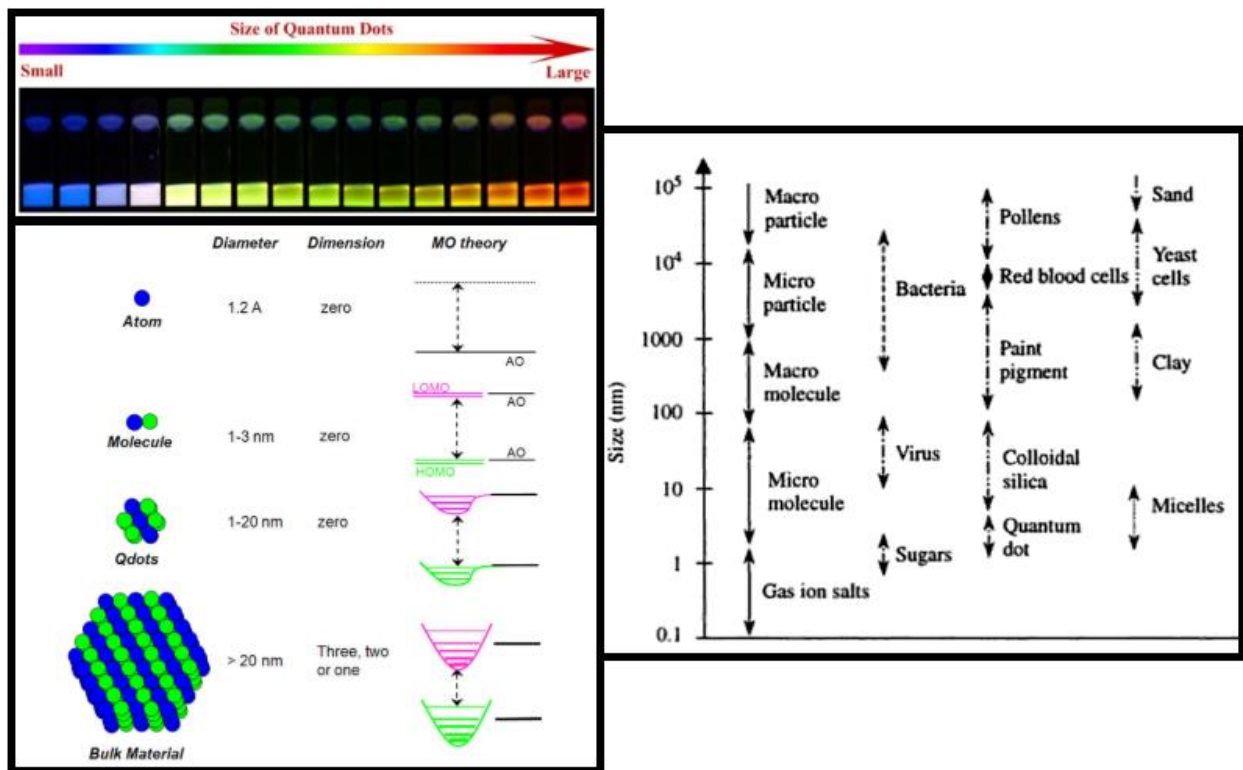
Figure 1: (top left) A series of Cadmium Selenide quantum dots of different sizes illuminated by UV lamp. As the quantum dots become smaller, their fluorescence emission frequency gets shorter, due to quantum confinement[3]. (bottom left) An illustration of the change in electronic orbitals through the transition from single atoms to bulk matter. As atoms come together they share atomic orbitals of identical discreet energy, to form an array of molecular orbitals of varying energy. These changes are evident in the electronic properties of the particle, such as optical and electrical[3]. (right) typical size range of different materials[2].

Nanomaterials can be divided into organic and inorganic materials (Figure 2). Organic nanomaterials include liposomes, micelles, dendrimers, nano-wires, monolayers, molecular machines, and some use biological materials such as DNA[7–13]. These materials are often prepared using a bottom-up approach, utilizing specific chemical groups and organic chemistry reactions. Inorganic nanomaterials are made of materials such as silica[14], gold[15], cadmium selenide[16] and different carbon allotropes[17] (e.g., nanotubes, nanodiamonds), and come in all shapes and dimensions[16,18–20].

A big challenge in the synthesis of nanomaterials is the preparation of a large quantity of material, while avoiding variability between particles, and controlling frequency of structural defects[21–26]. This if frequently achieved using bottom-up self-assembly methods. Different mechanism have been described for the nucleation and growth of NPs[27]. One example is the LaMer mechanism (Figure 3, left). First, monomer concentration in solution is sharply increased above a critical concentration that allows NP nucleation. This fast nucleation consumes enough monomer to reduce the concentration below the critical concentration, stopping new nuclei formation. Existing nuclei continue to grow, consuming the monomer until its concentration reaches the solubility limit. The separation between nucleation and growth is explained by the crystal free energy as function of its size, compared to the monomers at concentration below

$C_{critical}$ (Figure 3 ,right). At this concentration the formation of new nuclei is hindered by an energy barrier, however the growth of existing NPs is still favorable.
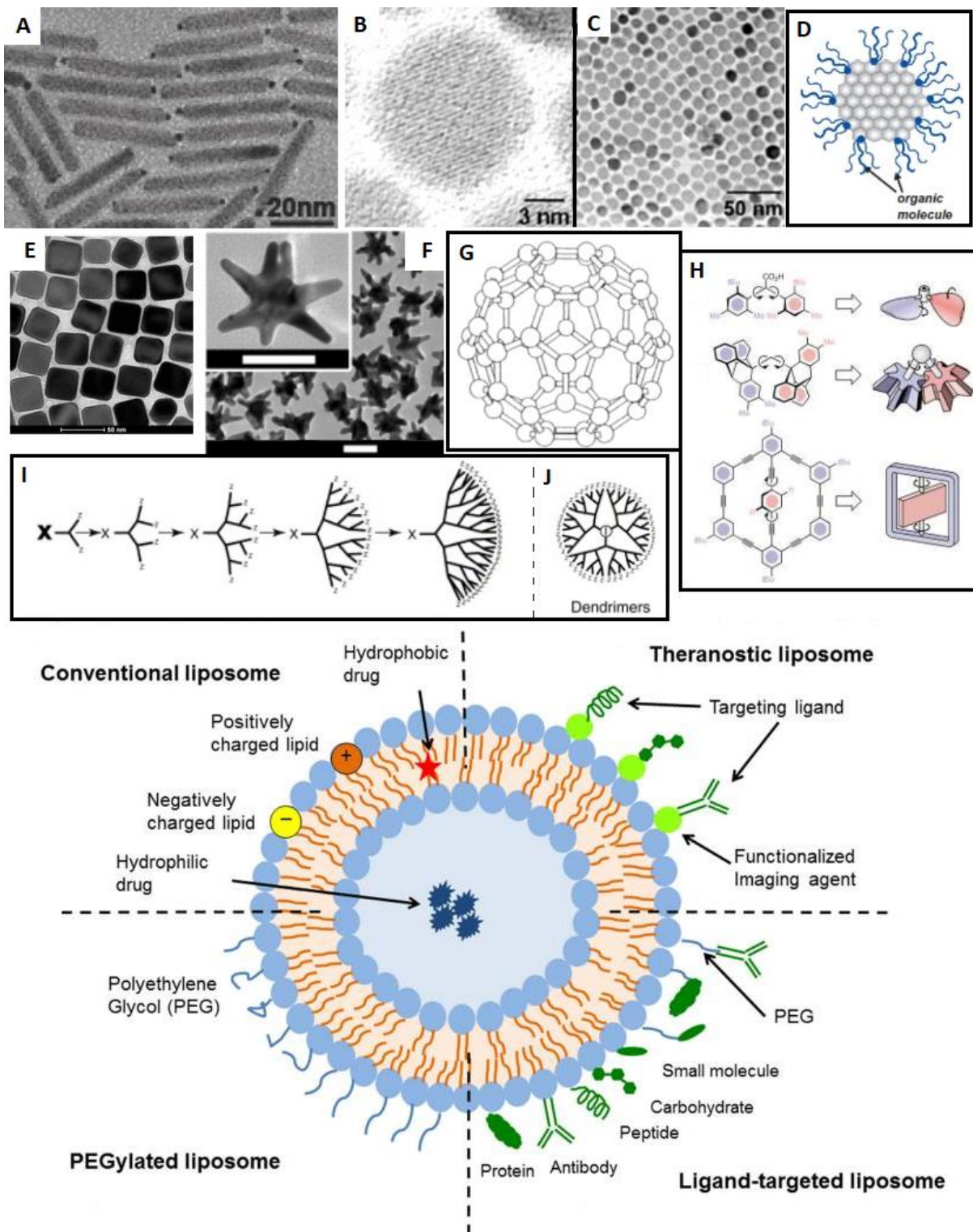

Figure 2: (A) TEM images showing cadmium sulfide quantum rods bearing a gold tip[16]. (B and C) TEM and HRTEM images of In₂O₃ nanocrystals[28]. (D) a schematic depiction of an inorganic nanoparticle stabilized by organic ligands on its surface[3]. (E)

TEM image of silver nanocubes (scale bar=50 nm)[20]. (F) TEM image of gold nanostars (both scale bars=50 nm)[19]. (G) ball and stick model of fullerene, C_{60}, one of carbon's allotropes[29]. (H) molecular structure and corresponding cartoon of three molecular machines[30]. (I and J) A cartoon of the structure and the stepwise growth of a dendrimer[8]. (bottom) A cartoon of a liposome consisting of aggregated surfactant molecules, different possibilities for drug loading and different surface modifications aimed to modify the construct's pharmacokinetics and allow it's imaging[10].
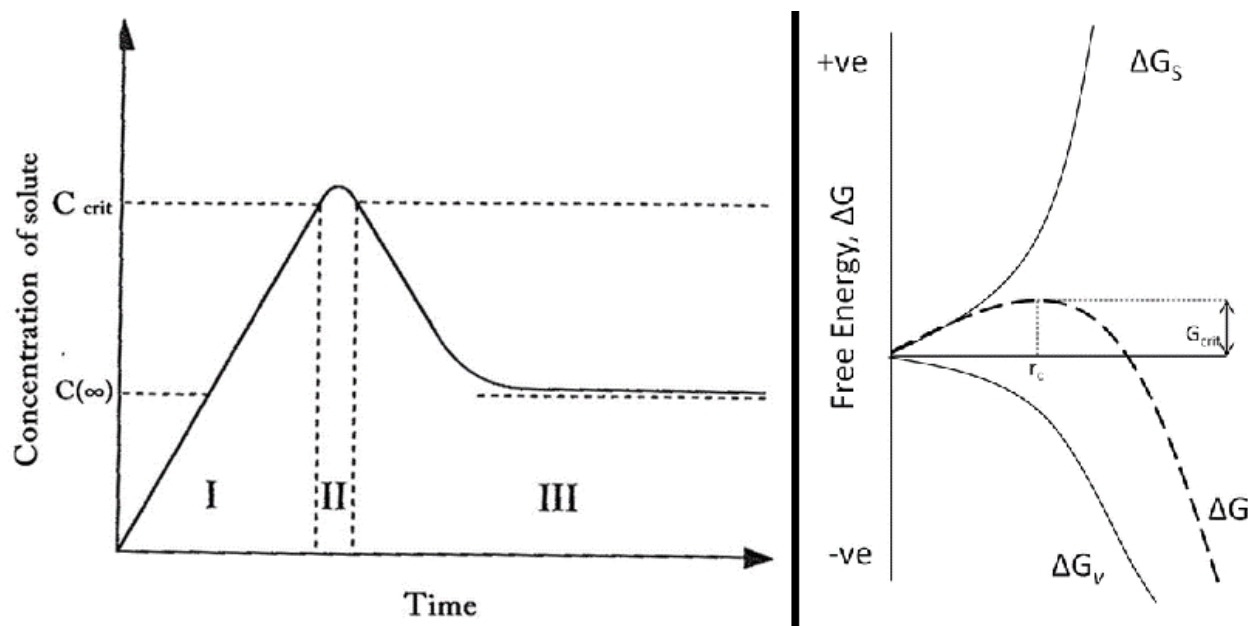

Figure 3: (left) A schematic graph describing different phases in the synthesis of monodisperse NPs, as described by LaMer[27]. In phase 1, monomer concentration increases above a critical concentration C_{crit} that allows nucleation. This nucleation in phase 2 quickly consumes the monomers and lowers their concentration below C_{crit}, thus stopping the creation of new NPs. In phase 3, existing nuclei grow, further consuming the monomers until they reach the solubility limit. the limitation of nucleation time yields a narrow size distribution within the NP population. (right) at monomer concentration below C_{crit}, the free energy of monomer crystallization as function of crystal size is given by both bulk volume (negative) and surface (positive) free energies. This result in a free energy barrier that prevents nucleation, while allowing growth of NPs above a critical size.

To prevent aggregation of the NPs and to lower its surface energy the NPs surface is usually covered by a surfactant (surface ligands, Figure 2, D)[31]. Such materials can also dictate anisotropic growth of the NP[32], and influence its electronic band structure[33]. As many methods for NP synthesis utilize organic solvents, the resulting NPs are often hydrophobic (or stabilized with hydrophobic ligands); a method is therefore needed to create a stable suspension of these NPs in aqueous solutions. Conceptually, it is possible to either replace the surface ligands (ligand exchange[34–36]) or add a hydrophilic component on top of them (polymer coating[36,37]). In both cases, ionizable chemical groups are frequently used, generating a net surface charge and measurable zeta potential that helps stabilizing the NP suspension[38,39]. The same chemical groups can also be used to chemically bind different molecules to the NP's surface (Figure 2, bottom)[10,15,40].

Applying the capacity for design and synthesis of nanomaterials to biology is appealing, both for the unique properties of these materials as well as their appropriate size for interaction with biological components. This will be discussed in part 1.c.

1.B - Challenges of drug delivery

For a drug-based treatment to be effective, the drug must have an impact on a specific tissue or group of cells in the body. To do so, it must usually interact with a localized therapeutic site, e.g., an enzyme, a receptor or a transcription factor. Different methods are used to screen different molecules for desirable interactions directly with such targets; in the level of the protein, the cell or the tissue, in vitro and in silico (Figure 4)[41–44]. These methods allow fast testing of a large number of compounds but lack the context of the entire organism.
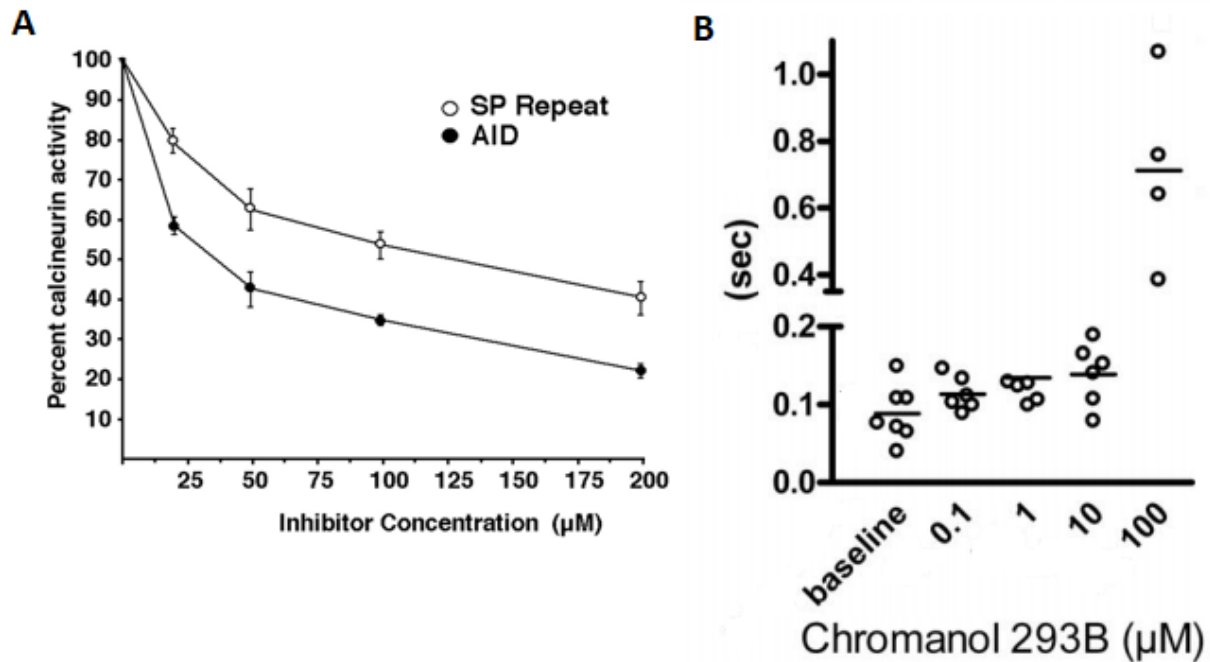

Figure 4: Examples for dose-response profiles. (A) the inhibition of the enzyme calcineurin as function of two peptide inhibitors, tested in vitro[42]. (B) the effect of chromanol 293B on the contraction time of engineered heart tissue grown in vitro. In these systems the drug effect is tested locally, without the context of the entire organism and the administration route.

There are different ways to introduce a drug into the body of the whole organism. The first contact point can be the skin, the eyes, the respiratory system, the digestion system and by injection into the blood stream or the tissue, among others[45–48]. The approval of a new drug for clinical use dictates a specific administration method, as different methods can drastically influence the drug pharmacokinetics, i.e., the drug diffusion, accumulation and clearance as function of time in different tissues. Thus, different administration method can impact both the drug efficacy and side effects[47]. For example, oral administration of a contraception would have a drastically different effect compared to vaginal administration[49,50]. Likewise, administration of antibiotics systemically would be different from topical administration[51].

From the administration point to the therapeutic site the drug must travel through the body, crossing different biological barriers while avoiding degradation or uptake by off target sites[52]. Drugs administered through the gastrointestinal tract, for example, need to survive the degradative environment of the stomach, and cross the mucus layer and endothelial cells in the

intestine before reaching the blood stream[53]. Once in the blood stream, a drug is distributed throughout the body, penetrating different tissues as function of localized blood flow, its ability to cross the blood vessels and diffuse through the tissue, as well as its hydrophobicity/hydrophilicity, pH sensitivity, and other high affinity interactions (e.g., binding to plasma proteins)[54–56]. Different barriers can further hinder desired delivery to specific targets, such as the blood-brain barrier, or - specifically important for this work - the plasma membrane for intracellular delivery. This non-ideal distribution (ideal would be exclusive delivery to the desired site) can lead to both side effects and low efficacy[52].

The term "clearance" describes the rate at which a drug is eliminated from the body, by metabolism or secretion (Figure 5). The major site for drug metabolism is the liver (and to some extent in all tissues[57]); specific molecules such as nucleic acid and peptides can be hydrolyzed by blood hydrolytic enzymes[58,59]. Excretion routes include the urine, feces, sweat and breast milk[54,55]. Endogenous materials such as native proteins have a typical blood half-life in the order of days; a modified or denatured protein (like other foreign bodies) can have a blood half-life in the order of minutes[60].
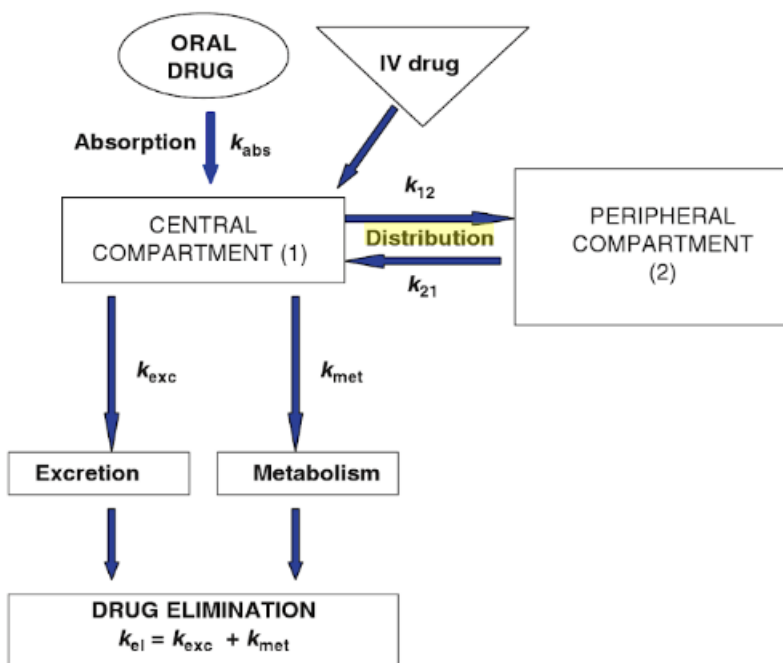
Figure 5: The two compartment model for the pharmacokinetics of drugs[54]. The "central compartment" represents the blood while the "peripheral compartment" can be any other tissue, such as bone, fat, or muscle. After reaching the blood the drug is reversibly distributed between the blood and different tissues, while being metabolized and excreted at the same time. Each process can be described by a rate constant.

Having tools for high throughput screening of different molecules enable the discovery of many new possible therapeutics, however, most of them fail to be efficiently delivered to the target site[52]. The incorporation of drugs into nanoconstructs improved this in some cases, by improving bioavailability for drugs with low solubility, increasing blood circulation time[61,62]

and improve the drug biodistribution profile[63]. The next part of the introduction will discuss the use of nanoparticles in biological systems and specifically for drug delivery.

1.C - Application of nanoparticles in medicine

The motivation to use nanomaterials in biological applications originates both from the unique size dependent properties of specific materials (e.g., quantum dots as fluorophores[64], gold NPs as energy-transducing agents for hyperthermia[65]), as well as having a size large enough to allow complexity and small enough to infiltrate the body (Figure 1, right). Such constructs can have a unique interaction and behavior in the body[52], which is both a blessing (enabling new therapeutics and diagnostics) and a curse (demanding thorough understanding and design).

1.C.i – the protein corona: many NPs are characterized by high surface energy originating from high magnitude surface charge and hydrophobic surface. When these NPs are introduced into a biological environment such as blood or the interstitial fluid, they meet a variety of macromolecules that can be adsorbed onto the NP's surface, reducing the total free energy[66,67]. This "corona" made mostly of proteins (hence "protein corona") was found to affect the NP's interaction and fate in vitro and in vivo (Figure 6), in terms of blood circulation time, biodistribution, cellular uptake, and intracellular localization[68]. This effect can be mediated by the modification of the NP's physical-chemical properties or by specific interaction with the corona biomolecules.

The formation of a biomolecular corona can be followed by the increase in NP's diameter as measured by differential centrifugal sedimentation and DLS, and a reduced zeta potential. Different publications describe the characterization of the specific constituent of the corona using gel electrophoresis and mass spectroscopy, allowing identification of specific proteins[69,70]. The structure of the corona on individual NPs seems random in terms of protein orientation and conformation[71]. The identity of the biomolecules changes as function of the physical and chemical properties of the NPs, and the biological fluid and its concentration, among other factors[67,68].

NPs can be designed to minimize biomolecule binding by using zwitterionic surface ligands and maintaining a low magnitude of zeta potential[72,73]. Another method to minimize the corona effect is modification of the NP's surface with uncharged, highly hydrophilic polymers, such as poly (ethyleneglycol) (PEG).
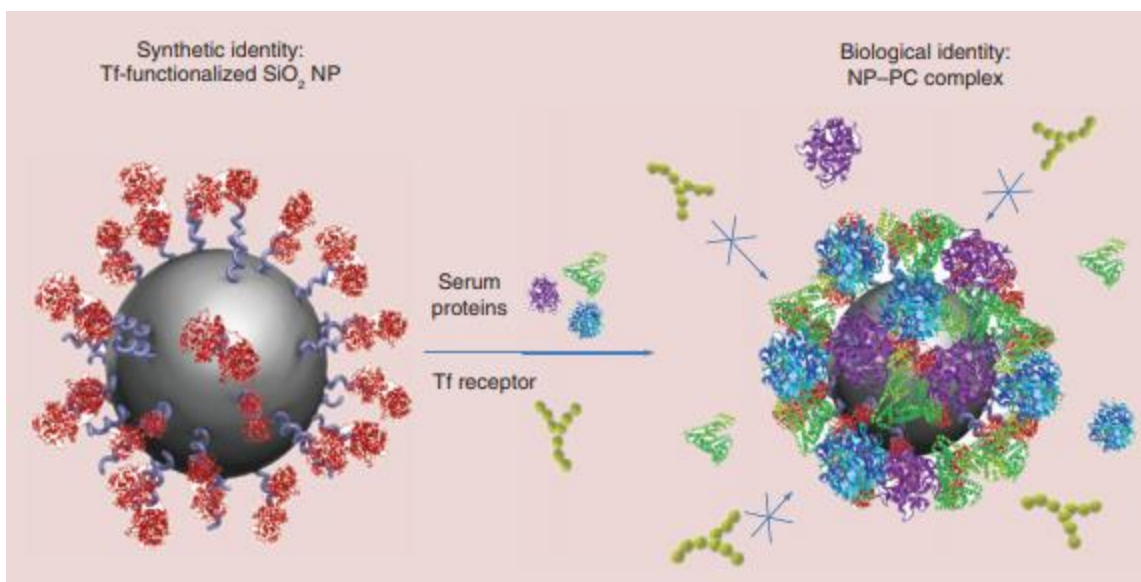
Figure 6: the impact of the protein corona on NP's interaction in the biological system. A NP is synthesized and functionalized with specific ligands (in the image – transferrin), however the formation of the protein corona masks the original surface and prevent molecular recognition as intended (in the image, no recognition by transferrin receptor)[67].

1.C.ii – Nanoparticle's pharmacological distribution depends on its physical characteristics: The main promise of NPs for drug delivery is the ability to control the drug biodistribution and kinetics. NPs circulating the blood stream are distributed to different tissues according to their ability to extravasate from the blood vessels and diffuse within the extracellular matrix – both depend on NP's size. Extravasation can be accomplished mostly exploiting the space between endothelial cells making the capillaries (later discussed – transcytosis). Large gaps between endothelial cells are called fenestrae. Most healthy tissues have non- fenestrated capillaries, thus limiting penetration of NPs bigger than a few nanometers. Different tissues have different fenestration size, allowing different extravasation kinetics as function of NP's size (Figure 7)[52,73–75]. Accordingly, NPs smaller than 5 nm can pass through kidney fenestration and are rapidly cleared from the blood by renal filtration. Bigger NPs have a longer circulation time and can penetrate other tissues more effectively. Organs with large fenestration such as the liver show increased uptake of NPs.
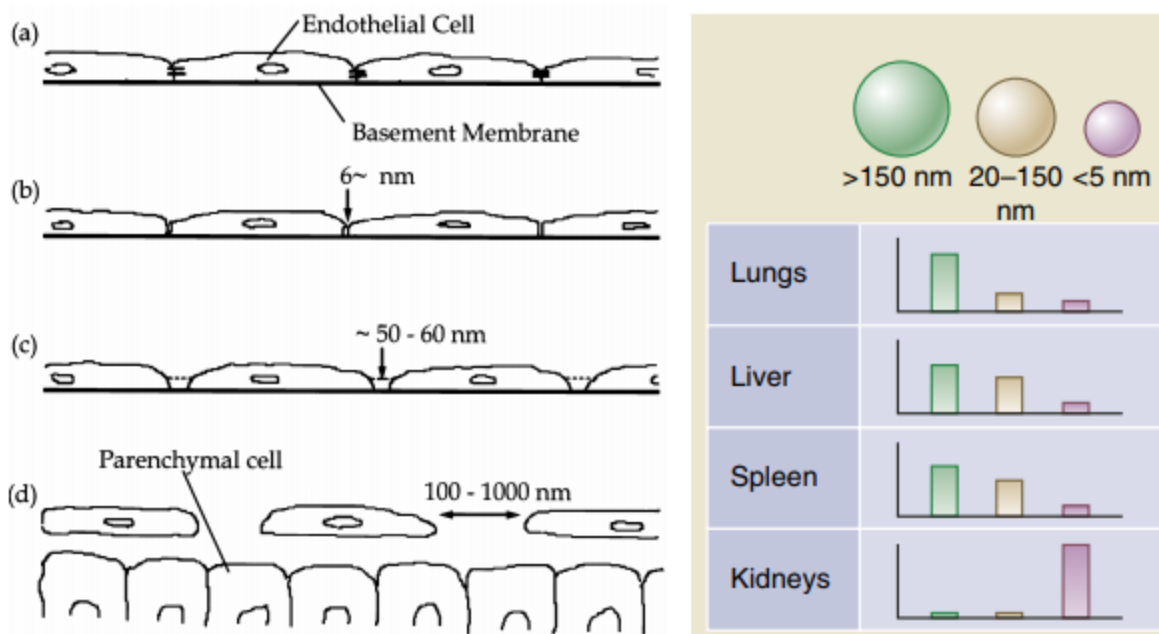
*Figure 7: NP's biodistribution depends on blood capillary's pore size. (**left** [74]) representative blood capillary walls of different tissues. Endothelial cells making the capillary wall can allow passage of particles between them. The gaps, called fenestrae or pores, are of different sizes in different tissues. (**a**) non-fenestrated capillary with tight junctions, characteristic of the brain and the retina. (**b**) non-fenestrated capillaries with loose junctions, characteristic of most tissues, such as skin, muscle and fat (pore size ~6 nm). (**c**) fenestrated capillaries, characteristic of the kidney (pore size upper limit ~15 nm [75]) and intestine among others. (**d**) sinusoid capillaries, characteristic of the liver and spleen, among others. (**right** [52]) as a consequence, NPs of different sizes would have different capacity to extravasate from the blood vessel to the tissue. The figure on the right shows NP's accumulation in different tissues as function of NP's size. This is also the result of other parameters (such as blood flow to the tissue and metabolism), as discussed in chapter 1.b.*

 Specifically important, is the finding that many pathologic tissues (i.e., inflammation and cancer) are characterized by increased permeability of blood vessels, leading to better NP extravasation into diseased sites[60,76]. This, together with poor lymphatic drainage is thought to be responsible for the Enhanced Permeability and Retention (EPR) effect. Post extravasation, the NP's size also influences their ability to diffuse through the extracellular matrix deep into the tissue[77,78]. This effect was demonstrated on 3D cell cultures with gold NPs of different sizes (Figure 8). Smaller NPs penetrated deeper and faster into the core of the in vitro simulated tissue.

Multicellular Spheroids
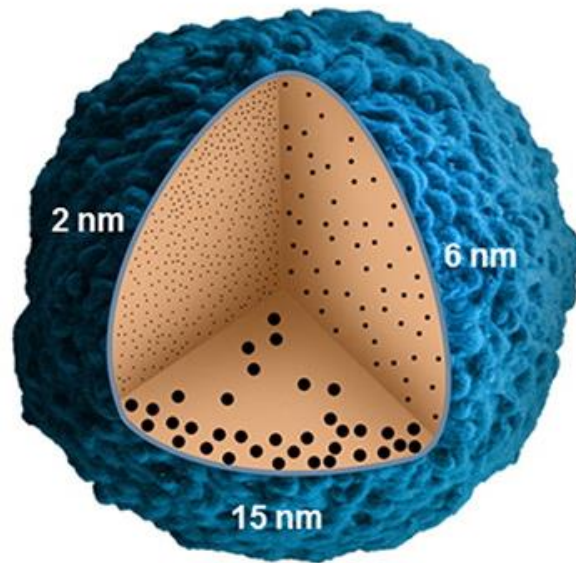
Figure 8: How tissue penetration depends on NP's size was demonstrated using in-vitro 3D cell culture. NPs of 2, 6, and 15 nm were administered and penetration quantified. Smaller NPs penetrated deeper and faster into the core of the sphere[78]*.*

A major cause of NPs clearance from plasma is uptake by the mononuclear phagocytic system, composed of monocytes, macrophages and dendritic cells, present in the blood stream and in some tissues (e.g., liver, spleen, lungs). Liver and spleen macrophages internalize through endocytosis NPs larger than 100 nm and thus remove them from circulation[73,79] (these NPs frequently end up endosomes, later discussed). Likewise, NPs with immunogenic surface of all sizes are rapidly internalized by these phagocytic cells. Figure 9 shows blood half-life times and organ-level biodistribution of gold-PEG NPs of different sizes and same zeta potential (slightly negative)[80]. All these NPs are too big for renal clearance, relatively unaffected by a protein corona (and thus not immunogenic) and show long circulation times. However, a monotonous increase in circulation time with reduced size is evident. The biodistribution shows removed NPs end up mostly in the liver and spleen.

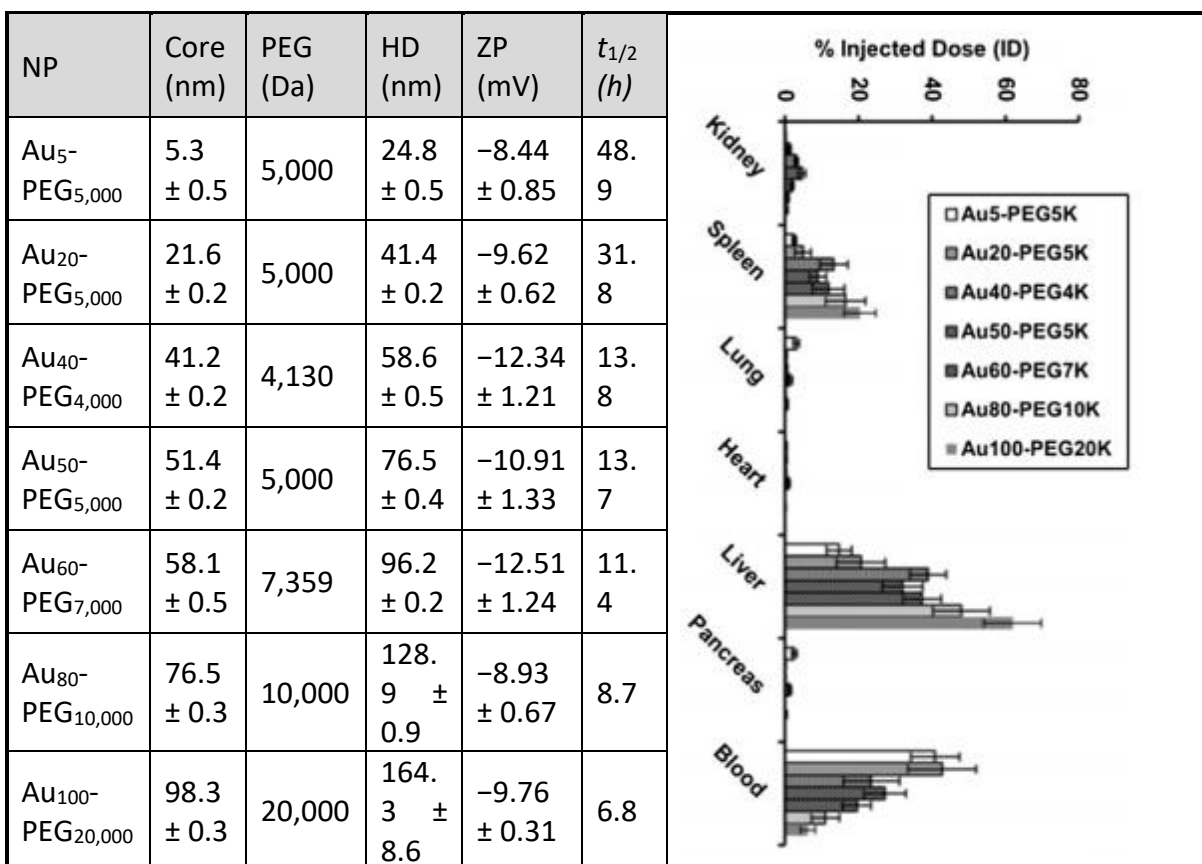| NP	Core (nm)	PEG (Da)	HD (nm)	ZP (mV)	$t_{1/2}$ (h)
Au5-PEG5,000	5.3 ± 0.5	5,000	24.8 ± 0.5	−8.44 ± 0.85	48.9
Au20-PEG5,000	21.6 ± 0.2	5,000	41.4 ± 0.2	−9.62 ± 0.62	31.8
Au40-PEG4,000	41.2 ± 0.2	4,130	58.6 ± 0.5	−12.34 ± 1.21	13.8
Au50-PEG5,000	51.4 ± 0.2	5,000	76.5 ± 0.4	−10.91 ± 1.33	13.7
Au60-PEG7,000	58.1 ± 0.5	7,359	96.2 ± 0.2	−12.51 ± 1.24	11.4
Au80-PEG10,000	76.5 ± 0.3	10,000	128.9 ± 0.9	−8.93 ± 0.67	8.7
Au100-PEG20,000	98.3 ± 0.3	20,000	164.3 ± 8.6	−9.76 ± 0.31	6.8

Figure 9: NP characterization and Mouse blood half-life (table), and biodistribution 24 hours post injection (graph) of gold-PEG NPs of different sizes. Bigger NPs are captured by phagocytic cells and end up mostly in the liver and spleen[80].

NP's geometry (e.g., spheres, rods, disks, figure 2) has an impact on their flow and extravasation from blood vessels [52,81]. Under laminar flow, spherical NPs tend to have ordered flow away from the blood vessel walls, decreasing chances of both extravasation and interaction with endothelial cells. Rod and disk-shaped NPs on the other hand, tumble and steer themselves (randomly) into the blood vessel walls more often. Once in contact with a cell (any cell), NP's geometry also affect chances of adherence and internalization[5]. That can be mediated by the degree of possible contact between the NP and the comparably flat cell surface.

Surface properties of NPs, such as charge and molecular recognition (i.e., ligand-receptor interaction) are an important factor. Positively charged NPs tend to be internalized quickly by macrophages and other cells (e.g., blood vessel endothelial cells) due to accumulation of a protein corona that triggers immune response, as well as direct interaction with cells plasma membrane[52,79,82]. This leads to quick elimination from circulation (Figure 10). Negative NPs have longer circulation time, and neutral to slightly negative NPs have the longest circulation time. This is due to low interaction with cells plasma membrane and low binding of plasma proteins (no protein corona), thus avoiding immune system cells and other specific interactions (explained later - molecular recognition).
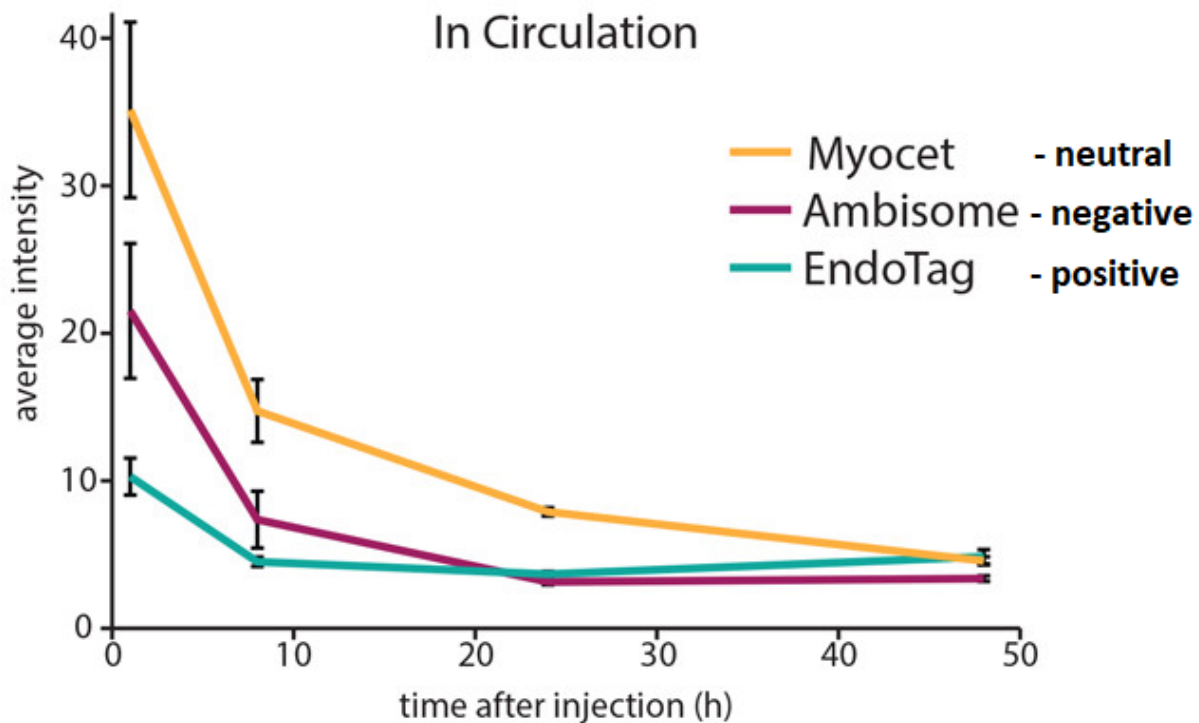
Figure 10: effect of surface charge on NP's circulation time[82]. ~110 nm liposomes of different surface charge were injected to zebra fish at equal dose, and their blood concentration was estimated by fluorescence emission. EndoTag, a mostly cationic liposome with zeta potential +46 mv were quickly eliminated from circulation. Ambisome, a mostly anionic liposome with zeta potential -34 mv had longer circulation time. Myocet, a zwitterionic liposome with zeta potential -16mv had the longest circulation time. This blood clearance is the result of cellular uptake, by macrophage and other cells.

Molecules on the surface of NPs (e.g., antibodies, peptides, sugars, Figure 2 bottom) can interact with specific biological mechanism, affecting the in-vivo behavior of NPs, like biodistribution, cellular uptake and metabolism. This is true both with deliberately attached molecules and with randomly adsorbed biomolecules of the protein corona[70,83]. Many NP designs take advantage of this to create "actively targeted" NP[84,85]. For example, surface grafted molecules can bind endothelial cells and initiate transcytosis, thus increasing NP's accumulation in specific tissues[86] (e.g., crossing the blood brain barrier); Antibodies are used to bind cancer cell specific epitopes and promote cellular uptake[15][87].

Studies indicate that NP's elasticity also has influence over NP's cellular uptake and bio-distribution[88,89]. Despite seemingly conflicting results, many results backed by computer simulations indicate that softer NPs are more difficult to internalize through endocytosis, as well as having different endocytic mechanisms for particles with different elasticity.

1.C.iii - Drug release: Ultimately a drug needs to be loaded onto the NPs and released in the body. This can be done in different ways depending on the NP. Some drugs are covalently conjugated to the NP[90,91]. In other cases, the drug is physically adsorbed or confined by the NP[92,93].

Each method dictates a drug loading capacity and release kinetics. Some NPs use an external trigger to quickly release the drug near its target, compared to off target sites. Such trigger can be local pH, temperature, or hydrolytic enzymes[94–96].

Research showed NPs can be excreted with the urine or feces[97,98], or metabolize/degrade within the body[99–101]. Some of these NPs can be biocompatible[102,103]. Other NPs are known to be toxic in vitro or in vivo[104,105].

1.C.iv - Molecular recognition and ligand density: one way to improve NP's biodistribution is through specific ligand-receptor interactions. Small molecules with specific and high affinity (e.g., peptides, antibodies) can be conjugated to the NP's surface to initiate specific interactions with target cells or tissue[106–108]. This interaction can often lead to cell internalization or transcytosis[87,109]. Because a single modification of a NP can impact its bio-fate through different mechanisms (as previously discussed, e.g., size, immune system interactions), more is not always better regarding targeting ligands and target affinity[15,110,111]. The implementation of this observation is often limited by the ability to synthetically control the number of ligands conjugated per NP. A part of this work was dedicated to the synthesis of NPs with a controlled number of targeting ligands and the evaluation of their performance in vivo.

1.C.v - Cellular uptake: This image painted by research works in recent decades is a good base for the implementation of NPs for drug delivery (evident by the approval of different drug-loaded nanoparticles for clinical use[112,113]), as well as the ongoing research in effort to reach new therapeutic targets. Many new therapeutic targets are localized inside cells, within the cytoplasm or inside intracellular organelles (e.g., cytosolic enzymes, transcription factors in the nucleus). For NPs to reach these targets they must first enter the cell, i.e. cross the plasma membrane. The major route of entry to the cell is through endocytosis, for macromolecules in general, as well as for NPs[114–119]. Endocytosis (Figure 11) starts by deformation of the plasma membrane to surround and engulf material present outside the cell, followed by fission to obtain internalized material surrounded by a membrane called vesicle or endosome. These endosomes (and the NPs trapped inside them) go through "endosomal maturation", a process that expose internalized material to lower pH and hydrolytic enzymes and ultimately degrade the material. Intermediate steps in this process include early endosomes, multivesicular bodies, late endosomes and finally the lysosome.
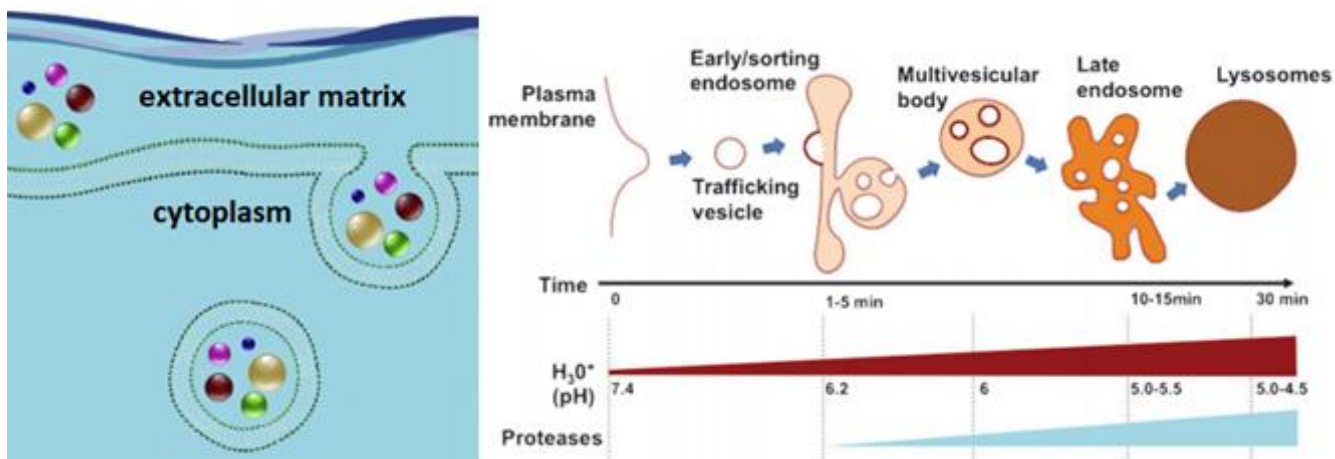
Figure 11: Endocytosis. (left) molecules outside the cell are surrounded by the plasma membrane by deforming the membrane, followed by fission (pinching off) to form an internalized vesicle[116]. (right) these vesicles are mobilized and go through a series of fusion and fission reaction with other compartments of the endosomal/lysosomal pathway inside the cell[118]. Throughout this process internalized material is acidified and exposed to hydrolytic enzymes.

1.C.vi - Mechanisms of endosomal escape: to come in contact with factors located inside the cellular cytoplasm and organelles and to avoid degradation in lysosomes, the NPs or the therapeutic agents must escape the endosomal membrane at earlier stages of evolution. Different mechanisms to achieve this goal have been described in the literature for different proteins and NPs. The proton sponge mechanism (Figure 12, a) debatably explains the ability of poly-cationic materials with pH buffering capacity within the range of endosomal pH to escape the endosome[120–123]. As the pH drops inside the endosome, a basic poly-cationic material would become increasingly charged; this would demand the influx of counter ions such as chloride ions to maintain charge neutrality, increasing osmotic pressure. If the endosome is small enough this might lead to endosomal rupture. Membrane fusion (Figure 12, b) between viral envelopes and endosomes can be triggered by specialized viral proteins[124] (e.g., hemagglutinin protein of the influenza virus). Similarly, such fusion can occur between endosomes and liposomes made of cationic lipids. Pore formation (Figure 12, c) by peptides, able to self-assemble into organized structures across the membrane, enabling the endosomal escape of small cargo molecule (up to 5000 Dalton). Polymer induced membrane disruption (Figure 12, d) by different polymers (e.g., PEI, dendrimers, poly-anionic) is thought to proceed in different mechanisms depending on the specific polymer.
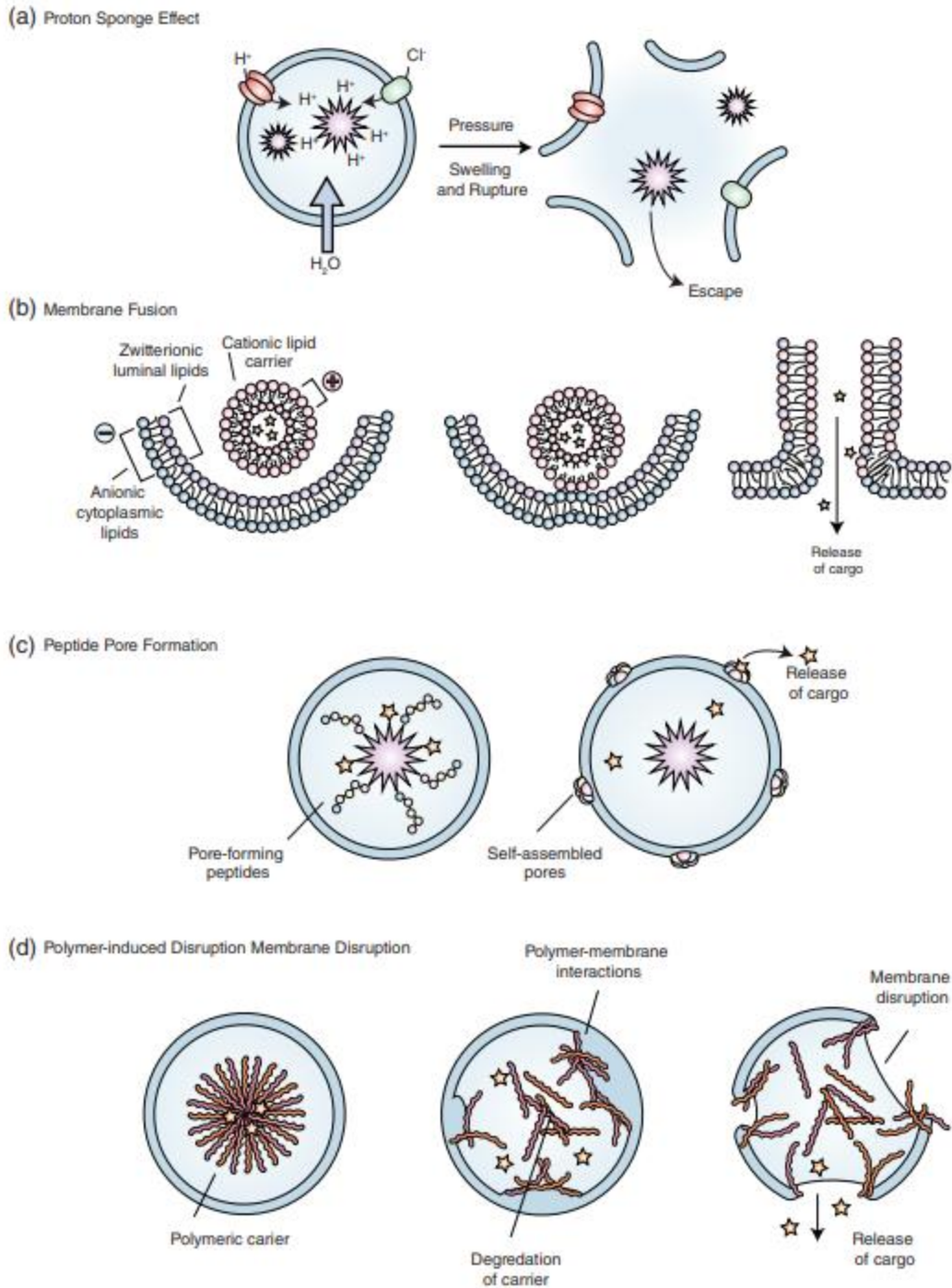
Figure 12: mechanisms of endosomal escape[117]. *(a) the proton sponge effect results in endosomal rupture by increasing osmotic pressure. (b) membrane fusion of viral envelope or cationic liposomes. (c) self-assembly of protein creating a pore in the membrane. (d) different polymers can disrupt the membrane by different mechanisms.*

1.C.vii - Evidence of cytoplasmic localization: with few exceptions, evidence of endosomal escape or cytosolic localization of different materials are given through qualitative biological (e.g., expression of foreign DNA or degree of protein synthesis) or fluorescent signals (e.g., colocalization with endosomal labels or subcellular distribution, Figure 13)[116,117,125]. These

methods suffer from low accuracy and prevents reliable comparison between different drug delivery systems. Recent attempts to develop a method to quantify endosomal escape used interaction with cytosolic factors to generate a signal, most often from a pro-fluorophore[126–128]. Other recent development offer semi-quantitative results based on western blot of biotinylated peptides[129]. However, no method has yet to become accepted as a standard, and the need for an accurate and sensitive method still exists.

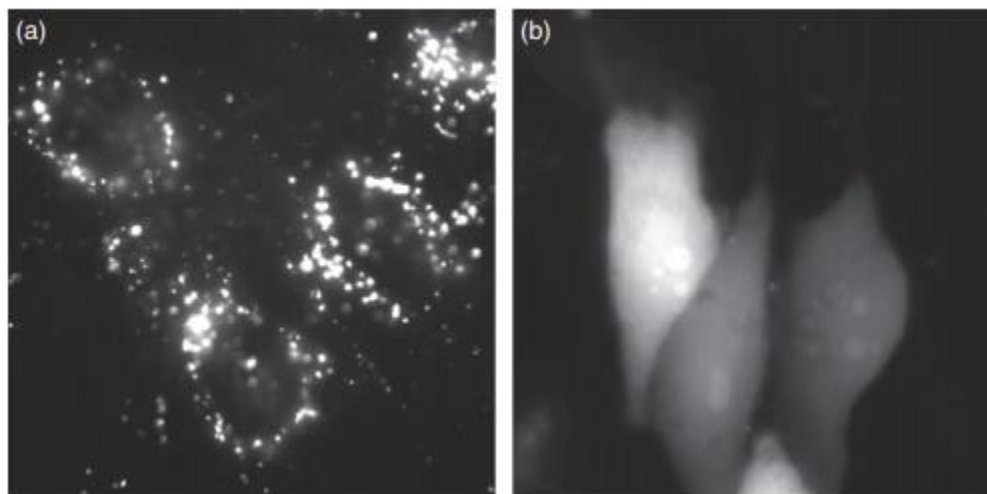Figure 13: (a) punctate distribution used as indication of low endosomal escape of fluorescent NPs, compared with (b) diffuse distribution indicating high endosomal escape[117].

1.C.viii - Qualitative in vitro models of endosomal escape: the cytoplasmic membrane of red blood cells can be used as a model of the endosomal membrane[130–132]. This is especially useful as permeabilization of these cells can lead to leaking of hemoglobin to the external solution, which is quantifiable by optical absorption. Following an incubation period of a membrane permeabilizing agent with the cells, the solution is centrifuged to sediment the cells while maintaining free hemoglobin in solution and measuring absorption. This model system can qualitatively indicate membrane permeabilization through "polymer induced membrane destabilization" or "pore formation".

A second in vitro model, usually used for small molecules, is the water/oil distribution coefficient. A vial is loaded with two immiscible solvents (e.g., water and octanol), and a solute is allowed to distribute between them (equation 1). The partition coefficient is defined as the equilibrium constant of this reaction (equation 2). This model test molecules ability to directly diffuse through the membrane. Octanol was found to be a good solvent to model solubility in biological membranes[133–135].

$$Eq.\,1: \quad solute^{water} \rightleftarrows solute^{oil}$$
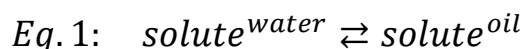
$$Eq.\,2: \quad K_{eq} = \frac{[solute]^{oil}}{[solute]^{water}}$$

1.C.ix - Quantification of endosomal escape: To quantify the degree of successful cytosolic delivery, we evaluated two methods, both based on a signal generated by exogenous NP's interaction with a cytosolic factor.

Fluorescence resonance energy transfer (FRET) is the exchange of energy between two fluorophores[136–139]: when one molecule (the donor) has a fluorescent emission that energetically overlaps the absorption of a second molecule (the acceptor), they can interact electrostatically (i.e. non-radiatively) to exchange the excitation energy. Because the acceptor's absorbing state decay faster than the donor's emitting state, this results in unidirectional energy transfer and a measurable change in fluorescent emission wavelength (Figure 14).
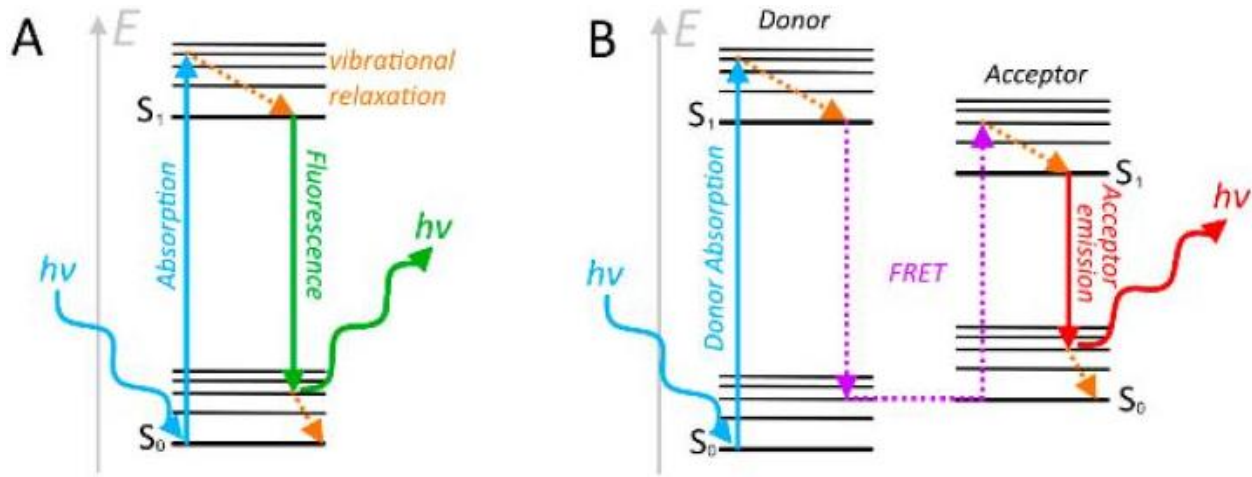

Figure 14: Jablonski diagrams describing fluorescence and FRET[139]. Horizontal black lines represent different electronic (S_0, S_1) and vibrational states of different energy. (A) a single fluorophore absorbs a photon and move to a higher energy state (blue arrow), followed by fast relaxation of vibrational energy (orange dashed arrow). Lastly the energy decay radiatively and fluorescence is emitted. (B) in the case of a donor-acceptor pair a different relaxation route becomes available through dipole-dipole interaction; the excitation energy is transferred to the acceptor molecule (purple arrows), followed by vibrational relaxation and radiative decay (red arrow) by the acceptor.

This interaction is highly sensitive to distances in the order of 1-10 nm, as illustrated by Eq. 3. E is the FRET quantum yield, r is the distance between fluorophores and R_0 is a constant characterizing the orientation and spectroscopic properties of the donor-acceptor pair.

$$Eq.\,3: \quad E = \frac{transferred\ energy\ quanta}{absorbed\ energy\ quanta} = \frac{1}{1 + (\frac{r}{R_0})^6}$$

The constant R_0 can be calculated using equation 4, where k is the orientational factor, equal to 2/3 for randomly rotating donor and acceptor. $\emptyset_D$ is the donor fluorescence quantum yield. n is the solution refractive index. And J is the spectral overlap integral between the donor and acceptor, given in equation 5, where $F_D(\lambda)$ is the peak normalized emission of the donor at wavelength λ, and $\varepsilon_A(\lambda)$ is the acceptor extinction coefficient at the same wavelength.

$$Eq.\,4: \quad R_0 = 8.785 * 10^{-5}\frac{k^2 * \emptyset_D * J}{n^4}$$

$$Eq.\,5: \quad J = \int F_D(\lambda) * \varepsilon_A(\lambda) * \lambda^4 * d\lambda$$

Given the absorption and emission spectra of any donor-acceptor pair, these equations can be applied to estimate the signal that would be generated by a specific fraction of NPs escaping the endosome.

As a second method, we tested the use of a profluorophore – FlAsH-EDT2 (Figure 15, 4,5-Bis(1,3,2-dithiarsolan-2-yl)-3,6-dihydroxyspiro[isobenzofuran-1(3H),9-[9H]xanthen]-3-one). This derivative of fluorescein (FlAsH) or carboxy-fluorescein (CrAsH) is non-fluorescent, and becomes fluorescent after binding with high affinity to a peptide sequence named Cys4 (with nanomolar dissociation constant)[140–143].
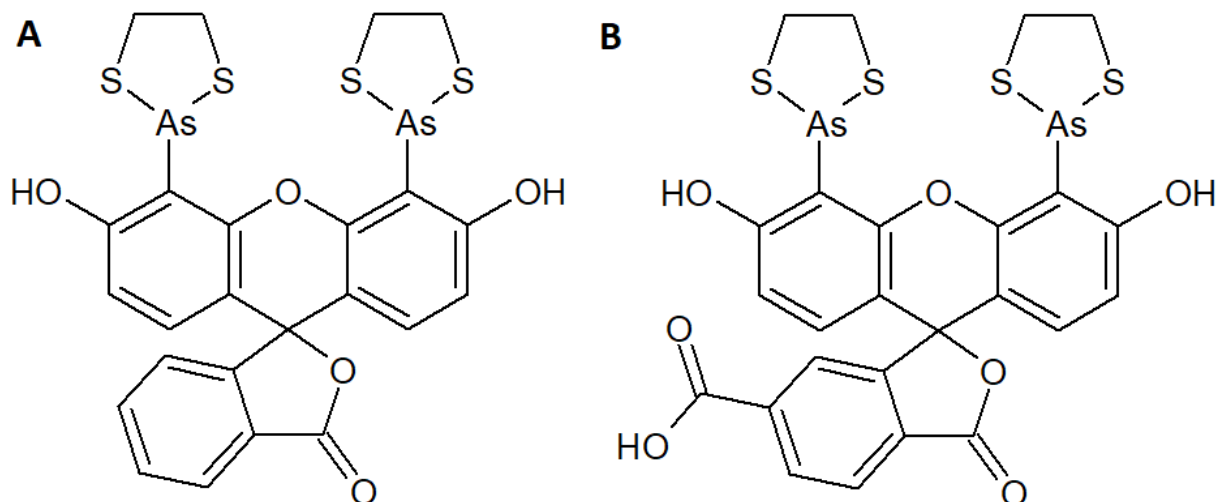
Figure 15: Chemical structure of FlAsH-EDT$_2$ and CrAsH-EDT$_2$ (differing by one carboxylic group). These pro-fluorophores can generate a signal when in contact with a peptide sequence, Cys4. This sequence can be expressed in cell's cytoplasm[140].

This pro-fluorophore (CrAsH) could be conjugated to a NP, and the Cys4 tag could be genetically fused and expressed on a cytoplasmic protein. The interaction between them would imply cytosolic localization of the NP and result in a measurable signal.

1.D - Summary and research aim

Following the progress in understanding of the rules that govern NP's behavior in vivo comes increasing motivation to implement them in clinical applications. Furthermore, current bottlenecks in drug development suggest that implementation of NPs for drug delivery is the way to go.

In the development of nanotechnology as in the development of macroscopic mechanical machines, simple functions are identified and perfected separately and later put together to perform a larger task. In this work we focus on three different functions or integration of functions for the realization of efficient drug delivery systems:

1. **The incorporation of "molecular recognition" moieties within nanodrug carriers:** in this part we aimed to test the effect of degree of NP's functionalization (with a molecular recognition function) on the NP's behavior in vivo. This was done using a method to produce NPs with a discrete number of chemical functional groups, to which the molecular recognition function is later conjugated. PMA capped gold NPs conjugated to the antibody Trastuzumab were used as a model.

2. **The incorporation of hydrophobic inorganic core within a NP through polymer capping:** here we aimed to describe the purity of NP samples prepared this way, methods to improve the purity, and the stability of the products. We achieve this by selectively removing excess polymer from a polymer capped-NP suspension and determining and colloidal stability by UV absorption and DLS.

3. **The development of functions for endosomal escape and cytoplasmic delivery:** starting from a point of having a delivery agent with non-reproducible positive results (PMA capped iron oxide NPs), we aimed to develop assays for mechanistic and quantitative studies, allowing the improvement of the delivery agent. Two mechanistic models – distribution coefficient and hemolysis were implemented. One method for quantification, FRET, was theoretically evaluated; and another method based on a pro-fluorophore was eventually implemented.

Chapter 2: Materials and Methods

Reagents: MOPS, Toluene, Methanol, Chloroform, Dodecylamine (DDA), Dodecanethiol, Poly(isobutylene-alt-maleic anhydride) average Mw ~6,000, THF, tetraoctylammonium bromide, tetrachloroauric acid, EDC, TBE buffer, NaOH, NaCl, NHS-fluorescein, carboxy-fluorescein, sodium periodate, sodium cyanoborohydride, Sodium borohydride, 14kD cellulose dialysis bags were all bought from sigma-aldrich. HCl was purchased from PanReac AppliChem. PEG-$(NH_2)_2$ was purchased from RAPP Polymere. Centrifugal filter systems (Amicon tubes, 100/50 kDa filter cut off), 0.22 μm filters were purchased from Millipore Corporation (Italy). Zeba size exclusion column, Alexa fluor 647 NHS, Alexa fluor 488, Lipofectamine 3000 were all purchased from Thermofisher. 300kDa float-a-lyzer dialysis bags were purchased from Spectrum. Ficoll PM70 was purchased from GE healthcare. Human blood mixed from different donors was donated by Niguarda hospital in Milan, Italy. Cetuximab (Erbitux) was purchased from Merck (Darmstadt, Germania)., Trastuzumab was acquired from Roche. Distilled water was obtained using a milli-q academic A10 system by Millipore. TEM imaging was done using Zeiss EM109, DLS measurements were done using a Malvern Zetasizer, ATR FT/IR-4100 was bought from Jasco

Synthesis of PMA with 75% DDA: to a round flask added 0.597 g dodecylamine and 0.665 g Poly(isobutylene-alt-maleic anhydride). Seal with cap and replace air with nitrogen using three vacuum→N_2 cycles. Using syringe add 20 ml THF and sonicate until all solids are dispersed. Maintain at 60 °C for 3 h, then reduce volume by vacuum to ~6 ml (solution becomes thick). Leave overnight at 60 °C, evaporate all solvent and re-dissolve in chloroform for 0.5 M monomer.

Preparation of PMA coated NPs with a discrete number of targeting ligands

Synthesis of hydrophobic gold NPs: 2.17 g tetraoctylammonium bromide was dissolved in 80 ml toluene. 300 mg tetrachloroauric acid was dissolved in 25 ml milli-Q water. Solutions were mixed in a separation funnel for 5 min and aqueous solution was discarded. Toluene was moved to a new flask and a fresh solution of sodium borohydride (334 mg in 25 ml milli-Q water) was added dropwise in 1 min. Solution was left with stirring for 1 h, and then moved to a separation funnel and washed with 25 ml of: 10 mM HCl, 10 mM NaOH, 4×25 ml milli-Q water. In each wash the aqueous solution was added and mixed for 1 minute, allowed to separate from the toluene and discarded. sometimes solid NaCl was added to assist phase separation. Toluene suspension was moved to a new flask and left with stirring overnight. Added 10 ml dodecanethiol and heat suspension to 65 °C for 2-3 h. The suspension was centrifuged at 1000 rcf for 5 min and sediments were discarded. 80 ml of methanol were added and the suspension was centrifuged again to precipitate the NPs. Supernatant was discarded, and NPs were resuspended in chloroform.

Phase transfer of 5 nm gold NPs: to 1 nmol of NPs in chloroform add 73 μl PMA in chloroform 0.5 M monomer. Sonicate for 1 min at room temperature. Evaporate solvent at 50 °C under vacuum and add 4 ml 50 mM NaOH solution. Sonicate until clear (~5 min). Filter using 30 kDa cutoff centrifuge filter to remove excess salts and introduce buffers as necessary.

Functionalization with PEG and separation using gel electrophoresis: using 100 µl PMA coated NPs in water at ~3 mg/ml, add 10 µl PEG diamine 10 kDa 10 mM, and 10 µl EDC in water around 25 mM (EDC concentration had to be calibrated for each preparation and tested in the gel for optimal mix containing both mono- and bi-functionalized NPs). After calibration the reaction could be scaled up as needed.

Agarose gel was prepared by boiling 5 g agarose in 250 ml TBE buffer with stirring. Let solution cool to 55 °C with stirring and cast. When solid mix samples with 10% glycerol and load to lane. Run for 65-70 min at 110 V (with TBE buffer as electrolyte solution).

To recover NPs from gel, cut out the band and place in 14 kDa dialysis bag together with few milliliters of buffer , seal and reapply voltage. Recovered NPs were re-concentrated using a centrifuge filter, centrifugated to sediment gel particles at 3000 RCF for 1 h and filtered using 0.22 µm syringe filter.

Antibody labeling and conjugation: antibody was dialyzed against PBS and concentration was determined by UV absorption. NHS-fluorecein or Alexa fluor 647 NHS were added in a 30 times mole excess and incubated overnight, then washed using 50 kDa centrifuge filter and then 7 kDa size exclusion column.

To 166 µl of labeled antibody 1 mg/ml in PBS, added 110 µl sodium periodate and incubate at 4 °C for 30 min. Use size exclusion column to remove salts and add sodium borate buffer pH 8.5 100 mM. add 94 µg of mono-functionalized NPs or 47 µg bi-functionalized NPs. Incubate for 2 hours and add sodium cyanoborohydride in sodium borate buffer pH8.5 to final concentration of 3.14mg/ml (toxic, work in fume hood). Incubate for 2 hours in room temperature and dialyze using a 300 kDa dialysis bag against PBS.

Testing the colloid stability and purity of polymer coated nanoparticles:

Labeling PMA with Alexa Fluor 488 cadaverine: 60 mg PMA in chloroform solution was evaporated and re-dissolved in THF. Added 179 µl Alexa Fluor 488 cadaverine in DMSO (0.5 mg/ml) and incubated for 48 hours at room temperature in the dark. Solvent was then evaporated and labeled PMA was re-dissolved in chloroform, later to be used for phase transfer of NPs.

Phase transfer of 18 nm gold NP suspended in chloroform: to 2 mg gold NPs in chloroform added 60 mg fluorescently labeled PMA. Suspension was sonicated for one minute and the solvent was evaporated at 50 degrees under vacuum. 50 mM NaOH solution was then added to resuspend the NPs. Suspension was then filtered by 50 kDa centrifuge filter to remove base and add sodium borate buffer.

Polymer removal by NP precipitation: to six, 15 ml polypropylene centrifuge tubes added 15 ml NP suspension in sodium borate buffer, pH 8.3 30 mM. All tubes were centrifugated at 10k RCF for 70 min. 14.5 ml of the supernatant ware recovered and replaced by the same buffer (or not,

in according to the final dilution factor). The samples were then sonicated for 2 min and centrifugated again (total of 5 centrifugations).

After last centrifugation, the NP suspension was filtered twice in deionized water to remove the buffer (using 50 kDa centrifuge filters) and diluted using different buffers (sodium borate pH 8.3 30 mM, phosphate buffered saline pH 7.4 20 mM, phosphate buffer pH 7 20 mM). Stability was assessed after three days using UV-VIS absorption.

Polymer was quantified in the NP suspension and in the supernatant using fluorescence (ex: 471 nm, em: 516 nm) and NPs were quantified using UV-VIS absorption at 520 nm.

Hemolysis assay as model of endosomal escape through membrane destabilization:

Isolation of RBCs and plasma from blood: Human blood was diluted ½ in PBS. To a centrifuge tube, added 15 ml Ficoll, and 20 ml diluted blood was added on top drop wise. Sample was centrifuged for 30 min at 408 RCF without break for deceleration. Human plasma was recovered from the top and RBCs were recovered from the precipitate. RBCs were then resuspended in 154 mM NaCl solution and resedimented three times. The concentration of RBCs in the final suspension was quantified by counting cells in a burker chamber under a microscope.

Hemolysis assay: to a series of microcentrifuge tubes added by this order: 100K RBCs, a PMA sample, and a specific buffer. In some experiments, PMA was preincubated in human plasma of specific concentration for 10 minutes prior to dilution of the PMA into the RBCs. After set incubation period with RBCs (30-120 min, 37 °C, shaking) tube were centrifuged at 1500 RCF and soup optical density was quantified at 541 nm.

Octanol/water distribution coefficient as model of endosomal escape through direct diffusion: to 3 mg, 3 mg/ml PMA in sodium borate buffer pH 9 30 mM (see hemolysis for phase transfer), added Alexa Fluor 488 cadaverine to 0.1 mM final concentration. added 4 µl EDC 0.1 M, four times, every 10 min. Filtered sample using 50 kDa centrifuge filter.

Citrate buffer (pH 4.5, 5, 5.5, 6.5) and phosphate buffer (pH 7.4) were prepared at 20 mM and NaCl was added to set the ionic strength to 154 mM.

To a glass vial added 1.5 ml buffer at desired pH and added Alexa Fluor 488 labeled PMA to final concentration of 75 µg/ml. On top, added 1.5 ml of octanol. Incubated for 4 days while tilted rotating at ~45° and 40 RPM.

Octanol phase was collected in microcentrifuge tubes, centrifuged at 2000 RCF for 1 min to remove water leftovers and emission was quantified from the octanol phase.

Assessment of FRET as a tool to quantify cytosolic localization: the Matlab code used is added in appendix 1.

Absorption and emission spectra of different fluorophores were taken from either the manufacturer's website or one of these databases:

http://www.fluorophores.tugraz.at/

http://www.spectra.arizona.edu/

CrAsH-EDT$_2$ as a sensor to quantify cytosolic localization:

Conjugation of CrAsH or Carboxy-Fluorescein to PMA: PMA was transferred to water as previously described and diluted to 15 mg/ml in deionized water. Added EDBE to 250 μM (0.5% monomer mole) and EDC to 2 mM and incubated for 2 h. Sample was filtered using a 50 kDa centrifugal filters to remove excess reagents.

To 1 ml phosphate buffer pH 7, 5 mM added CrAsH-EDT$_2$ to reach OD$_{507nm}$ of 15.6. Add sulfo-NHS to 7.6 mM and EDC to 7.6mM. Incubated solution at room temperature for 30 min and add 3 mg PMA-EDBE and 200 μL sodium borate buffer pH 8.5 0.3 M. Incubate overnight in fridge and filter using 50 kDa centrifuge filter.

Conjugation of CrAsH or Carboxy-Fluorescein to PEI: to 10 μL PEI (10 mg/ml) in MOPS buffer (400 mM, pH 7) added 80 μL CrAsH or carboxy-fluorescein in DMSO (1.35 mM), 200 μL EDC (0.2 M) in PBSx5 (pH 7.4) and left in fridge overnight. solution was then filtered using a 10 kDa centrifuge filter, three times using an 80 mM ethylamine solution and another three times using PBS (~1/10 dilution each wash).

Uptake assay using NP-fluorescein: using either HeLa cells (to test PEI) or T98G cells (to test PMA), 300k cells were seeded in a 12 multi well plate. 24 h later, cells were treated with either PEI-Fluorescein or PMA-Fluorescein and incubated at 37 °C. After the incubation period cells were washed with PBS and detached with trypsin and EDTA. Cells were collected in FACS tubes, centrifugated and resuspended in once in PBS and a second time in PBS+EDTA (2 mM) before FACS analysis.

Expression plasmid: using pcDNA3 as backbone in which we clone the coding sequence of EBFP2 (enhanced blue fluorescent protein-2) associated (or not) to the Cys4 sequence (amino acid sequence: FLNCCPGCCMEP).

Transfection of cells with expression plasmids: using either HeLa cells (to test PEI) or T98G cells (to test PMA), 180k cells (HeLa) or 250k cells (T98G) were seeded in a 12 multi well plate. 24 h later cells were transfected using Lipofectamine 3000 (Thermofisher) in accordance with the product protocol and another 24 h later, cells were used to assay for endosomal escape.

CrAsH endosomal escape assay: this was a modified version of a published protocol by Hoffmann et.al. Nature Protocols, 2010. NP-CrAsH conjugates were mixed with 50 mM Bal in DMSO for a 1:3 CrAsH:Bal mol ratio, incubated at room temperature for 5 min and diluted to desired PEI concentration. Cells were washed twice with PBS with Calcium and Magnesium and incubated at 37 °C with NP-CrAsH in 500 μl of medium without FBS. After the incubation period, NPs and medium were removed and replaced with 200 μM BAL (2,3-Dimercaptopropanol) in PBS for 10 min at 37 °C. Cells were washed twice with PBS with calcium and magnesium and incubated for

another 1 h at 37 °C in medium without FBS before harvesting the cells. After the incubation period cells were washed with PBS and detached with trypsin and EDTA. Cells were collected in FACS tubes, centrifugated and resuspended in once in PBS and a second time in PBS+EDTA (2 mM) before FACS analysis.

Chapter 3: Results and Discussion

4.A - Synthesis of PMA for use as polymeric micelles and polymer coating for hydrophobic NPs

commercial poly[isobutene alt-maleic anhydride] was reacted in organic solvent with dodecyl amine overnight unless otherwise stated, in 4:3 PMA monomer to dodecylamine (DDA) mole ratio (Figure 16).
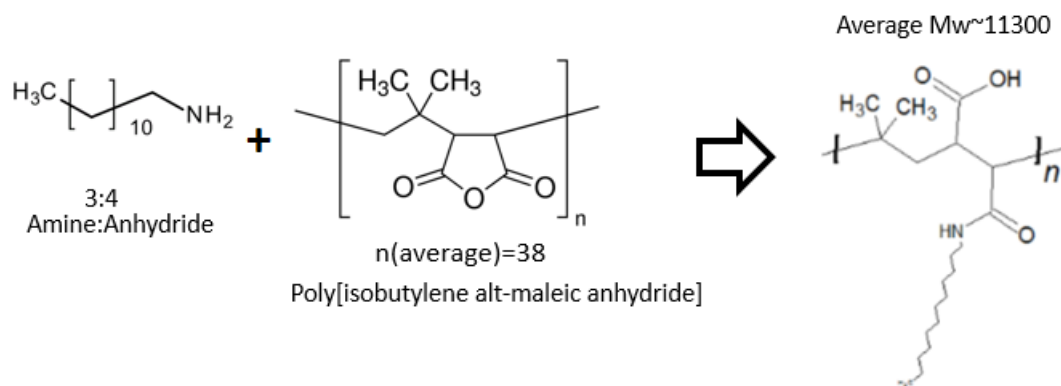

Figure 16: Preparation of amphiphilic polymer for drug delivery as micelles or surface coating of other hydrophobic NPs. Reaction of dodecylamine with PMA.

The product IR spectra (Figure 17) showed lower absorption typical of the anhydride (black dot), and appearance of peaks typical of carboxylic acid and substituted amide (red dots), confirming the success of the reaction[144,145].
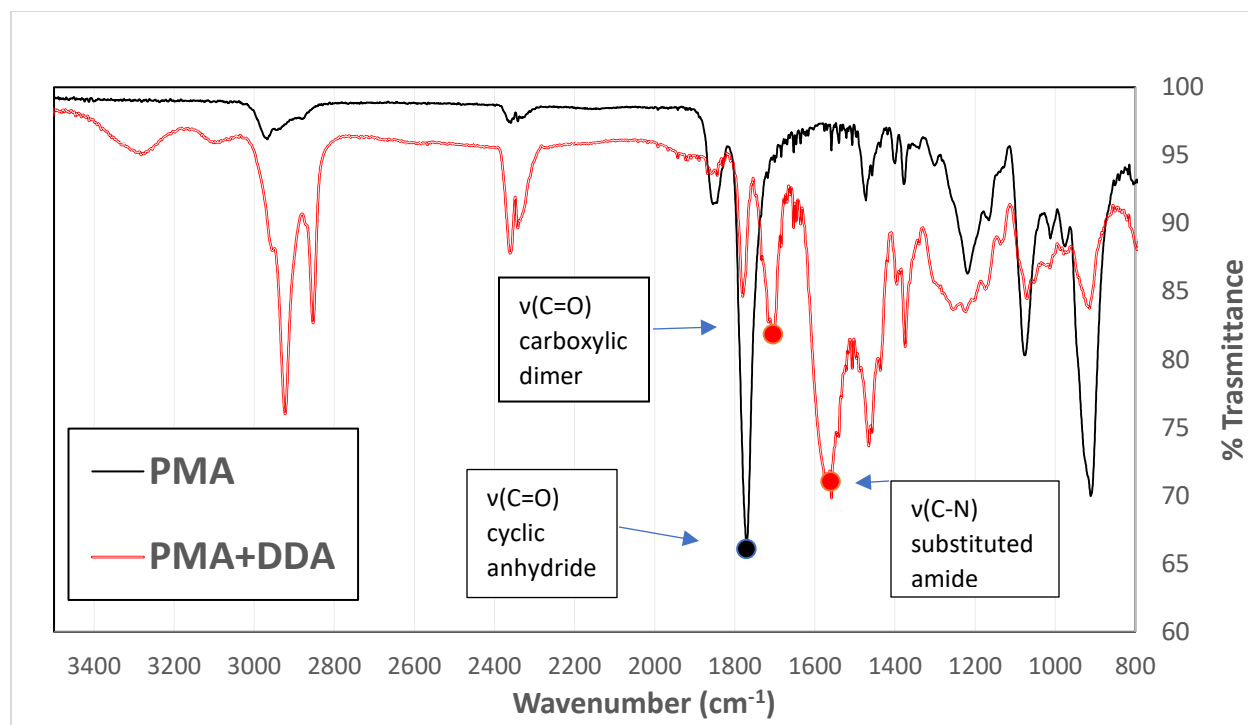
Figure 17: IR spectra of PMA before and after reaction with 0.75 mole ratio of dodecylamine. Marked by a black dot is the absorption peak characteristic of an anhydride ring, with lower intensity after the reaction. Two red dots mark peaks appearing after the reaction, typical of carboxylic acids and monosubstituted amides[144,145].

After solubilization in water PMA was found to form ~10 nm aggregates with pH and ionic strength dependence. Figure 18 shows that at pH 9 with 40 mM ionic strength the DLS size of PMA was 7.4 nm (number distribution) and zeta potential -79 mV. A pH titration revealed a buffering range between pH 5-10 (Figure 19). A calibration curve found optical absorption at 250 nm to be suitable to estimate the polymer concentration in pH 7 phosphate buffer between 3-0.03 mg/ml.
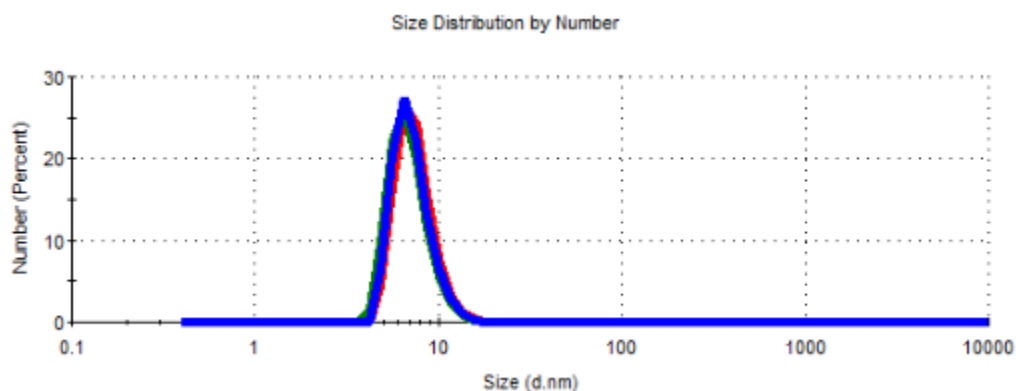
Figure 18: DLS spectra of PMA at pH 9 and 40 mM ionic strength. Aggregate size was found to increase with ionic strength and decrease with pH.

30
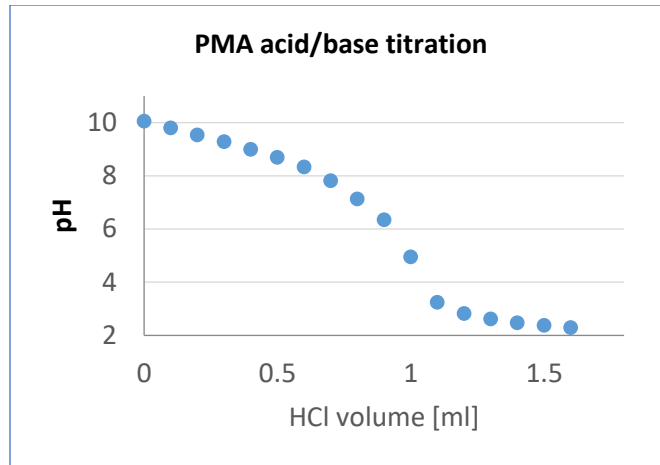
Figure 19: pH titration of PMA showing PMA's buffering range between pH 5-10.

4.B - Preparation of PMA coated NPs with a discrete number of targeting ligands

gold NPs were synthesized by reduction of chloroauric acid in organic phase, stabilized with hydrophobic ligands and stored in chloroform. TEM image showed a 5 nm gold core, and DLS showed a hydrodynamic diameter of 8.5 nm (Figure 20).
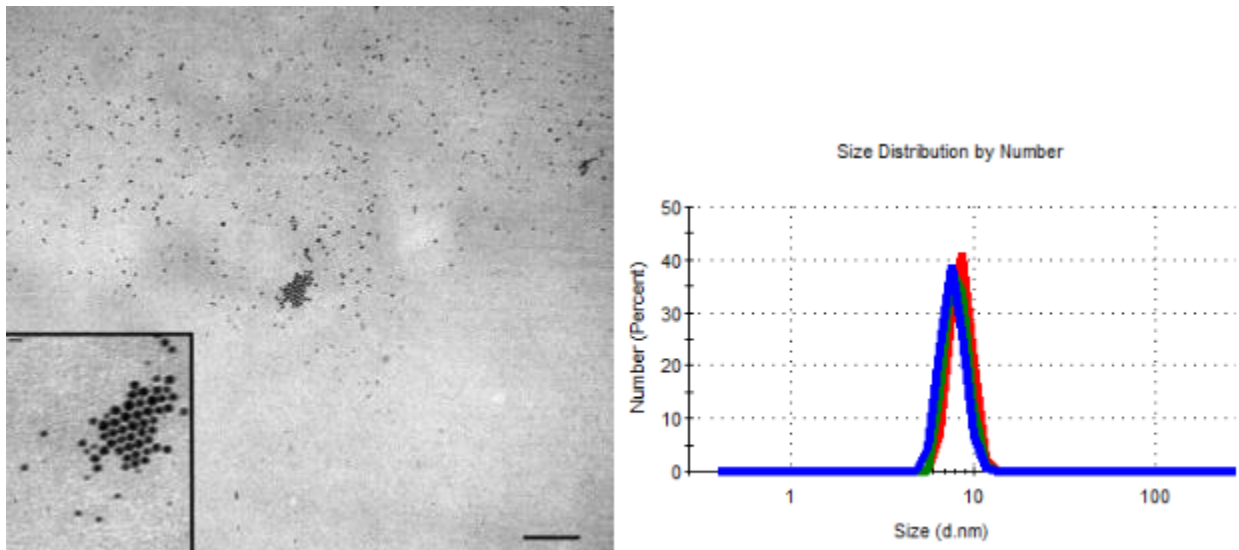
Figure 20: TEM and DLS size of unmodified gold NPs shows uniform size and no aggregation. Scale bar represents 50 nm and 5 nm in magnification.

NPs were phase transferred using PMA as surface coating to allow water dispersibility. DLS in water showed a single peak at 12 nm (Figure 21). these NPs showed no sign of aggregation for more than a year.
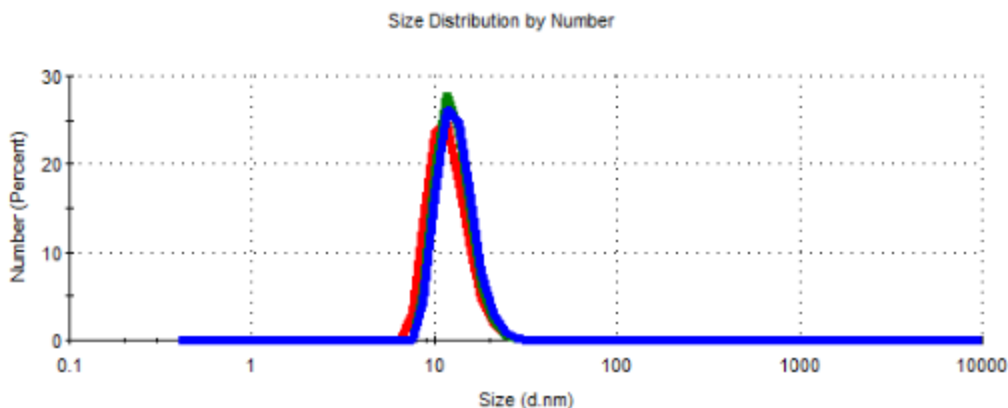
Figure 21: hydrodynamic size of PMA coated gold NPs in water.

To obtain NPs with exactly one, or exactly two functional groups for targeting agent conjugation, NPs were initially conjugated to 10 kDa PEG diamine, to yield a mixture of NPs non-, mono-, and bi-conjugated PEG, as well as aggregates. This mixture was than separated using gel electrophoresis (Figure 22), and NPs with exactly one or exactly two conjugated PEG-amine chains were recovered from different bands.
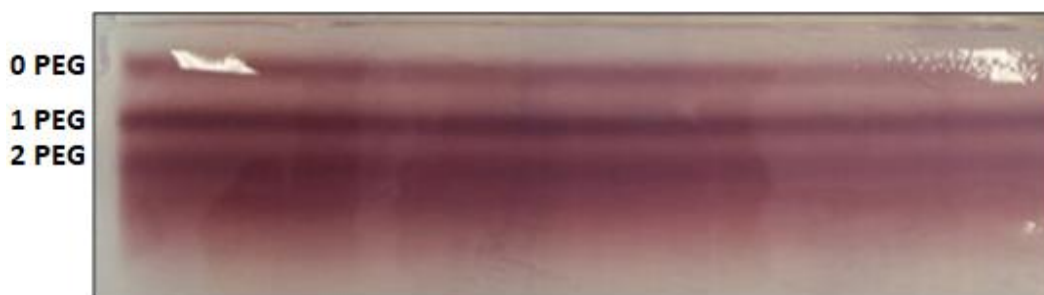
Figure 22: Separation of gold NPs with discrete number of amine groups using gel electrophoresis.

These amino groups were conjugated to an antibody (Trastuzumab or Cetuximab) through reductive amination, using the (oxidized) sugar at the Fc region of the antibody. Antibodies used were first labeled with a fluorescent dye (fluorescein), used to assess efficiency of binding. Emission of resulting NPs showed higher emission from bi-functionalized NPs, and bigger hydrodynamic radius (by DLS) indicating that the higher amine content translated to a higher antibody content (Figure 23). The ratio of emission was lower than expected, probably due to differences in free PMA content (through which the conjugation is carried) or due to physical adsorption of antibody the surface of NP-1xPEG. This is partly addressed in the next section (Testing the colloid stability and exchange kinetics of polymer coated nanoparticles).

NP	DLS size [nm]
NP-1xPEG	9.6±0.4
NP-2xPEG	11.1±0.1
NP-1xAb	11.3±0.4
NP-2xAb	18.1±0.6
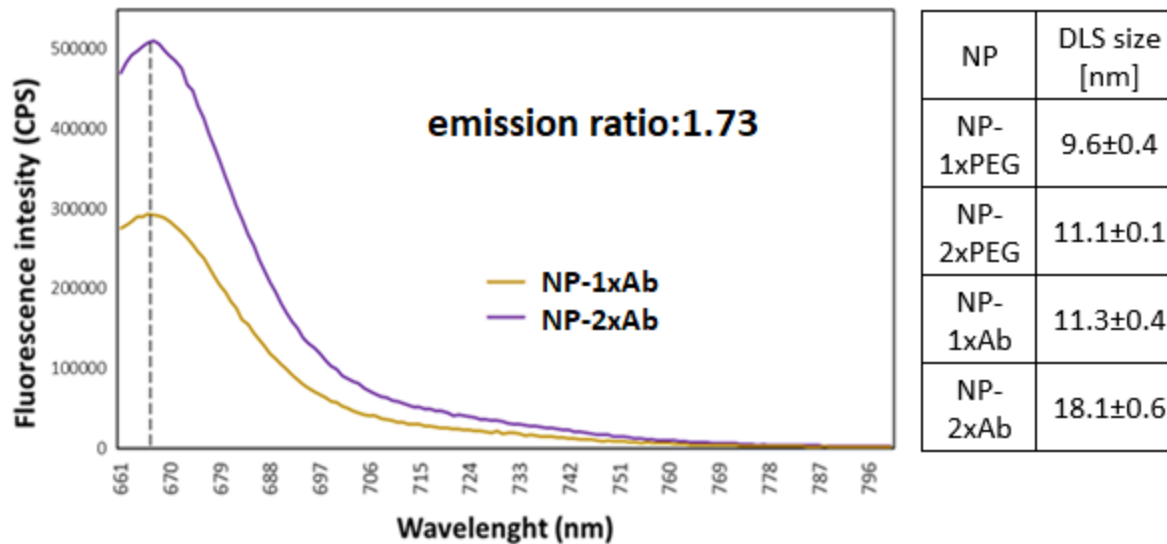
Figure 23: Characterization of gold NPs with discrete number of functional groups. (right) DLS size of different NPs, showing increasing size with increased functionalization. (left) NPs with two amine groups show higher emission, corresponding to higher Ab content. The ratio of 1.73 is lower than the expected value (2) can be a result of different PMA content between NP-1xPEG and NP-2xPEG, as well as from physical adsorption of antibody to the surface of NP-1xPEG.

These NPs were used as a model of molecular recognition in drug delivery, with cell culture as well as in a tumor bearing mouse model and showed improved activity in vivo of monofunctionalized NPs, as published in Nature Communications, 2016 (see publications).

4.C - Testing the colloid stability and purity of polymer coated nanoparticles

Different phase transfer techniques use specific ligands to grant NPs colloidal stability in water and allow further surface conjugation. However, if excess ligands are left in solution this might negatively affect successful surface conjugation to the NPs as well as result in adverse effects *in vivo*. To test the purity and stability on polymer coated NPs, we designed an experiment to sequentially remove excess polymer while measuring polymer content and the NP's stability. PMA was fluorescently labeled and used to phase transfer hydrophobic, 18 nm gold NPs synthesized by the citrate method and stabilized by dodecylamine (by other members of the group). This method yields NPs with highly monodisperse size, thus making any colloidal instability evident in methods such as DLS. Figure 24 and Figure 25 show the DLS size of the NP before and after the phase transfer by fluorescent PMA, showing similar size (~18 nm).
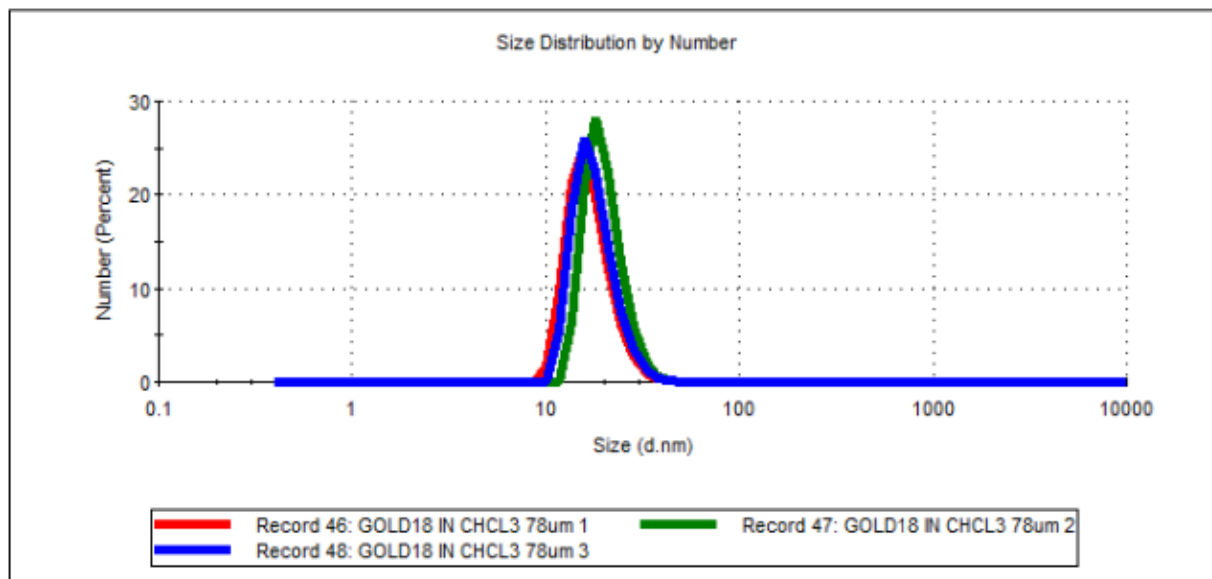
Figure 24: hydrophobic gold NPs in chloroform. Size distribution by number.
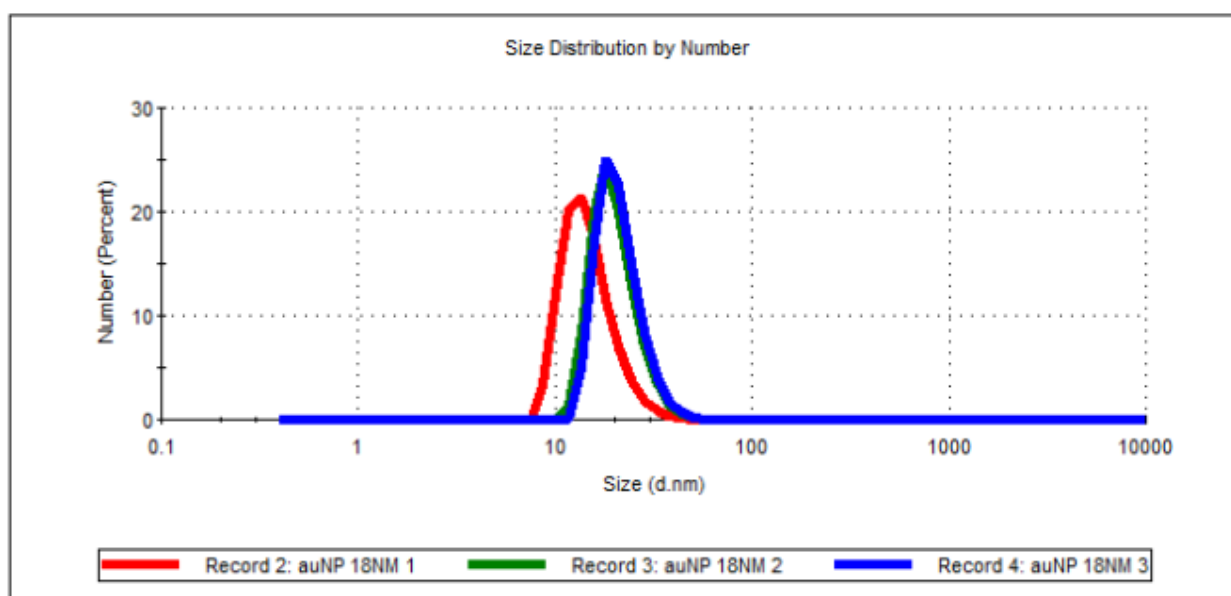
Figure 25: gold NPs in sodium borate buffer, after phase transfer using PMA. size distribution by number.

NPs in sodium borate buffer were precipitated using ultracentrifugation and the supernatant was diluted (or not, for control) by a known factor before resuspending the NPs and repeating this process five times. To assure that the changes in stability are a result of polymer removal and not the repeated centrifugation – all samples were centrifugated the same number of times. Later, polymer content in the supernatant/sediment was determined by fluorescence and NP's colloidal stability was assessed using optical absorption and DLS.

Figure 26 shows the PMA content in the NP suspension (NP+SUP) and in the supernatant (SUP) after different dilutions (determined by fluorescence). We anticipate the dilution of excess

polymer to follow the dilution of the supernatant (X axis of Figure 26), as is evident in the first three samples (dilutions 1, 30, 900). It appears that the excess of PMA in those samples (not on the NP's surface) greatly exceeds the polymer content attached to the NP, as evident by the similarity in PMA's concentration in the NP suspension and in the supernatant, as well as the good match of the regression line with a formula similar to Y=1/X, expressing simple dilution. In contrast, the next three samples break this trend, showing a slower reduction in PMA concentration. This "buffering effect" might be explained by removal of PMA from the NP's surface. This illustrates the problem of conjugating other materials to the NP through the surface – due to large excess of free polymer competing for conjugation. We estimate over 99% of the polymer is actually free in solution. Also, apparently, removal of excess polymer might destabilize the NP's colloidal stability.
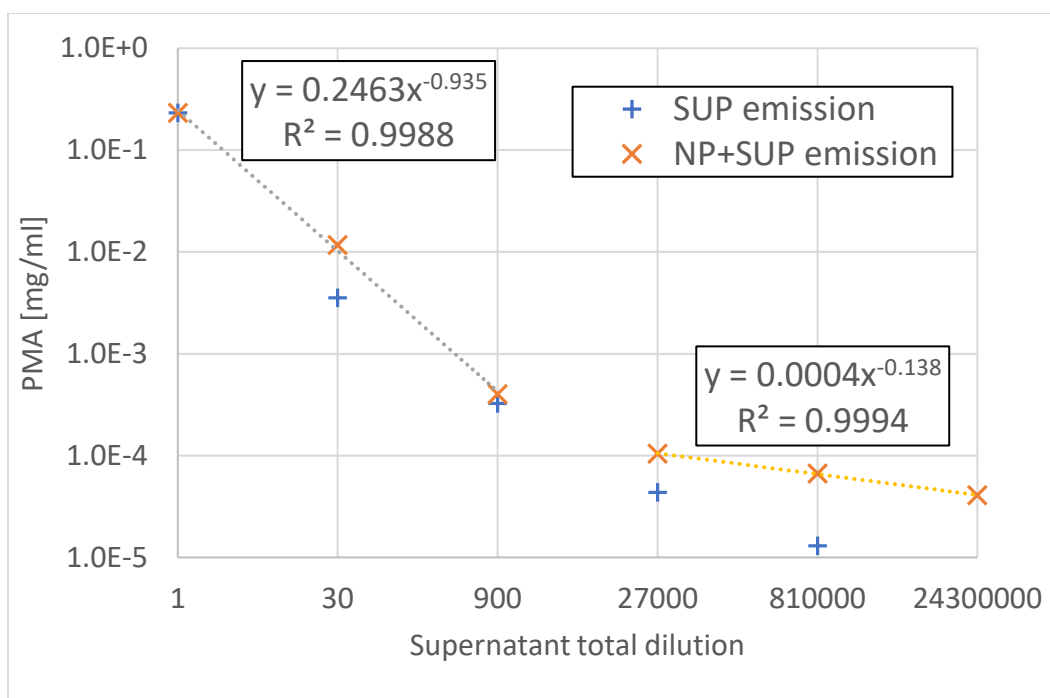
Figure 26: the concentration of PMA in the NP suspension and in the supernatant, as determined by fluorescent emission. In the first three samples (dilution of 1, 30, 900) the PMA concentration is reduced by the same factor as the total dilution, indicating removal of free excess polymer from the solution. In the next three samples (dilutions 27K, 810K, 24300K) the removal of PMA is "buffered". This can indicate the removal of PMA from the NP's surface.

Figure 27 illustrates the effect of polymer removal on the NP's colloidal stability. The yellow dots represent the yield of NPs immediately at the end of the centrifugation steps, as measured by UV absorbance (where fluorescence was measured). The other three colors were measured after three days of incubation in three different buffers. We found substantial amount of the NPs adsorbed to the glass and plastic containers used – for all samples except the undiluted (SUP dilution=1).
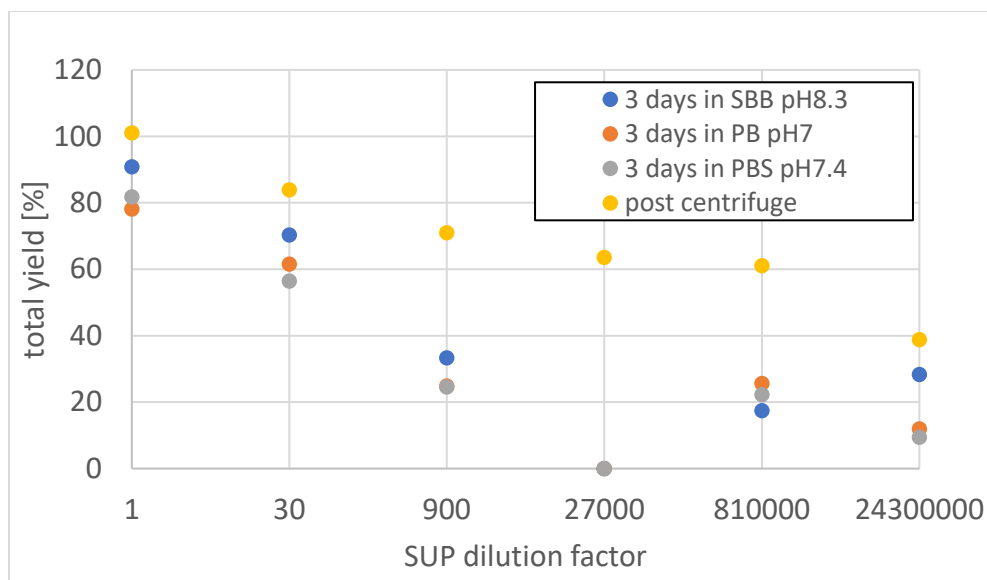
Figure 27: stability of the NPs throughout the centrifugation steps and 3 days after. All samples showed increased instability with further dilution.

In some of the samples (but not all), colloidal instability was also evident in the DLS spectra and the wavelength of the plasmon peak (sample 27000 had a drastic change in UV spectra that did not allow quantification after 3 days).

These results were reproduced with other NPs with different size and composition, illustrating this as a general limitation of the phase transfer method, calling for new solutions for the incorporation of hydrophobic inorganic NPs into drug delivery systems.

4.D - Preliminary evidence of drug delivery using PMA nanoparticles (VIVIT)

Tests of PMA coated iron oxide NPs as cytosolic drug delivery agents used VIVIT, an anti-inflammatory peptide as a model drug. Using these NPs, we demonstrated the inhibition of dendritic cells inflammatory response through cytosolic delivery of VIVIT in vitro and in vivo in mouse models (data not shown). This was the base and starting point for the endosomal escape related experiments of this work.

As suspensions of polymer caped inorganic NPs often contain a mixture of NPs and "empty" micelles and the subsequent surface chemistry is done through the polymer (and thus does not distinguish between them), we tested PMA micelles alone for their ability to escape the endosome. This is favorable in terms of nanocarrier's toxicity. As such, experiments using PMA micelles were conducted using similar concentration, i.e. the concentration used as surfactant for iron oxide NPs.

4.E - Hemolysis assay as model of endosomal escape through membrane destabilization

A brief description of this mechanism was given in chapter 1.C.vi and Figure 12, D. Red blood cells are frequently used to test material's ability to destabilize the plasma membrane, as a model of the endosomal membrane. For this purpose, erythrocytes were isolated from human blood through density gradient sedimentation and washed in pH 7.4 PBS. Different vials were loaded with erythrocytes, PMA and a citrate/phosphate buffer of a specific pH, and after a period of incubation erythrocytes were sedimented again by centrifugation. Leaked hemoglobin/heme was quantified by absorption, giving a measure of PMA's ability to destabilize the erythrocyte plasma membrane, as a model of the endosomal membrane. In some experiment results are presented as a fraction of the positive control (erythrocytes incubation in distilled water), however, due to differences between different batches of blood data should be compared only within each experiment (each graph) and some results are presented as measured absorption instead.

Figure 28 shows the hemolysis activity of PMA as function of PMA concentration (left) and incubation time (right), with monotonously increasing trends. Interestingly, cell lysis was limited to a narrow range of pH between pH 6.7-7 (while colloidal stability was maintained until pH 6). We further examined PMA's behavior below this range later (octanol/water distribution coefficient).
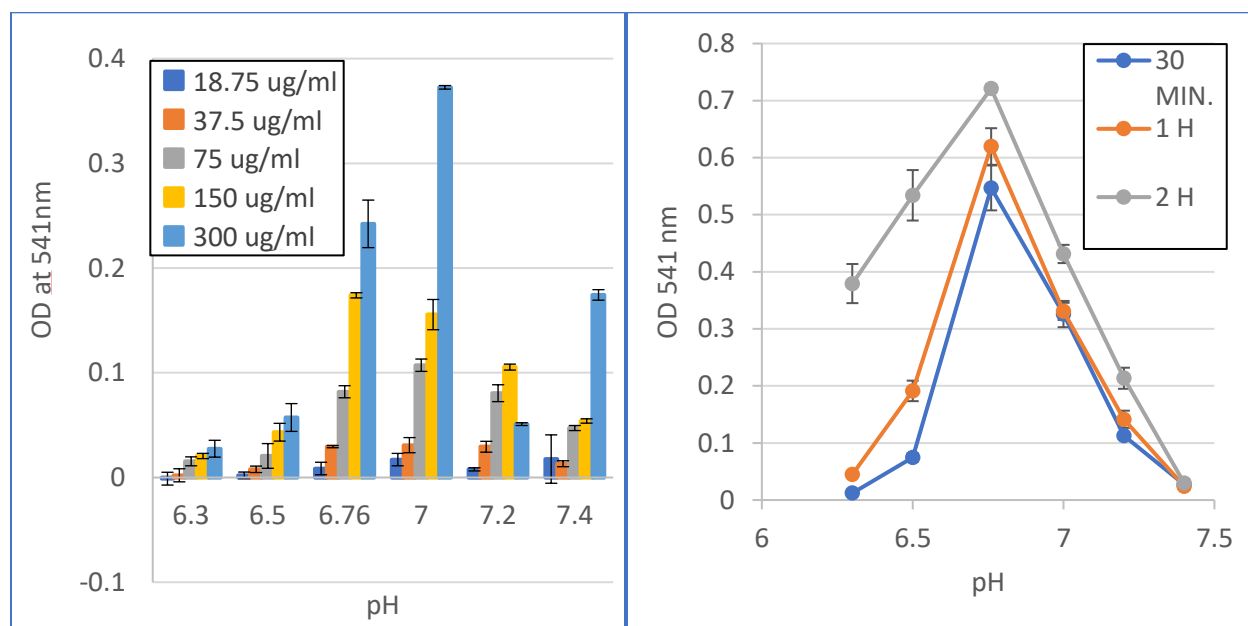
Figure 28: PMA hemolysis of erythrocytes at different pH. (left) increasing concentration of PMA leads to higher membrane permeabilization (after 30min). Likewise, (right) with longer incubation time (at 25 µg/ml). Interestingly, hemolysis was limited to a narrow range of pH between 6.7-7. Error bars represents standard deviation from triplicates.

We next tested the effect of the PMA monomer to dodecyl amine ratio, i.e., the micelles hydrophilic/hydrophobic volume ratio. Figure 29 shows the hemolysis pH profile of PMA functionalized with different amounts of dodecyl amine. The polymer narrow range of hemolytic activity was shifted to higher (80%) or lower (70%) pH depending on dodecyl amine content. This has been described in the literature for other polymeric NPs (for example [146]). This raise the

need to calibrate PMA's hemolysis pH profile to the pH profile of maturing endosomes (Figure 11). Our "standard" version of PMA with 75% dodecyl amine show good hemolysis between pH 6.7-7, which is not ideal given the endosome of most cells can reach pH 6.2 within 1-5 min. PMA with ~65% dodecyl amine might be more suited for endosomal escape. Alternatively, some specialized cells have basic endosomes that might require a different endosomolytic-pH profile[147].
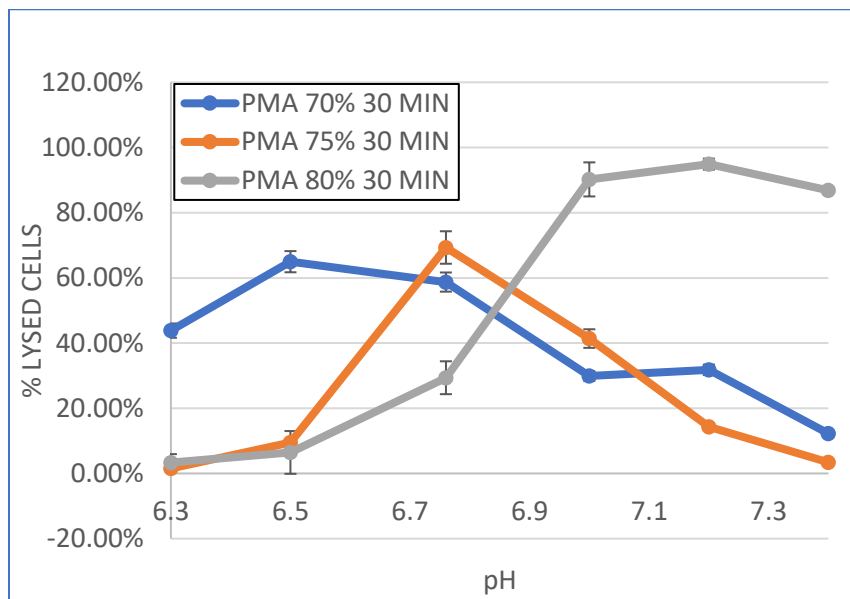
Figure 29: effect of hydrophilic/hydrophobic volume ratio on the hemolysis's pH profile at 75ug/ml. Reduced dodecyl amine content results in activation onset shifted to lower pH, and vice versa. Error bars represents standard deviation from triplicates.

To test the effect of plasma proteins, 1 mg/ml PMA was first incubated with varying concentration of blood plasma for 10 min, prior to testing its hemolytic activity. Figure 30 (left) shows this effect – a decrease in activity with increasing plasma concentration. We hypothesized this can be due to either (1) formation of a protein corona prior to pH change or (2) due to the plasma concentration in the presence of erythrocytes and specific pH. To discriminate between them, we conducted the experiment in Figure 30 (right): this time the plasma concentration was the same during preincubation with PMA but different during incubation with erythrocytes (while maintaining the same final PMA concentration). when pre-incubation was done using higher PMA concentration (leading to higher dilution subsequent dilution) – activity was higher. This demonstrates the different activity arise from the plasma concentration during hemolysis and not from pre-formed protein corona, assuming the formation of the protein corona did not substantially deplete the soluble protein content.
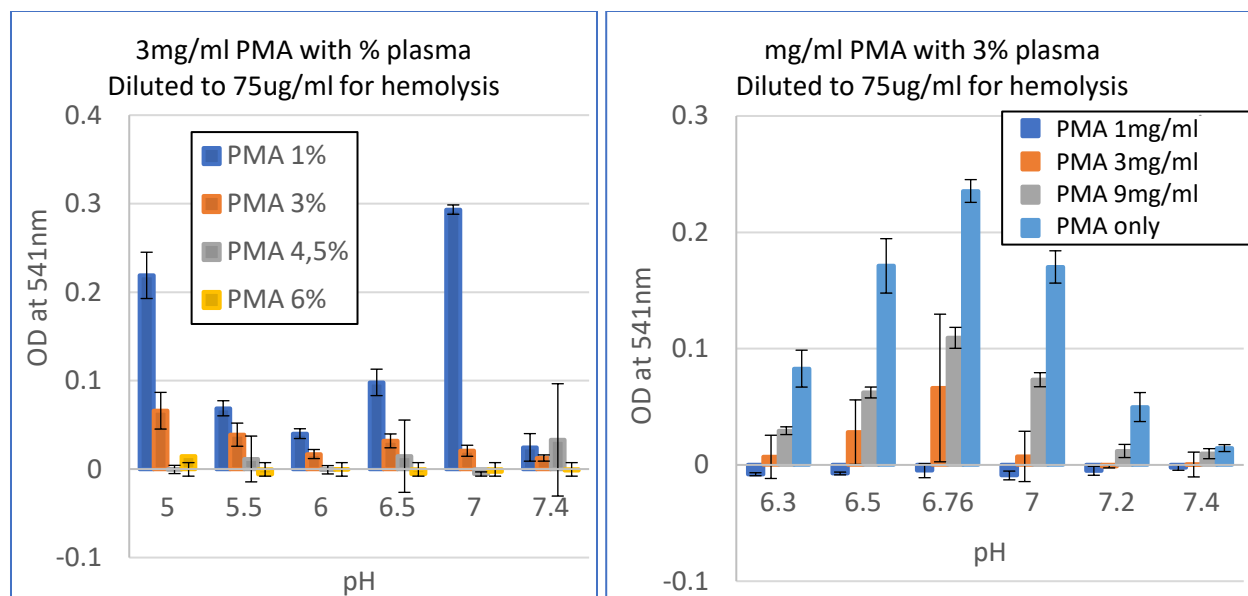
Figure 30: Influence of blood serum protein on PMA's hemolytic activity. (left) 3 mg/ml PMA was pre-incubated for 10 min with different plasma concentrations, and then diluted to 75 µg/ml for the hemolysis assay. This experiment indicated increased inhibition of hemolysis with increased plasma concentration. (right) in this modified version of the same experiment, different concentrations of PMA were pre-incubated with the same concentration of plasma, and finally diluted to 75 µg/ml PMA concentration for the hemolysis assay. This experiment indicated that hemolysis inhibition is a result of plasma concentration during the hemolysis assay, and not pre-formed protein corona.

As both hemolytic activity and plasma protein interactions are a function of the NP's surface charge and hydrophobicity, we tested the effect of modifying PMA with EDBE (Ethylenedioxy bis(ethylamine)). This modification could reduce PMA's surface hydrophobicity and net electric charge (reduction in hydrophobicity would result both from EDBE's amphiphilic nature and from the reduction of negative surface charge, which would allow further ionization of carboxylic groups).

EDBE was conjugated to PMA's carboxylic groups through a peptide bond. To verify this conjugation, we measured the presence of primary amines on PMA, as well as the change in DLS size and zeta potential. Figure 31 (left) shows increased levels of FITC binding to PMA micelles after functionalization with EDBE (verifying its conjugation). Figure 31 (right) shows the change in zeta potential. A substantial decrease in potential is seen with 9% EDBE. Presumably lower degree of functionalization indeed reduced surface energy, but further ionization of carboxylic groups "buffered" the change in zeta potential.
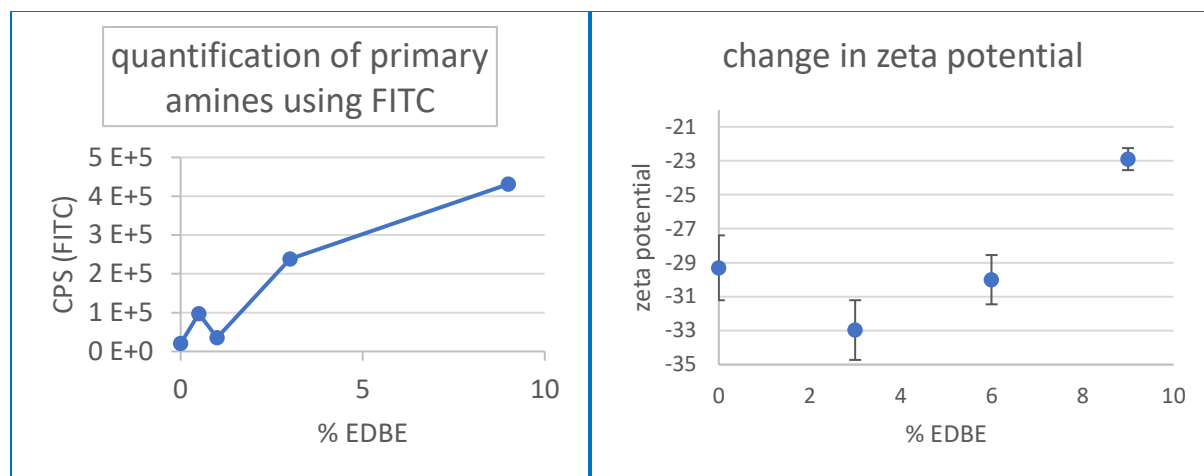
Figure 31: characterization of PMA-EDBE: (left) increased functionalization with EDBE was demonstrated through increased binding of FITC. (right) the effect of EDBE on micelle's surface energy is seen through change in zeta potential. A substantial change is evident from 9% EDBE functionalization (error bars are standard deviation of three measurements).

Testing this modified PMA with no plasma showed very similar results (Figure 32), while testing it with plasma showed increased hemolysis (or lower inhibition). This might be useful to improve the endosomal escape capability of this polymer. Likewise, it might allow longer circulation time in vivo, as reported for other zwitterionic NPs[73].
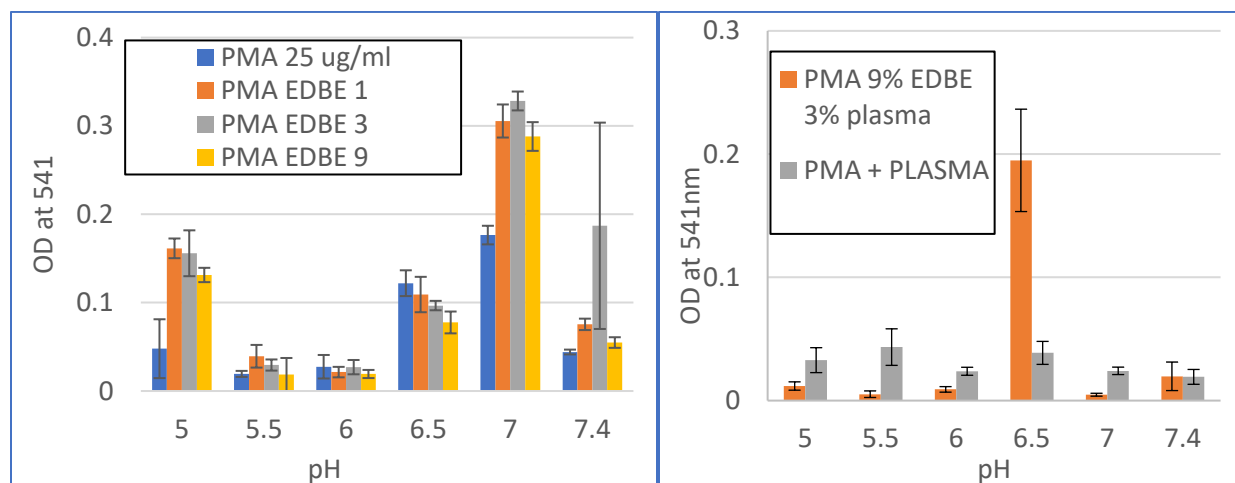
Figure 32: Hemolytic activity of PMA-EDBE. (left) testing EDBE modified PMA without plasma showed very similar activity profile. (right) in the presence of plasma however, PMA-EDBE (9%) showed less inhibition.

When interpreting results from this model, it is important to note that here plasma proteins concentration represents the concentration within the endosome. In vivo, different internalization mechanisms (e.g., micropinocytosis, in contrast to phagocytosis) and different stages of endosomal maturation might be different with this regard.

4.F - Octanol/water distribution coefficient as model of endosomal escape through direct diffusion

Considering a second mechanism for endosomal escape, we hypothesized the following mechanism of direct diffusion through the endosomal membrane. This mode of crossing the membrane is usually limited for amphiphilic molecules smaller than 500 Da. PMA has an average molecular weight of ~11300 Da, however, it can experience a dramatic change in hydrophilicity following endocytosis that is not typical for other molecules. By this model internalized PMA will lose its charge and hydrophilic surface due to acidification, resulting in penetration and solubilization of the polymer within the hydrophobic part of the membrane (Figure 33, right) as govern by its distribution coefficient. At this point, the polymer could also distribute itself into the more basic aqueous phase of the cytoplasm. To model this behavior, we used multiple biphasic systems at different pH (Figure 33, left). The aqueous phase was modeled with phosphate/citrate buffers at different pH, and the hydrophobic part of the membrane was modeled using octanol.

$$NP^W \overset{K}{\rightleftharpoons} NP^O$$

$$K = \frac{[NP]^O}{[NP]^W}$$
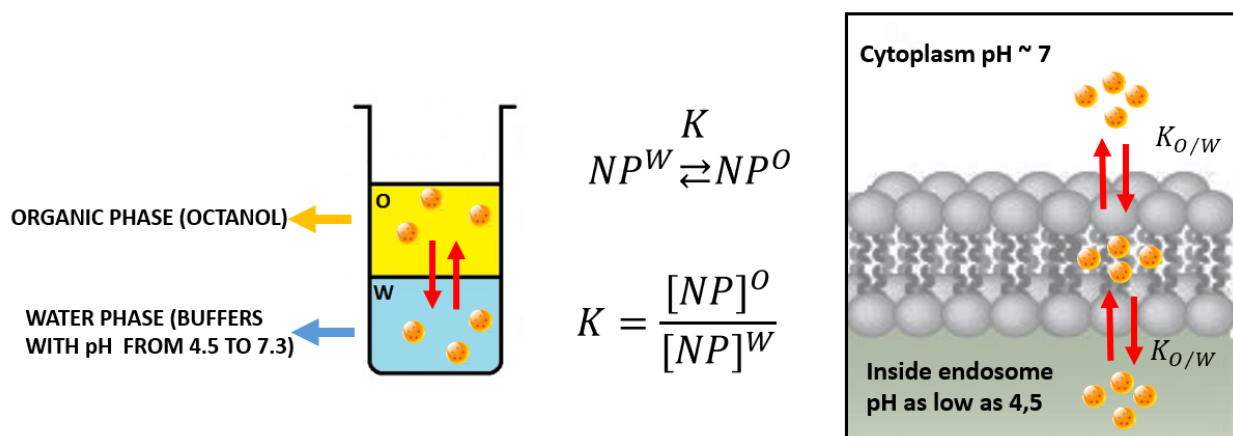
Figure 33: proposed mechanism (right) and experimental setup (left) for endosomal escape through direct diffusion.

PMA was labeled with a fluorescent dye and equilibrium concentration was quantified within the organic phase, while aqueous concentration was determined by calculation from total initial concentration. Thus, distribution coefficient calculated in this method are lower limits – under the assumption all other PMA is dispersed in the aqueous phase (in contrast to the interphase or the vial walls). We selected a dye known to have very low partition coefficient (thus limiting false positive signal from free dye)[148], as well as being pH-insensitive throughout the experimental pH. To test for any change in emission due to solvent, a sample of dye was dissolved in ethanol, and later diluted into water or octanol. The octanol solution had lower emission by a factor of 0.52. This was factored into the calculation of polymer concentration.

Figure 34 shows the change in PMA's distribution coefficient as pH is lowered to around 1. This value makes direct diffusion reasonable, within the limitation of the model.
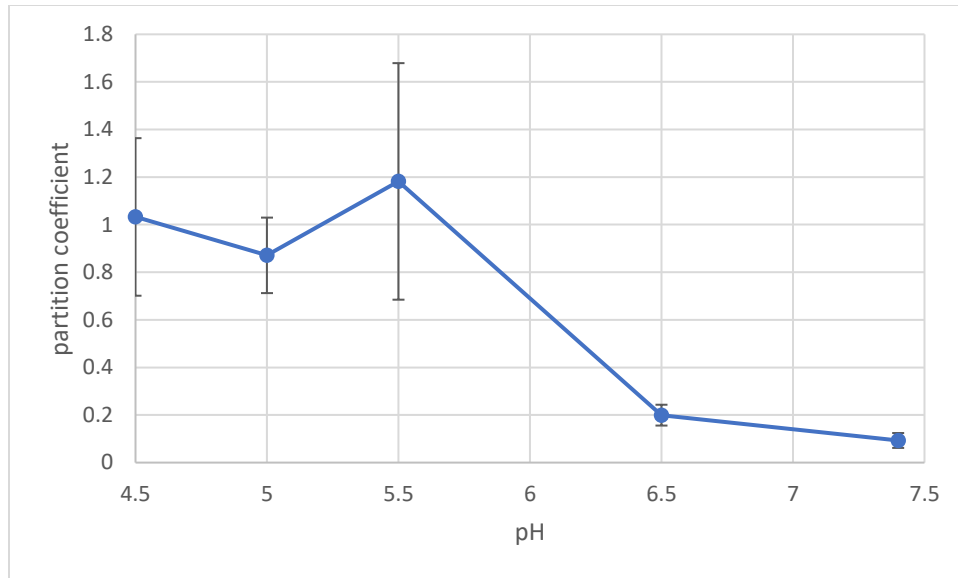
Figure 34: Distribution coefficient of PMA at different pH.

Next, we tested the effects of different DDA content and plasma concentration (Figure 35). Increased DDA content was found to increase PMA's migration to the organic phase and vice versa. Addition of plasma to the aqueous phase had an inhibitory effect on PMA's migration to octanol at very low concentrations (similar to the hemolysis assay). This might represent one of the limits of these models, as the concentration and identity of proteins inside the endosomal pathway is unclear.
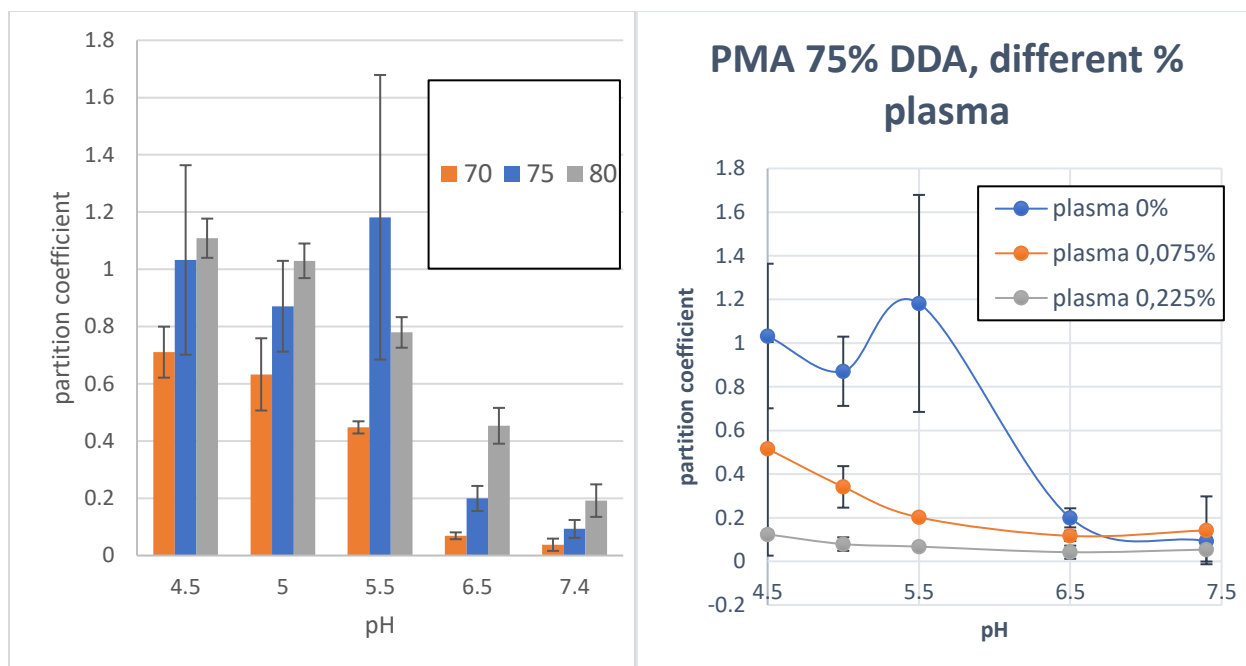
Figure 35: (left) effect of different DDA content on PMA's distribution coefficient. the general trend shows higher migration to organic phase with increasing DDA content, at all pH (error bars represent standard deviation of triplicates). (right) similar to the hemolysis assay, plasma was found to have an inhibitory effect, preventing migration of PMA to octanol (error bars represent standard deviation of three experiments).

Testing the effect of EDBE modification (reducing the surface free energy), PMA did not seem to change its migration to the octanol phase with or without plasma (Figure 36). Worth noting is the fact that this modification actually increases the degree of ionization of the polymer at each pH. This raise the question whether PMA is actually soluble in the octanol phase or forming reversed micelles, and if so, if it is a good representation of the biological membrane. This would have to be answered using real cellular membranes in the future.
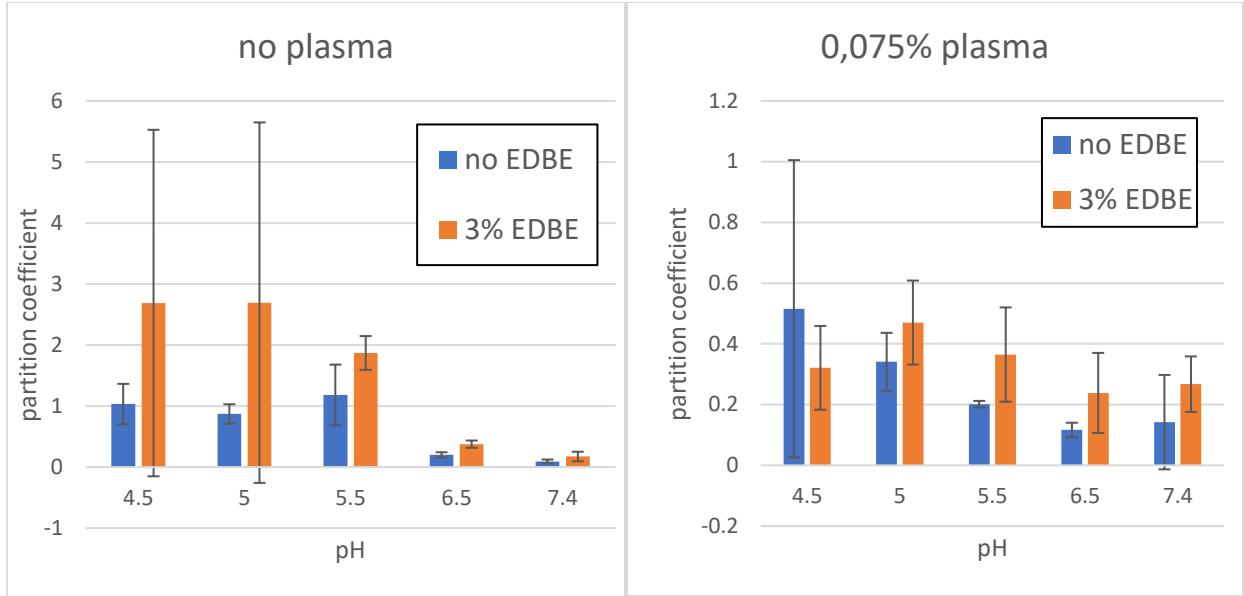
Figure 36: (left) EDBE modification of PMA did not have a clear effect on its octanol/water distribution with (right) and without (left) plasma (error bars represent standard deviation of triplicates).

4.G - Assessment of FRET as a tool to quantify cytosolic localization

To assess using FRET interaction between endogenic fluorescent protein and an externally administered fluorescent dye to quantify endosomal escape, and possibly identify specific fluorophore for the task we used a computational model. The FRET signal is defined as the ratio of fluorescent intensity with/without FRET (i.e., with/without endosomal escape) (Eq. 6). Note that with and without FRET, both the donor and acceptor contribute to the emission intensity (this is called "donor emission leak" and "acceptor absorption leak").

$$Eq.6 \quad signal = \frac{Em_{FRET}^{donor} + Em_{FRET}^{acceptor}}{Em_{No\ FRET}^{donor} + Em_{No\ FRET}^{acceptor}}$$

Given any FRET pair absorption spectra, we can use bear-lambert law to calculate the energy absorbed by each fluorophore (Eq. 7, ε is the extinction coefficient of wavelength λ_{Ex}, C is the fluorophore's concentration and l is the optical length

$$Eq.7 \quad I = I_0 * 10^{-\varepsilon(\lambda)*c*l} \quad \rightarrow \quad absorbed\ energy = I_0 - I$$

Estimating each fluorophore's average concentration (C_d, C_a) within the cell, the FRET distance (r, Eq. 3) and the degree of endosomal escape ($\%_{escape}$), we can calculate the total amount of energy transfer (Eq. 8). The donor energy over donor concentration gives the energy per molecule, the acceptor concentration times the percent of endosomal escape gives the number of molecules exchanging energy through FRET, and E (Eq. 3) is the fraction of energy transferred per interaction.

44

$$Eq. 8: \quad total\ energy\ transfer = \frac{donor\ energy}{C_d} * (C_a * \%_{escape}) * E$$

Lastly, given each fluorophore's energy, we can calculate the emission using the normalized emission spectra and quantum yield (QY) (Eq. 9). In this context, normalized means total area under curve equal 1.

$$Eq. 9 \quad Em_{FRET} = (absorbed\ energy \mp transfered\ energy) * QY * normalized\ Em(\lambda)$$

Considering for example the fluorescent protein DsRed-Express (QY=0.44, ε=44,000 $M^{-1} * cm^{-1}$) as FRET donor and Alexa Fluor 750 (QY=0.12, ε=290,000 $M^{-1} * cm^{-1}$) as acceptor (Absorption and emission spectra in **Error! Reference source not found.**, best FRET parameters in Table 1).
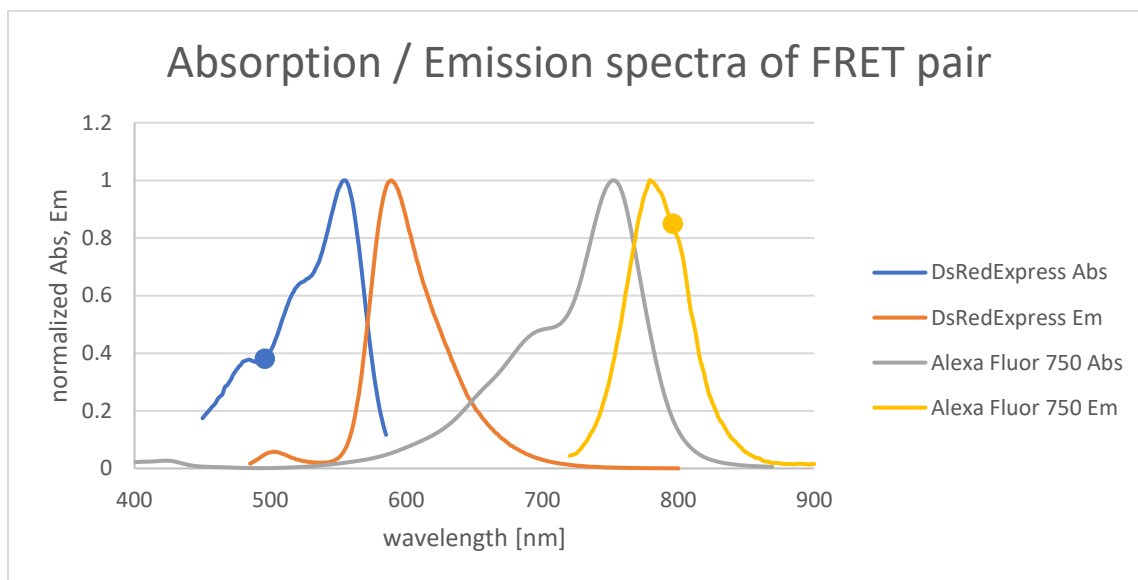
Figure 37: Example of absorption and emission spectra of a FRET pair. Optimal wavelengths for excitation (494 nm) and emission (789 nm) are marked on curve. The signal was averaged over 20 nm wavelength range. Note that both are different than the fluorophore's peak absorption/ emission.

We calculated the FRET constant and the anticipated FRET signal in each absorption and emission wavelength, assuming **10% endosomal escape** (this would reflect the sensitivity of such assay, higher percent would give stronger signal), **FRET distance of 4 nm** (this is a lower limit estimation, as the size of the fluorescent protein itself and the need for a binding agent between it and the drug delivery system would probably dictate a longer distance, which would result in lower signal), **donor concentration of 5 μM** and **acceptor concentration of 1 μM** (important here is the ratio between these concentrations. The fluorescent protein concentration is a low estimate based on published work[149,150], this of course is cell and expression system dependent. Both articles report a variance of order of magnitudes in this value between cells. The acceptor concentration was estimated using the uptake of fluorescein labeled PMA micelles. These parameters would give the highest signal when the concentration within the cytoplasm are equal,

meaning in this case $C_{acceptor}*\%_{escape}=C_{donor}$). The emission intensities were averaged over 20 nm to avoid artifacts and simulate the monochromator's band width.

Processing these spectra using these parameters yielded the result presented in Figure 38 and the highlighted line of Table 1.
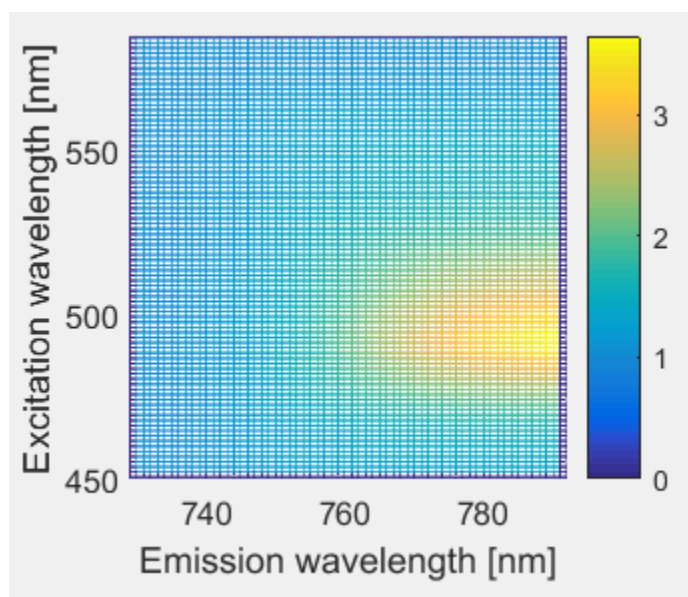
Figure 38: software output for a FRET pair candidate (donor: DsRedExpress, acceptor: Alexa fluor 750). The software calculates the FRET signal for all excitation and emission wavelengths. The maximum signal is presented in Table 1.

Table 1: representative output of different FRET pair candidates. All calculations assumed FRET distance of 4 nm, 10% endosomal escape, 5 µM fluorescent protein and 1 µM organic dye. All tested dye's spectra were either from the website of the manufacturer's website or from reference [151,152]

donor	acceptor	max signal	Em [nm]	Ex [nm]	R_0 [Å]
DsRedExpress	alexa fluor 750	3.65	789	494	60.50
DsRedExpress2	alexa fluor 750	3.58	789	494	60.49
mKO	alexa fluor 647	2.55	685	471	62.21
EGFP	alexa fluor 647	2.16	669	471	49.94
HcRed1	alexa fluor 647	1.98	699	412	49.31
ZsGreen1	alexa fluor 594	1.78	634	456	56.03
alexa fluor 488	TagRFP	1.28	663	450	62.94
alexa fluor 488	mPlum	1.23	663	479	54.96

The maximal anticipated signal for DsRedExpress and Alexa Fluor 750 was 3.65, the highest of all tested combinations. This value can theoretically be improved by using FRET pairs with better spectral separation, e.g., using high stokes shift fluorophores or quantum dots, however these might be limited by low quantum yield or compatibility with our hypothesized assay. At this point,

due to the low anticipated signal and high complexity of such experimental system, we decided to try other methods for endosomal escape quantification (using CrAsH-EDT$_2$).

4.H - CrAsH-EDT2 as a sensor to quantify endosomal escape

Previous reports using FlAsH and CrAsH showed a ~40 times increase in the fluorophore's emission after binding to its target sequence. Compared to the data presented in Table 1, this would mean a "max signal" of 4.9 (assuming 10% endosomal escape). This higher dynamic range, as well as not requiring a third molecular recognition function (unlike the hypothesized FRET system) made CrAsH a better choice for this experiment. To test the use of CrAsH as a sensor of endosomal escape we designed an expression plasmid of a blue fluorescent protein-Cys4 fusion (BFP-Cys4), and conjugated CrAsH to the surface of different NPs reported to be able to reach the cytoplasm. Cytoplasmic localization of a nanocarrier would result in CrAsH-Cys4 binding and a measurable increase in fluorescence (Figure 39).
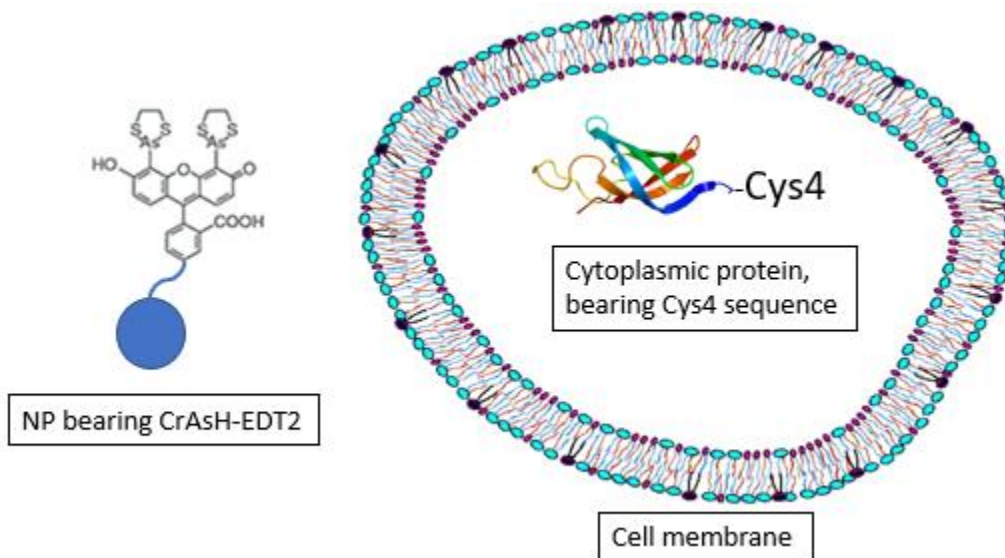
Figure 39: Cartoon depicting the proposed method for quantification of cytosolic localization. The pro-fluorophore CrAsH becomes fluorescent only after binding to the genetically encoded Cys4 tag.

As a first step, each component (transgenic cells and NP-CrAsH) was characterized separately. To demonstrate the recognition between CrAsH and the expressed BFP-Cys4 protein, transgenic cells were treated with FlAsH-EDT$_2$, the cell permeable version of CrAsH, and cells were analyzed by flow cytometry (Figure 40). Compared to untreated cells (UTR), cells transfected with an expression plasmid for BFP with (BFP+T) or without (BFP-T) the Cys4 tag showed a wide range of emission intensities in the blue channel, correlated to the concentration of the Cys4 tag; cells treated only with FlAsH (FlAsH only) showed a uniform shift in the green channel compared to untreated cells (related to the pro-fluorophore basal brightness). Cells transfected with BFP-T (fluorescent protein without Cys4 tag) AND FlAsH showed the combination of both – a wide range of blue together with a uniform increase in green. Finally, cells transfected with BFP+T (fluorescent protein fused to the Cys4 tag) AND FlAsH showed a dependence between the green

and blue channels, i.e., the higher the blue signal the higher was the green - high BFP+T expressing cells had ~11 times higher green emission intensity compared to cells expressing low BFP+T in the same sample. This is due to binding of FlAsH to the Cys4 tag and following increase in its brightness. Other published work state a higher dynamic range of emission between on-off states of FlAsH (and CrAsH, around 35 times increase[143]). The lower relative increase can result from both decomposition of FlAsH back to fluorescein (more relevant in the case of CrAsH [153]), or from partial oxidation of FlAsH or EDT. The later can be prevented by using specific reducing agents to the experiment medium. Specifically, TCEP and mercapto-ethanesulfonate were found to be effective at lowering the basal emission and improving this dynamic range.
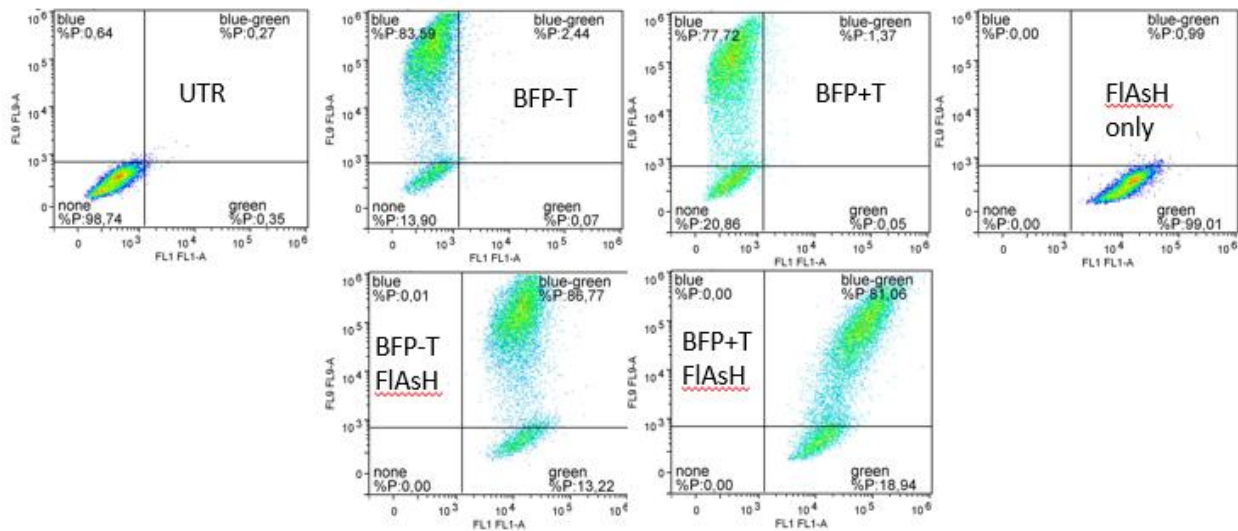
Figure 40: Flow cytometry analysis of HeLa cells with and without the expression plasmid and free cell permeable FlAsH. Each graph shows the green emission on the horizontal axis (originating from FlAsH), and the blue emission on the vertical axis (originating from BFP, proportional to Cys4) of each cell.

CrAsH was conjugated to PMA's carboxylic groups through a diamine linker (EDBE), as well as to polyethyleneimine, a polymer reported to be capable of endosomal escape[120,123] (used as positive control). We then tested the binding of conjugated CrAsH to a chemically synthesized Cys4 peptide (not fused to BFP). Figure 41 shows the relative increase in conjugated CrAsH emission after binding to Cys4, as well as free CrAsH activated with lysed cells transfected with BFP+T (mtag+T) for comparison. PEI-CrAsH and free CrAsH had very similar response, ultimately increasing by about 11-fold; in contrast, PMA-CrAsH had lower/slower increase in emission. This might be due to steric inhibition of CrAsH-Cys4 binding and might be improved by using a different linker or better control of pH and ionic strength (as they both affect PMA's aggregation state and micelle size). Maximizing this response is critical, as it determines the assay sensitivity and accuracy. In later experiments, this dynamic range was improved to about 35 by adding the above-mentioned reducing agents.
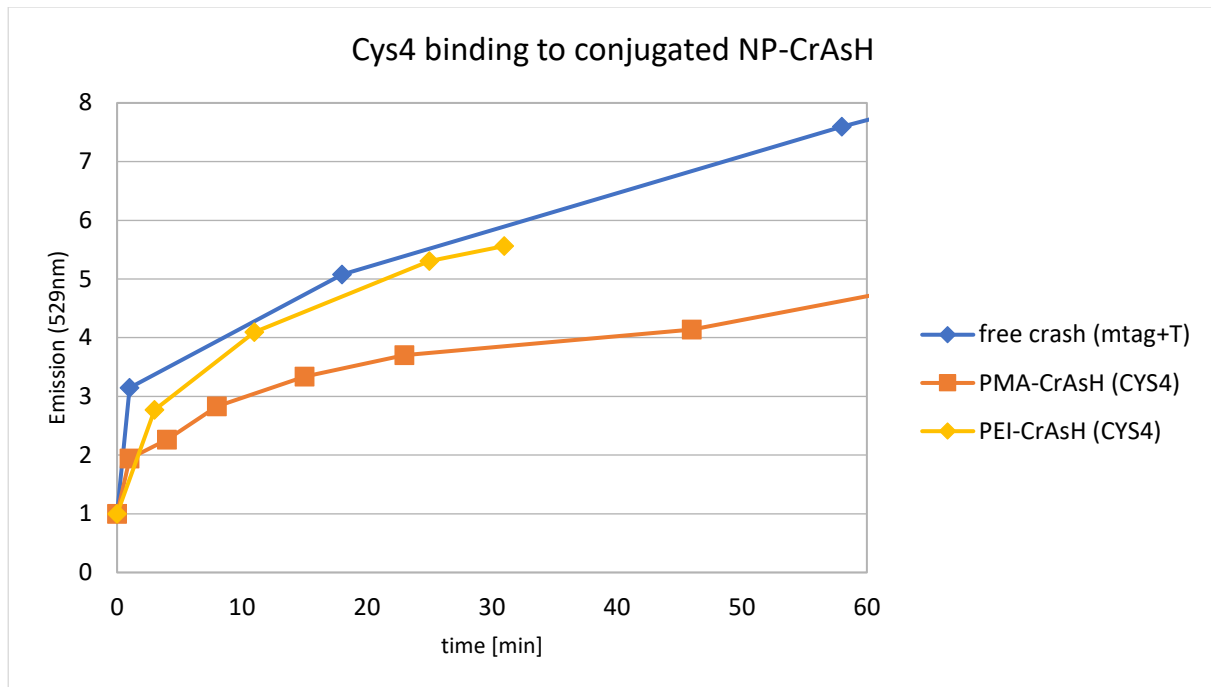
Figure 41: NP-CrAsH binding to Cys4. PMA-CrAsH showed lower binding/increase in emission compared to free CrAsH and PEI-CrAsH.

Seeing that both component – BFP-Cys4 expressing cells and NP-CrAsH – were working, we aimed at testing them together. To assure enough cellular uptake of each NP, we conjugated carboxy fluorescein to PMA and PEI using the same conjugation method (to obtain the same degree of labeling) and tested different NP concentration and incubation times with the cells. As seen in Figure 42, NP's uptake plateaued after 2 h and we chose that period of incubation; the dose was chosen to have an intensity increase higher than 10, i.e., 90 µg/ml for PMA and 97.2 µg/ml for PEI.
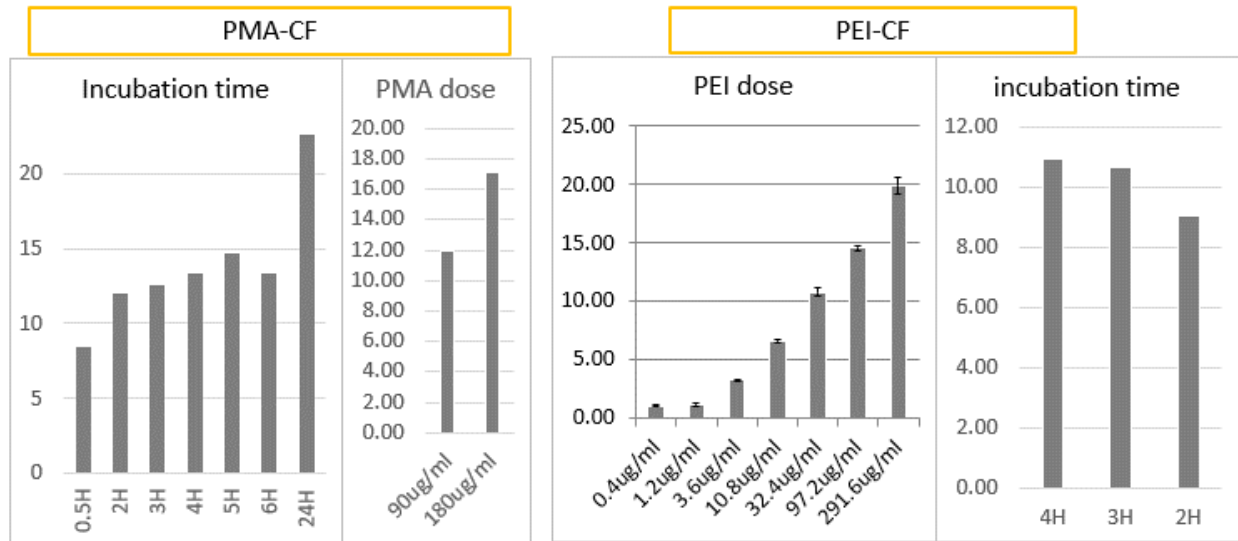
Figure 42: Cellular uptake of PEI-CF and PMA-CF. this data was used to find the optimal dose and concentration for the later NP-CrAsH experiment, such that the signal intensity would be high enough.

Next, BFP-Cys4 expressing cells were treated with PEI-CrAsH or PMA-CrAsH. We chose HeLa cells for PEI, as previous reports showed good ability of PEI to escape the their endosomes[123]. Figure 43 shows the flow cytometry data of PEI-CrAsH administered to BFP-Cys4 expressing HeLa cells. After two hours of incubation the PEI was replaced with cell medium, and after another hour cells were harvested and analyzed. All the control sample (UTR, BFP-T, BFP+T, PEI-CrAsH, BFP-T + PEI-CrAsH) looked like previous test with FlAsH (Figure 40), i.e., no green-blue dependence. In the sample with BFP+T and PEI-CrAsH there was a slight dependence, about 4-fold increase in green in high intensity blue cells compared with low intensity blue. A separate control ruled out the possibility of residual free CrAsH to penetrate the cells (even at high concentrations). These controls prove the signal is a result of endosomal escape of PEI.
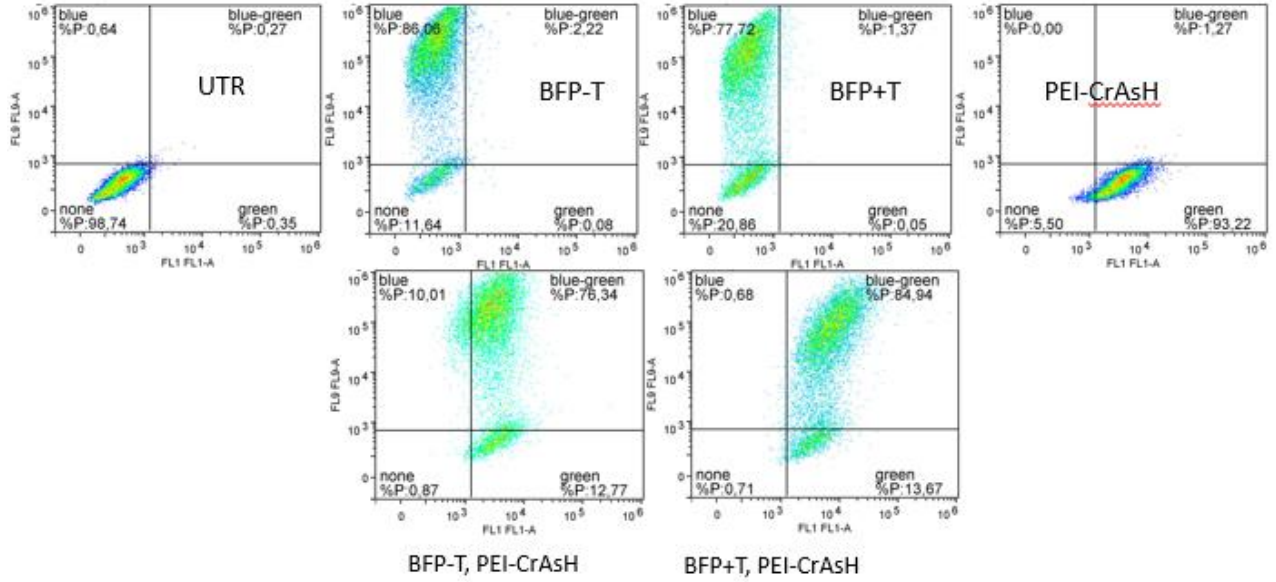
Figure 43: Positive control for NP-CrAsH endosomal escape test. Green-blue dependence in BFP+T and PEI-CrAsH sample indicate measurable degree of endosomal escape. The

To translate the shift in emission to the yield of endosomal escape, we assume the green emission can be described as:

$$Eq.\,10 \quad green\;emission = \left(e * D_{off}^{on} + q\right) * C + B$$

$$e + q = 1$$

Where B is the background autofluorescence of thee cell, C is a parameter describing the brightness of CrAsH, q is the fraction of PEI-CrAsH trapped inside endosomes (and therefore unbound to Cys4), e is the PEI-CrAsH fraction that reached the cytoplasm (and therefore is bound to Cys4) and D_{off}^{on} represent the brightness dynamic range between on-off states. Assuming the contribution of B can be neglected and that the uptake of PEI-CrAsH by cells is not affected by their level of BFP expression, we get:

$$Eq.\,11 \quad green\;emission(no\;BFP, e = 0, q = 1) = C$$

So, by dividing the green emission of cells with high BFP expression with the green emission of cells with no BFP expression we get:

$$Eq.\,12 \quad green\;ratio = e * D_{off}^{on} + q$$

$$Eq.\,13 \quad e + q = 1$$

For the dynamic range, we can use the value D=11, obtained from using PEI-CrAsH activated using free soluble Cys4 (figure 37). The range of recorded emissions in the blue channel (for sample BFP+T, PEI-CrAsH) was from about 1E+1 to 1.1E+6. We define the range 0-2E+3 (including 99% of not transfected cells) as "no BFP" and the range 2E+5-1.1E+6 as cells expressing high BFP. We then calculate the average green intensities from each of these groups (within the same sample).

Dividing these values will give "green ratio", that will be used to calculate the yield of endosomal escape (using equations 12 and 13). The results of these calculations are presented in Table 2. Further tweaks could probably increase the sensitivity and accuracy of this method, however, these results suggest it is a viable method for quantification of endosomal escape. To our knowledge, this is the first example showing a reliable method to allow the determination of the ratio of successfully escaped NPs.

Table 2: Average emission values and endosomal escape yield. Results in duplicates.

Sample	Green average $_{no\ BFP}$ (number of cells)	Green average $_{high\ BFP}$ (number of cells)	Green ratio	Endosomal escape yield	Comment
BFP+T, PEI-CrAsH	3702 (2543)	16574 (1605)	4.477	34.77%	Sample
	4158 (2179)	18369 (1412)	4.418	34.18%	
BFP-T, PEI-CrAsH	4129 (1941)	4158 (3175)	1.007	0.07%	Negative control
	4537 (1455)	4486 (3161)	0.989	-0.11%	

The next step in this project would be to test also PMA, as well as other type of cells and drug delivery agents. We hope this could be a general method for the quantification of endosomal escape.

Chapter 4: Conclusion

The aim of this work was to further our understanding and abilities in the field of nanoparticle-based drug delivery. Our local starting point within this field was based upon two previously running projects. The first one was aimed at illustrating the effect of molecular recognition ligand density on drug delivery in vivo (chapter 4.B). After completing that project, we raised questions regarding the effectivity of conjugating ligands to inorganic NPs using their surface coating. Our follow up study (chapter 4.C) illustrated the problem of having excess polymer free in solution and prompted the development of better techniques for phase transfer. To our knowledge, this is the first comprehensive study highlighting the impact of previously unexplored features relating to colloidal stability of polymer-coated nanocrystals in a biofriendly environment. In light of the broad utilization of polymeric coating strategies to improve the biological stability of colloidal nanoparticles for nanomedicine application, our results are particularly relevant in order to improve our understanding of such multifaceted phenomena. We are currently working to develop reliable solutions in this direction.

The second project started from the implementation of PMA-coated iron oxide NPs as drug delivery agents to the cellular cytoplasm. Previous experiments already showed successful, although inconsistent delivery of a peptide drug (chapter 4.D). Our mission was to find the mechanism of delivery (with endosomal escape as the critical step) and provide the means to quantify delivery and improve reproducibility.

We proposed two possible mechanisms – endosomal escape through membrane destabilization (chapter 4.E) and endosomal escape through direct diffusion (chapter 4.F), and PMA's ability to permeabilize or cross the endosomal membrane was demonstrated using two suitable models. These models later allowed for the qualitative exploration of different effects on PMA's endosomal escape capability. Namely, the effects of plasma proteins, PMA's hydrophobic content and PMA's surface free energy were investigated. The results showed a strong inhibitory effect of plasma protein on membrane crossing in both models, however, we also saw that fine tuning of the surface free energy could help mitigate this effect in the hemolysis model. Furthermore, the need to match the hemolysis-pH profile of the polymer to the target cell's endosomal pH became evident. This could be done through changing the polymer hydrophobic content.

In order to quantify the degree of endosomal escape, we initially evaluated the use of a FRET signal between an exogenic organic dye conjugated to the NPs and a fluorescent protein expressed inside the cell's cytoplasm (chapter 4.G). After calculating the estimated signal from such a system with different fluorophores, we concluded that this method was not practical for this application. The Matlab tool, however, might be generally useful when considering using FRET and assist in choosing a good FRET pair.

As an alternative to FRET, we chose a pro-fluorophore capable of recognizing a peptide tag resulting in the production of a fluorescent signal (chapter 4.H). After setting up this system and

characterizing its separate components, we were able to quantify the endosomal escape percentage of PEI, a polymer known to be able to reach the cytoplasm. This system must still be optimized and tested for its reproducibility. Specifically, we hope this will help in improving our PMA based delivery system, as well as have a general impact in this field, where the inability to quantify delivery hinders development of new efficient drug carriers.

This work is significant in both highlighting limitations in currently used methods and necessary improvements (phase transfer techniques), and in enabling better characterization of delivery methods (endosomal escape mechanism and quantification). We hope that this will lead to new solutions of nano-particles based drug delivery and improved healthcare.

Publications

Tumour homing and therapeutic effect of colloidal nanoparticles depend on the number of attached antibodies, Miriam Colombo, Luisa Fiandra, Giulia Alessio, Serena Mazzucchelli, Manuela Nebuloni, Clara De Palma, Karsten Kantner, Beatriz Pelaz, **Rany Rotem**, Fabio Corsi, Wolfgang J. Parak & Davide Prosperi, **Nature Communications volume 7, (2016)**

Bioengineered approaches for site-orientation of peptide-based ligands of nanomaterials, Svetlana Avvakumova, Miriam Colombo, Elisabetta Galbiati, Serena Mazzucchelli, **Rany Rotem** & Davide Prosperi, in "**Biomedical Applications of Functionalized Nanomaterials**", **(2018)** Chapter 6, pp. 139-169. Eds. B. Sarmento, J. das Neves. Elsevier, 1st Edition, ISBN: 978-0-323-50878-0.

References

[1]   Borm PJA, Robbins D, Haubold S, Kuhlbusch T, Fissan H, Donaldson K, et al. The potential risks of nanomaterials: A review carried out for ECETOC. Part Fibre Toxicol 3;(2006).

[2]   Cao G. Nanostructures & nanomaterials: synthesis, properties & applications. 1st ed. imperial college press; (2004).

[3]   Bera D, Qian L, Tseng TK, Holloway PH. Quantum dots and their multimodal applications: A review. Materials (Basel) 3;(2010):2260–345.

[4]   Ferrari M. Cancer nanotechnology: Opportunities and challenges. Nat Rev Cancer 5;(2005):161–71.

[5]   Albanese A, Tang PS, Chan WCW. The Effect of Nanoparticle Size, Shape, and Surface Chemistry on Biological Systems. Annu Rev Biomed Eng 14;(2012):1–16.

[6]   Daniel MC, Astruc D. Gold Nanoparticles: Assembly, Supramolecular Chemistry, Quantum-Size-Related Properties, and Applications Toward Biology, Catalysis, and Nanotechnology. Chem Rev 104;(2004):293–346.

[7]   Wang C, Huang Z, Lin Y, Ren J, Qu X. Artificial DNA nano-spring powered by protons. Adv Mater 22;(2010):2792–8.

[8]   Esfand R, Tomalia DA. Poly(amidoamine) (PAMAM) dendrimers: From biomimicry to drug delivery and biomedical applications. Drug Discov Today 6;(2001):427–36.

[9]   Gong J, Chen M, Zheng Y, Wang S, Wang Y. Polymeric micelles drug delivery system in oncology. J Control Release 159;(2012):312–23.

[10]   Sercombe L, Veerati T, Moheimani F, Wu SY, Sood AK, Hua S. Advances and challenges of liposome assisted drug delivery. Front Pharmacol 6;(2015).

[11]   Grimsdale AC, Müllen K. The chemistry of organic nanomaterials. Angew Chemie - Int Ed 44;(2005):5592–629.

[12]   Briseno AL, Mannsfeld SCB, Jenekhe SA, Bao Z, Xia Y. Introducing organic nanowire transistors. Mater Today 11;(2008):38–47.

[13]   Temirov R, Soubatch S, Luican A, Tautz FS. Free-electron-like dispersion in an organic monolayer film on a metal substrate. Nature 444;(2006):350–3.

[14]   Lu J, Liong M, Zink JI, Tamanoi F. Mesoporous silica nanoparticles as a delivery system for hydrophobic anticancer drugs. Small 3;(2007):1341–6.

[15]   Colombo M, Fiandra L, Alessio G, Mazzucchelli S, Nebuloni M, De Palma C, et al. Tumour homing and therapeutic effect of colloidal nanoparticles depend on the number of attached antibodies. Nat Commun 7;(2016).

[16]   Mokari T, Rothenberg E, Popov I, Costi R, Banin U. Selective growth of metal tips onto semiconductor quantum rods and tetrapods. Science (80-) 304;(2004):1787–90.

[17]   Pinzón JR, Villalta-Cerdas A, Echegoyen L. Fullerenes, Carbon Nanotubes, and Graphene for Molecular Electronics. Unimolecular Supramol. Electron. I, vol. 312, (2011), p. 127–74.

[18]   Chen J, Saeki F, Wiley BJ, Cang H, Cobb MJ, Li ZY, et al. Gold nanocages: Bioconjugation and their potential use as optical imaging contrast agents. Nano Lett 5;(2005):473–7.

[19]   Yuan H, Khoury CG, Hwang H, Wilson CM, Grant GA, Vo-Dinh T. Gold nanostars: Surfactant-free synthesis, 3D modelling, and two-photon photoluminescence imaging. Nanotechnology 23;(2012).

[20]   Avvakumova S, Galbiati E, Sironi L, Locarno SA, Gambini L, Macchi C, et al. Theranostic Nanocages for Imaging and Photothermal Therapy of Prostate Cancer Cells by Active Targeting of Neuropeptide-Y Receptor. Bioconjug Chem 27;(2016):2911–22.

[21]   Park J, Lee E, Hwang N-M, Kang M, Kim SC, Hwang Y, et al. One-Nanometer-Scale Size-Controlled Synthesis of Monodisperse Magnetic Iron Oxide Nanoparticles. Angew Chemie 117;(2005):2932–7.

[22]   O'Brien S, Brus L, Murray CB. Synthesis of monodisperse nanoparticles of barium titanate: Toward a generalized strategy of oxide nanoparticle synthesis. J Am Chem Soc 123;(2001):12085–6.

[23]   Park J, Kang E, Son SU, Park HM, Lee MK, Kim J, et al. Monodisperse nanoparticles of Ni and NiO: Synthesis, characterization, self-assembled superlattices, and catalytic applications in the suzuki coupling reaction. Adv Mater 17;(2005):429–34.

[24]   Ebert P. Nano-scale properties of defects in compound semiconductor surfaces. Surf Sci Rep 33;(1999):121–303.

[25]   Liqiang J, Yichun Q, Baiqi W, Shudan L, Baojiang J, Libin Y, et al. Review of photoluminescence performance of nano-sized semiconductor materials and its relationships with photocatalytic activity. Sol Energy Mater Sol Cells 90;(2006):1773–87.

[26]   Kong M, Li Y, Chen X, Tian T, Fang P, Zheng F, et al. Tuning the Relative Concentration Ratio of Bulk Defects to Surface Defects in TiO2 Nano Crystal Leads to High Efficient Photocatalytic Efficiency. J Am Chem Soc 133;(2011):16414–7.

[27]   Thanh NTK, Maclean N, Mahiddine S. Mechanisms of nucleation and growth of nanoparticles in solution. Chem Rev 114;(2014):7610–30.

[28]   Rao CNR, Govindaraj A, Vivekchand SRC. Inorganic nanomaterials: current status and future prospects. Annu Reports Sect A Inorg Chem 102;(2006):20.

[29]   Dresselhaus MS, Dresselhaus G, Eklund PC. Science of fullerenes and carbon nanotubes. Academic Press; (1996).

[30]   Balzani V, Credi A, Raymo FM, Stoddart JF. 49. Artificial molecular machines. Angew Chemie - Int Ed 39;(2000):104–16.

[31]   Lu AH, Salabas EL, Schüth F. Magnetic nanoparticles: Synthesis, protection, functionalization, and application. Angew Chemie - Int Ed 46;(2007):1222–44.

[32]   Ananikov VP, Orlov N V., Beletskaya IP, Khrustalev VN, Antipin MY, Timofeeva T V. New approach for size- and shape-controlled preparation of Pd nanoparticles with organic ligands. Synthesis and application in catalysis. J Am Chem Soc 129;(2007):7252–3.

[33]   Brown PR, Kim D, Lunt RR, Zhao N, Bawendi MG, Grossman JC, et al. Energy level modification in lead sulfide quantum dot thin films through ligand exchange. ACS Nano 8;(2014):5863–72.

[34]   Zhang T, Ge J, Hu Y, Yin Y. A general approach for transferring hydrophobic nanocrystals into water. Nano Lett 7;(2007):3203–7.

[35]   Yang J, Lee JY, Ying JY. Phase transfer and its applications in nanotechnology. Chem Soc Rev 40;(2011):1672–96.

[36]   Ben-Shahar Y, Scotognella F, Waiskopf N, Kriegel I, Dal Conte S, Cerullo G, et al. Effect of surface coating on the photocatalytic function of hybrid CdS-Au nanorods. Small 11;(2015):462–71.

[37]   Soliman MG, Pelaz B, Parak WJ, Del Pino P. Phase transfer and polymer coating methods toward improving the stability of metallic nanoparticles for biological applications. Chem Mater 27;(2015):990–7.

[38]   Mandzy N, Grulke E, Druffel T. Breakage of TiO2 agglomerates in electrostatically stabilized aqueous dispersions. Powder Technol 160;(2005):121–6.

[39]   Bagwe RP, Hilliard LR, Tan W. Surface Modification of Silica Nanoparticles to Reduce Aggregation andNonspecific Binding. Langmuir 22;(2006):4357–62.

[40]   Conde J, Dias JT, Grazù V, Moros M, Baptista P V., de la Fuente JM. Revisiting 30 years of biofunctionalization and surface chemistry of inorganic nanoparticles for nanomedicine. Front Chem 2;(2014).

[41]   Shoichet BK, Kobilka BK. Structure-based drug screening for G-protein-coupled receptors. Trends Pharmacol Sci 33;(2012):268–72.

[42]   Vega RB, Yang J, Rothermel BA, Bassel-Duby R, Williams RS. Multiple domains of MCIP1 contribute to inhibition of calcineurin activity. J Biol Chem 277;(2002):30401–7.

[43]   Hansen A, Eder A, B??nstrup M, Flato M, Mewe M, Schaaf S, et al. Development of a drug screening platform based on engineered heart tissue. Circ Res 107;(2010):35–44.

[44]   Aramburu J, Yaffe MB, López-Rodríguez C, Cantley LC, Hogan PG, Rao A. Affinity-driven peptide selection of an NFAT inhibitor more selective than cyclosporin A. Science (80-) 285;(1999):2129–33.

[45] Cheng Y, Xu Z, Ma M, Xu T. Dendrimers as drug carriers: Applications in different routes of drug administration. J Pharm Sci 97;(2008):123–43.

[46] Heyder J. Deposition of Inhaled Particles in the Human Respiratory Tract and Consequences for Regional Targeting in Respiratory Drug Delivery. Proc Am Thorac Soc 1;(2004):315–20.

[47] Berlin C.M. J, May-McCarver DG, Notterman DA, Ward RM, Weismann DN, Wilson GS, et al. Alternative routes of drug administration - Advantages and disadvantages (subject review). Pediatrics 100;(1997).

[48] Gaudana R, Ananthula HK, Parenky A, Mitra AK. Ocular Drug Delivery. AAPS J 12;(2010):348–60.

[49] Alexander NJ, Baker E, Kaptein M, Karck U, Miller L, Zampaglione E. Why consider vaginal drug administration? Fertil Steril 82;(2004):1–12.

[50] Cagnacci A, Ferrari S, Tirelli A, Zanin R, Volpe A. Route of administration of contraceptives containing desogestrel/etonorgestrel and insulin sensitivity: a prospective randomized study. Contraception 80;(2009):34–9.

[51] Belcon MC. Topical versus systemic antibiotics in the treatment of acute superficial skin infections. J Natl Med Assoc 71;(1979):63–4.

[52] Blanco E, Shen H, Ferrari M. Principles of nanoparticle design for overcoming biological barriers to drug delivery. Nat Biotechnol 33;(2015):941–51.

[53] Karamanidou T, Karidi K, Bourganis V, Kontonikola K, Kammona O, Kiparissides C. Effective incorporation of insulin in mucus permeating self-nanoemulsifying drug delivery systems. Eur J Pharm Biopharm 97;(2015):223–9.

[54] Tomlin M. Pharmacology & Pharmacokinetics. A basic reader. Springer Science & Business Media; (2009).

[55] Gary C. Rosenfeld DSL. Pharmacology. 4th ed. Lippincott Williams & Wilkins; (2007).

[56] Primeau AJ, Rendon A, Hedley D, Lilge L, Tannock IF. The distribution of the anticancer drug doxorubicin in relation to blood vessels in solid tumors. Clin Cancer Res 11;(2005):8782–8.

[57] Coleman MD, Wiley InterScience (Online service). Human drug metabolism : an introduction. Wiley-Blackwell; (2010).

[58] Juliano RL. The delivery of therapeutic oligonucleotides. Nucleic Acids Res 44;(2016):6518–48.

[59] Bruno BJ, Miller GD, Lim CS. Basics and recent advances in peptide and protein drug delivery. Ther Deliv 4;(2013):1443–67.

[60] Maeda H, Nakamura H, Fang J. The EPR effect for macromolecular drug delivery to solid tumors: Improvement of tumor uptake, lowering of systemic toxicity, and distinct tumor

imaging in vivo. Adv Drug Deliv Rev 65;(2013):71–9.

[61]   Kumari A, Yadav SK, Yadav SC. Biodegradable polymeric nanoparticles based drug delivery systems. Colloids Surfaces B Biointerfaces 75;(2010):1–18.

[62]   Hu L, Tang X, Cui F. Solid lipid nanoparticles (SLNs) to improve oral bioavailability of poorly soluble drugs. J Pharm Pharmacol 56;(2004):1527–35.

[63]   Barenholz Y. Doxil® - The first FDA-approved nano-drug: Lessons learned. J Control Release 160;(2012):117–34.

[64]   Medintz IL, Uyeda HT, Goldman ER, Mattoussi H. Quantum dot bioconjugates for imaging, labelling and sensing. Nat Mater 4;(2005):435–46.

[65]   Chatterjee DK, Diagaradjane P, Krishnan S. Nanoparticle-mediated hyperthermia in cancer therapy. Ther Deliv 2;(2011):1001–14.

[66]   Docter D, Westmeier D, Markiewicz M, Stolte S, Knauer SK, Stauber RH. The nanoparticle biomolecule corona: lessons learned - challenge accepted? Chem Soc Rev 44;(2015):6094–121.

[67]   Corbo C, Molinaro R, Parodi A, Toledano Furman NE, Salvatore F, Tasciotti E. The impact of nanoparticle protein corona on cytotoxicity, immunotoxicity and target drug delivery. Nanomedicine 11;(2016):81–100.

[68]   Caracciolo G, Farokhzad OC, Mahmoudi M. Biological Identity of Nanoparticles In Vivo: Clinical Implications of the Protein Corona. Trends Biotechnol 35;(2017):257–64.

[69]   Monopoli MP, Walczyk D, Campbell A, Elia G, Lynch I, Baldelli Bombelli F, et al. Physical-Chemical aspects of protein corona: Relevance to in vitro and in vivo biological impacts of nanoparticles. J Am Chem Soc 133;(2011):2525–34.

[70]   Cox A, Andreozzi P, Dal Magro R, Fiordaliso F, Corbelli A, Talamini L, et al. Evolution of Nanoparticle Protein Corona Across the Blood-Brain Barrier. ACS Nano (2018).

[71]   Kelly PM, Åberg C, Polo E, O'Connell A, Cookman J, Fallon J, et al. Mapping protein binding sites on the biomolecular corona of nanoparticles. Nat Nanotechnol 10;(2015):472–9.

[72]   Moyano DF, Saha K, Prakash G, Yan B, Kong H, Yazdani M, et al. Fabrication of corona-free nanoparticles with tunable hydrophobicity. ACS Nano 8;(2014):6748–55.

[73]   García KP, Zarschler K, Barbaro L, Barreto JA, O'Malley W, Spiccia L, et al. Zwitterionic-coated "stealth" nanoparticles for biomedical applications: Recent advances in countering biomolecular corona formation and uptake by the mononuclear phagocyte system. Small 10;(2014):2516–29.

[74]   Okuhata Y. Delivery of diagnostic agents for magnetic resonance imaging. Adv Drug Deliv Rev 37;(1999):121–37.

[75]   Sarin H. Physiologic upper limits of pore size of different blood capillary types and

another perspective on the dual pore theory of microvascular permeability. J Angiogenes Res 2;(2010).

[76] Fang J, Nakamura H, Maeda H. The EPR effect: Unique features of tumor blood vessels for drug delivery, factors involved, and limitations and augmentation of the effect. Adv Drug Deliv Rev 63;(2011):136–51.

[77] Cabral H, Matsumoto Y, Mizuno K, Chen Q, Murakami M, Kimura M, et al. Accumulation of sub-100 nm polymeric micelles in poorly permeable tumours depends on size. Nat Nanotechnol 6;(2011):815–23.

[78] Huang K, Ma H, Liu J, Huo S, Kumar A, Wei T, et al. Size-dependent localization and penetration of ultrasmall gold nanoparticles in cancer cells, multicellular spheroids, and tumors in vivo. ACS Nano 6;(2012):4483–93.

[79] Arami H, Khandhar A, Liggitt D, Krishnan KM. In vivo delivery, pharmacokinetics, biodistribution and toxicity of iron oxide nanoparticles. Chem Soc Rev 44;(2015):8576–607.

[80] Choi CHJ, Zuckerman JE, Webster P, Davis ME. Targeting kidney mesangium by nanoparticles of defined size. Proc Natl Acad Sci 108;(2011):6656–61.

[81] Shah S, Liu Y, Hu W, Gao J. Modeling Particle Shape-Dependent Dynamics in Nanomedicine. J Nanosci Nanotechnol 11;(2011):919–28.

[82] Campbell F, Bos FL, Sieber S, Arias-Alpizar G, Koch BE, Huwyler J, et al. Directing Nanoparticle Biodistribution through Evasion and Exploitation of Stab2-Dependent Nanoparticle Uptake. ACS Nano 12;(2018):2138–50.

[83] Walkey CD, Olsen JB, Song F, Liu R, Guo H, Olsen DWH, et al. Protein corona fingerprinting predicts the cellular interaction of gold and silver nanoparticles. ACS Nano 8;(2014):2439–55.

[84] Byrne JD, Betancourt T, Brannon-Peppas L. Active targeting schemes for nanoparticle systems in cancer therapeutics. Adv Drug Deliv Rev 60;(2008):1615–26.

[85] Danhier F, Feron O, Préat V. To exploit the tumor microenvironment: Passive and active tumor targeting of nanocarriers for anti-cancer drug delivery. J Control Release 148;(2010):135–46.

[86] Saraiva C, Praça C, Ferreira R, Santos T, Ferreira L, Bernardino L. Nanoparticle-mediated brain drug delivery: Overcoming blood-brain barrier to treat neurodegenerative diseases. J Control Release 235;(2016):34–47.

[87] Fiandra L, Mazzucchelli S, De Palma C, Colombo M, Allevi R, Sommaruga S, et al. Assessing the In Vivo Targeting Efficiency of Multifunctional Nanoconstructs Bearing Antibody-Derived Ligands. ACS Nano 7;(2013):6092–102.

[88] Anselmo AC, Mitragotri S. Impact of particle elasticity on particle-based drug delivery systems. Adv Drug Deliv Rev 108;(2017):51–67.

[89] Guo P, Liu D, Subramanyam K, Wang B, Yang J, Huang J, et al. Nanoparticle elasticity directs tumor uptake. Nat Commun 9;(2018).

[90] D'Emanuele A, Jevprasesphant R, Penny J, Attwood D. The use of a dendrimer-propranolol prodrug to bypass efflux transporters and enhance oral bioavailability. J Control Release 95;(2004):447–53.

[91] Vinciguerra D, Tran J, Nicolas J. Telechelic polymers from reversible-deactivation radical polymerization for biomedical applications. Chem Commun 54;(2018):228–40.

[92] Eloy JO, Claro de Souza M, Petrilli R, Barcellos JPA, Lee RJ, Marchetti JM. Liposomes as carriers of hydrophilic small molecule drugs: Strategies to enhance encapsulation and delivery. Colloids Surfaces B Biointerfaces 123;(2014):345–63.

[93] Chang HI, Yeh MK. Clinical development of liposome-based drugs: Formulation, characterization, and therapeutic efficacy. Int J Nanomedicine 7;(2012):49–60.

[94] Singh N, Karambelkar A, Gu L, Lin K, Miller JS, Chen CS, et al. Bioresponsive mesoporous silica nanoparticles for triggered drug release. J Am Chem Soc 133;(2011):19582–5.

[95] Gao Q, Xu Y, Wu D, Sun Y, Li X. pH-responsive drug release from polymer-coated mesoporous silica spheres. J Phys Chem C 113;(2009):12753–8.

[96] Mura S, Nicolas J, Couvreur P. Stimuli-responsive nanocarriers for drug delivery. Nat Mater 12;(2013):991–1003.

[97] Minchin R. Nanomedicine: Sizing up targets with nanoparticles. Nat Nanotechnol 3;(2008):12–3.

[98] Burns AA, Vider J, Ow H, Here E, Oula PM, Baumgart M, et al. Fluorescent silica nanoparticles with efficient urinary excretion for nanomedicine. Nano Lett 9;(2009):442–8.

[99] Kreyling WG, Abdelmonem AM, Ali Z, Alves F, Geiser M, Haberl N, et al. In vivo integrity of polymer-coated gold nanoparticles. Nat Nanotechnol 10;(2015):619–23.

[100] Panyam J, Labhasetwar V. Biodegradable nanoparticles for drug and gene delivery to cells and tissue. Adv Drug Deliv Rev 55;(2003):329–47.

[101] Park J-H, Gu L, von Maltzahn G, Ruoslahti E, Bhatia SN, Sailor MJ. Biodegradable luminescent porous silicon nanoparticles for in vivo applications. Nat Mater 8;(2009):331–6.

[102] Giner-Casares JJ, Henriksen-Lacey M, Coronado-Puchau M, Liz-Marzán LM. Inorganic nanoparticles for biomedicine: Where materials scientists meet medical research. Mater Today (2016).

[103] Jiao M, Zhang P, Meng J, Li Y, Liu C, Luo X, et al. Recent advancements in biocompatible inorganic nanoparticles towards biomedical applications. Biomater Sci 6;(2018):726–45.

[104] Choi SJ, Lee JK, Jeong J, Choy JH. Toxicity evaluation of inorganic nanoparticles:

Considerations and challenges. Mol Cell Toxicol (2013).

[105] Soenen SJ, Rivera-Gil P, Montenegro JM, Parak WJ, De Smedt SC, Braeckmans K. Cellular toxicity of inorganic nanoparticles: Common aspects and guidelines for improved nanotoxicity evaluation. Nano Today (2011).

[106] Choi HS, Liu W, Liu F, Nasr K, Misra P, Bawendi MG, et al. Design considerations for tumour-targeted nanoparticles. Nat Nanotechnol (2010).

[107] Olivier JC. Drug transport to brain with targeted nanoparticles. NeuroRx (2005).

[108] Gu FX, Karnik R, Wang AZ, Alexis F, Levy-Nissenbaum E, Hong S, et al. Targeted nanoparticles for cancer therapy. Nano Today (2007).

[109] Clark AJ, Davis ME. Increased brain uptake of targeted nanoparticles by adding an acid-cleavable linkage between transferrin and the nanoparticle core. Proc Natl Acad Sci U S A 112;(2015):12486–91.

[110] Farokhzad OC, Langer R. Impact of nanotechnology on drug delivery. ACS Nano (2009).

[111] Wiley DT, Webster P, Gale A, Davis ME. Transcytosis and brain uptake of transferrin-containing nanoparticles by tuning avidity to transferrin receptor. Proc Natl Acad Sci (2013).

[112] Bobo D, Robinson KJ, Islam J, Thurecht KJ, Corrie SR. Nanoparticle-Based Medicines: A Review of FDA-Approved Materials and Clinical Trials to Date. Pharm Res 33;(2016):2373–87.

[113] Ventola CL. Progress in Nanomedicine: Approved and Investigational Nanodrugs. P T 42;(2017):742–55.

[114] Beddoes CM, Case CP, Briscoe WH. Understanding nanoparticle cellular entry: A physicochemical perspective. Adv Colloid Interface Sci 218;(2015):48–68.

[115] Zhao J, Stenzel MH. Entry of nanoparticles into cells: The importance of nanoparticle properties. Polym Chem 9;(2018):259–72.

[116] Varkouhi AK, Scholte M, Storm G, Haisma HJ. Endosomal escape pathways for delivery of biologicals. J Control Release 151;(2011):220–8.

[117] Selby LI, Cortez-Jugo CM, Such GK, Johnston APR. Nanoescapology: progress toward understanding the endosomal escape of polymeric nanoparticles. Wiley Interdiscip Rev Nanomedicine Nanobiotechnology 9;(2017).

[118] Canton I, Battaglia G. Endocytosis at the nanoscale. Chem Soc Rev 41;(2012):2718–39.

[119] Hillaireau H, Couvreur P. Nanocarriers' entry into the cell: Relevance to drug delivery. Cell Mol Life Sci 66;(2009):2873–96.

[120] Benjaminsen R V., Mattebjerg MA, Henriksen JR, Moghimi SM, Andresen TL. The possible "proton sponge " effect of polyethylenimine (PEI) does not include change in lysosomal

pH. Mol Ther 21;(2013):149–57.

[121] Akinc A, Thomas M, Klibanov AM, Langer R. Exploring polyethylenimine-mediated DNA transfection and the proton sponge hypothesis. J Gene Med 7;(2005):657–63.

[122] Behr J. The proton sponge: a trick to enter cells the viruses did not exploit. Int J Chem 2;(1997):34–6.

[123] Vermeulen LMP, Brans T, Samal SK, Dubruel P, Demeester J, De Smedt SC, et al. Endosomal Size and Membrane Leakiness Influence Proton Sponge-Based Rupture of Endosomal Vesicles. ACS Nano 12;(2018):2332–45.

[124] White JM, Whittaker GR. Fusion of Enveloped Viruses in Endosomes. Traffic 17;(2016):593–614.

[125] Martens TF, Remaut K, Demeester J, De Smedt SC, Braeckmans K. Intracellular delivery of nanomaterials: How to catch endosomal escape in the act. Nano Today 9;(2014):344–64.

[126] Lönn P, Kacsinta AD, Cui XS, Hamil AS, Kaulich M, Gogoi K, et al. Enhancing Endosomal Escape for Intracellular Delivery of Macromolecular Biologic Therapeutics. Sci Rep 6;(2016).

[127] Wang Z, Luo M, Mao C, Wei Q, Zhao T, Li Y, et al. A Redox-Activatable Fluorescent Sensor for the High-Throughput Quantification of Cytosolic Delivery of Macromolecules. Angew Chemie - Int Ed 56;(2017):1319–23.

[128] Chao TY, Raines RT. Fluorogenic label to quantify the cytosolic delivery of macromolecules. Mol Biosyst 9;(2013):339–42.

[129] Verdurmen WPR, Mazlami M, Plückthun A. A quantitative comparison of cytosolic delivery via different protein uptake systems. Sci Rep 7;(2017).

[130] Erazo-Oliveras A, Muthukrishnan N, Baker R, Wang TY, Pellois JP. Improving the endosomal escape of cell-penetrating peptides and their cargos: Strategies and challenges. Pharmaceuticals 5;(2012):1177–209.

[131] Evans BC, Nelson CE, Yu SS, Beavers KR, Kim AJ, Li H, et al. Ex Vivo Red Blood Cell Hemolysis Assay for the Evaluation of pH-responsive Endosomolytic Agents for Cytosolic Delivery of Biomacromolecular Drugs. J Vis Exp (2013).

[132] Yessine MA, Leroux JC. Membrane-destabilizing polyanions: Interaction with lipid bilayers and endosomal escape of biomacromolecules. Adv Drug Deliv Rev 56;(2004):999–1021.

[133] Ong S, Liu H, Pidgeon C. Immobilized-artificial-membrane chromatography: Measurements of membrane partition coefficient and predicting drug membrane permeability. J. Chromatogr. A, vol. 728, (1996), p. 113–28.

[134] Levin VA. Relationship of Octanol/Water Partition Coefficient and Molecular Weight to Rat Brain Capillary Permeability. J Med Chem 23;(1980):682–4.

[135] Rothwell JA, Day AJ, Morgan MRA. Experimental determination of octanol-water partition coefficients of quercetin and related flavonoids. J Agric Food Chem 53;(2005):4355–60.

[136] Pope AJ, Haupts UM, Moore KJ. Homogeneous fluorescence readouts for miniaturized high-throughput screening: Theory and practice. Drug Discov Today 4;(1999):350–62.

[137] Wu PG, Brand L. Resonance Energy Transfer: Methods and Applications. Anal Biochem (1994).

[138] Clegg RM. Fluorescence resonance energy transfer. Curr Opin Biotechnol (1995).

[139] Hochreiter B, Garcia AP, Schmid JA. Fluorescent proteins as genetically encoded FRET biosensors in life sciences. Sensors (Switzerland) (2015).

[140] Griffin BA, Adams SR, Tsien RY. Specific covalent labeling of recombinant protein molecules inside live cells. Science (80-) 281;(1998):269–72.

[141] Martin BR, Giepmans BNG, Adams SR, Tsien RY. Mammalian cell-based optimization of the biarsenical-binding tetracysteine motif for improved fluorescence and affinity. Nat Biotechnol (2005).

[142] Adams SR, Tsien RY. Preparation of the membrane-permeant biarsenicals FlAsH-EDT2 and ReAsH-EDT2 for fluorescent labeling of tetracysteine-tagged proteins. Nat Protoc (2008).

[143] Cao H, Chen B, Squier TC, Mayer MU. CrAsH: A biarsenical multi-use affinity probe with low non-specific fluorescence. Chem Commun (2006).

[144] Larkin P. Infrared and Raman Spectroscopy. (2011).

[145] Lin-Vien D, Colthup NB, Fateley WG, Grasselli JG (Professor). The Handbook of infrared and raman characteristic frequencies of organic molecules. Academic Press; (1991).

[146] Henry SM, El-Sayed MEH, Pirie CM, Hoffman AS, Stayton PS. pH-responsive poly(styrene-alt-maleic anhydride) alkylamide copolymers for intracellular drug delivery. Biomacromolecules (2006).

[147] Savina A, Jancic C, Hugues S, Guermonprez P, Vargas P, Moura IC, et al. NOX2 Controls Phagosomal pH to Regulate Antigen Processing during Crosspresentation by Dendritic Cells. Cell (2006).

[148] Hughes LD, Rawle RJ, Boxer SG. Choose your label wisely: Water-soluble fluorophores often interact with lipid bilayers. PLoS One (2014).

[149] Furtado A, Henry R. Measurement of green fluorescent protein concentration in single cells by image analysis. Anal Biochem (2002).

[150] Peet JA. Quantification of the cytoplasmic spaces of living cells with EGFP reveals arrestin-EGFP to be in disequilibrium in dark adapted rod photoreceptors. J Cell Sci (2004).

[151] Fluorophores.org n.d.

[152] Spectra Database hosted at the University of Arizona n.d.

[153] Pomorski A, Adamczyk J, Bishop AC, Kre¸zel A. Probing the target-specific inhibition of sensitized protein tyrosine phosphatases with biarsenical probes. Org Biomol Chem (2015).

Appendix 1

The matlab code used to assess FRET efficiencies of different donor-acceptor pairs:

A_mega_main.m

```matlab
% Abs spectrum must be normalized to the same peak to which Ext coefficient
% is givin!!!
% define BGN_V before run!!!    (background noise)

% start fresh
    clc
   % clearvars

% define constants
    endogenous_player = 1;  % 1 for externaly administered donor, 2 for
acceptor. see generate_signal_map, calculating macro_transfer_energy
    n_acceptors = 1;
    emission_monochromator_band_width = 20;
    imposed_ex_min = 300;
    imposed_ex_max = 700;
    imposed_emission_min = 400;
    imposed_emission_max = 1000; % for no max set to 1000
    laser_wavelength = 0;  % if equal 0 - scan all wavelengths
    delivered_fraction = 0.1;   %input('delivery fraction (1-0):');
    R0_constant=0.217266;      % need to be determined using pairs with known
R0
    I0=1.025E+8;
    quenched_acceptor_fraction = 0;           %   reducing the noise from
acceptor Abs leak by adding a thiol cleavable quencher - see if/else in
generate_signal_map
    quenched_donor_fraction = 0;
    fluorophore_distance = 40;  % Angstrom

    %  define donor / acceptor concentrations, in Molar
    %  (clara apply 25ug/ml to cells, which is close to 0.126uM in micelle
concentration
    if endogenous_player == 1   %   external donor
        donor_concentration = 1E-6;
        minimum_acceptor_concentration = 5E-6;
        maximum_acceptor_concentration = 5E-6;
    end
    if endogenous_player == 2   %   external acceptor
        donor_concentration = 5E-6;
        minimum_acceptor_concentration = 1E-6;
        maximum_acceptor_concentration = 1E-6;
    end
  % load('background noise interpolated, 1M cells per ml, 3nm slit.mat');
    real_noise_interpolated=zeros(1000,1000);   % no real noise
% import data
    import_multiple_files;  % create one matrix with all

    %setup loop parameters to calcuate for different acceptor concentation
    acceptor_concentration = minimum_acceptor_concentration;
    i_concentration=1;
```

```matlab
    %   define log for each pair's maximum signal
    maximum_log = struct('SN', 0, 'donor', 'a', 'acceptor', 'a', 'max', 0,
'cell_number', 0, 'R0', 0, 'acceptor_abs_leak', 0, 'donor_emission_leak', 0,
'acceptor_concentration', 0, 'fluorophore_distance_A', 0,
'monochromator_band_width', 0, 'n_acceptors', 0, 'delivered_fraction', 0);

    %   define/reset signal map
    signal_map = zeros(1000, 1000, num_of_proteins*num_of_organic_dyes, 3);

    while acceptor_concentration <= maximum_acceptor_concentration

        i_protein = num_of_proteins;


        while i_protein>0
            j_organic=num_of_organic_dyes;
            while j_organic>0
                DQY = all_spectra(1010, 1, i_protein, 1);        % donor
quantum yield.
                AQY = all_spectra(1010, 1, j_organic, 2);        % acceptor
quantum yield
                DEC = all_spectra(1010, 2, i_protein, 1);        % donor
extinction coefficient
                AEC = all_spectra(1010, 2, j_organic, 2);        % acceptor
extinction coefficient
                donor=all_spectra(1:1000, 1:4, i_protein, 1);     % define
donor from all_spectra
                acceptor=all_spectra(1:1000, 1:4, j_organic, 2);  % define
acceptor from all_spectra

                maximum_log((i_protein-1)*num_of_organic_dyes+j_organic,
i_concentration).donor = protein_spectra_file_names(i_protein).name;
                maximum_log((i_protein-1)*num_of_organic_dyes+j_organic,
i_concentration).acceptor = organic_dye_spectra_file_names(j_organic).name;
                maximum_log((i_protein-1)*num_of_organic_dyes+j_organic,
i_concentration).SN = (i_protein-1)*num_of_organic_dyes+j_organic;
                maximum_log((i_protein-1)*num_of_organic_dyes+j_organic,
i_concentration).acceptor_concentration = acceptor_concentration;
                maximum_log((i_protein-1)*num_of_organic_dyes+j_organic,
i_concentration).fluorophore_distance_A = fluorophore_distance;
                maximum_log((i_protein-1)*num_of_organic_dyes+j_organic,
i_concentration).monochromator_band_width =
emission_monochromator_band_width;
                maximum_log((i_protein-1)*num_of_organic_dyes+j_organic,
i_concentration).n_acceptors = n_acceptors;
                maximum_log((i_protein-1)*num_of_organic_dyes+j_organic,
i_concentration).delivered_fraction = delivered_fraction;

                Aone_pair;

                disp((i_protein-1)*num_of_organic_dyes+j_organic);

                j_organic = j_organic-1;
            end
```

```matlab
            i_protein = i_protein-1;
        end


        acceptor_concentration = minimum_acceptor_concentration *
3^i_concentration;
        i_concentration = i_concentration+1;


        if minimum_acceptor_concentration == maximum_acceptor_concentration
        acceptor_concentration = maximum_acceptor_concentration *2;  %
meaning - break loop.
        end


    end
    clearvars real_noise_interpolated acceptor acceptor_Abs_leak all_spectra
cell number donor donor_emission_leak i_protein j_organic
macro_transfered_energy micro_transfered_energy no_spectrum_overlap R0
tep_signal_map pair_number temp_signal_map water_refractive_index unified
real_noise R0_constant max_signal k_squared cell_number;
    clearvars quenched_acceptor_fraction protein_spectra_file_names
organic_dye_spectra_file_names num_of_proteins num_of_organic_dyes
fluorophore_distance donor_concentration delivered_fraction
acceptor_concentration ;
    clearvars quenched_donor_fraction n_acceptors_micro_transfered_energy
n_acceptors minimum_acceptor_concentration maximum_acceptor_concentration;
    clearvars local_overlap laser_wavelength imposed_ex_min imposed_ex_max
imposed_emission_min imposed_emission_max i_em_sum i_concentration I0
endogenous_player emission_monochromator_band_width delta concentration_step
b a;
```

Aone_pair.m

```matlab
%   create a single matrix for both
%   the format of this unified matrix: (by column)
%   acceptor Abs coefficient ; donor Abs ; donor Em ; acceptor Abs ; acceptor
Em
unified = zeros(1000,5);
%extrapulate_donor_abs;
%extrapulate_acceptor_em;
%%
%   normalization of emission by energy  - total area equal quantum yield.
    sum_of_emission_donor = sum(donor(:,4), 'omitnan');
    sum_of_emission_acceptor = sum(acceptor(:,4), 'omitnan');

    temp_donor_em_norm = (donor(:, 4) * DQY / sum_of_emission_donor) ;
    temp_acceptor_em_norm = (acceptor(:, 4) * AQY / sum_of_emission_acceptor)
;

%   copy to unified matrix
    copy_norm_em_to_unified;


%   delete variables
```

```matlab
    clearvars sum_of_emission_donor sum_of_emission_acceptor donor_em_norm
acceptor_em_norm temp_donor_em_norm temp_acceptor_em_norm;
%%


%%
%   normalization of Abs by Concentration and Extinction coefficient
    temp_donor_Abs_norm = (donor(:,2) * DEC * donor_concentration);
    temp_acceptor_Abs_norm = (acceptor(:,2) * AEC * acceptor_concentration);

%   calculation of absorbed energy fraction
    temp_donor_Abs_energy = (I0-I0*10.^(-1*temp_donor_Abs_norm));
    temp_acceptor_Abs_energy = (I0-I0*10.^(-1*temp_acceptor_Abs_norm));

%   copy to unified matrix
    copy_norm_Abs_to_unified;

%   copy Extinction coefficient to unified
    temp_acceptor_ext_coef = acceptor(:,2) * AEC;
    copy_extinction_coefficient_to_unified;

%     % tricky part, usefull for transfered energy calculation
%     temp_transferable_abs = donor(:,2) * DEC *
(acceptor_concentration*delivered_fraction);
%     temp_transferable_energy = =(1-10.^(-1*temp_transferable_abs))
%     copy_transferable_energy_to_unified;

    unified(isnan(unified))=0;  % change all NaN to 0
    %close_WL_gap;  %for some problematic spectras, with only even number
wavelengths
    % calculate R0 for this pair.
    calculate_R0;

%   delete variables
    clearvars temp_donor_Abs_norm temp_acceptor_Abs_norm
temp_donor_Abs_energy temp_acceptor_Abs_energy temp_acceptor_ext_coef;
    clearvars  DQY AQY AEC DEC acceptor_abs_at_wl donor_em_at_wl
temp_donor_ext_coef;
    %%

    generate_signal_map;
    %  add results to log
    %  the calculation ((i_protein-1)*j_organic+j_organic), gives the "pair"
serial number
        maximum_log((i_protein-1)*num_of_organic_dyes+j_organic,
i_concentration).R0 = R0;

    if no_spectrum_overlap==1
        maximum_log((i_protein-1)*num_of_organic_dyes+j_organic,
i_concentration).max = max_signal;
        maximum_log((i_protein-1)*num_of_organic_dyes+j_organic,
i_concentration).donor_emission_leak = donor_emission_leak;
        maximum_log((i_protein-1)*num_of_organic_dyes+j_organic,
i_concentration).acceptor_abs_leak = acceptor_Abs_leak;
        maximum_log((i_protein-1)*num_of_organic_dyes+j_organic,
i_concentration).cell_number = cell_number;
```

```
        end


    clearvars  spectral_overlap wl_index;
```

calculate_R0.m

```
water_refractive_index = 1.334;  % this is actually a function of wavelength,
but only change ~1% in relevent spectrum
k_squared = 0.666666;            % dipole orientation factor, ranging from 0-
4. this is a value for two free rotating dipoles.
spectral_overlap = 0;

wl_index=1;                             % wavelength index
while wl_index<1001
    donor_em_at_wl = unified(wl_index, 3);
    acceptor_abs_at_wl = unified(wl_index, 1);
    spectral_overlap = spectral_overlap +
donor_em_at_wl*acceptor_abs_at_wl*(wl_index.^4);    % unified(:, 1) is the
acceptor ext coefficient
    wl_index=wl_index+1;
end

R0 = R0_constant*(spectral_overlap * k_squared /
water_refractive_index.^4).^(1/6); % the QY is already multiplied by the
emission (emission total area is equal QY)
```

check_if_define_for_all.m

```
% this script checks if Abs/Em spectrum of both fluorophores are defined,
% at Abs/Em +/-4
local_overlap=0;
if unified(ex-1, 2)>0 && unified(ex+1, 2)>0
    if unified(ex-1, 4)>0 && unified(ex+1, 4)>0
        if unified(em-delta, 3)>0 && unified(em+delta, 3)>0
            if unified(em-delta, 5)>0 && unified(em+delta, 5)>0
                local_overlap=1;
            end
        end
    end
end
```

copy_extinction_coefficient_to_unified.m

```
d = size(temp_acceptor_ext_coef);
l = 1;
```

```
while l<=d(1,1)
    if acceptor(l,1)>0
        unified((acceptor(l,1)), 1) = temp_acceptor_ext_coef(l);
    end
    l=l+1;
end

clearvars l d;
```

copy_norm_Abs_to_unified.m

```
l = 1;
d = size(temp_acceptor_Abs_energy); % length of array (exceeding couse an
error)
while l<=d(1,1)
    if acceptor(l,1)>0
        unified((acceptor(l,1)), 4) = temp_acceptor_Abs_energy(l);
    end
    l=l+1;
end

l = 1;
d = size(temp_donor_Abs_energy); % length of array (exceeding couse an error)
while l<=d(1,1)
    if donor(l,1)>0
        unified((donor(l,1)), 2) = temp_donor_Abs_energy(l);
    end
    l=l+1;
end

clearvars l d;
```

copy_norm_em_to_unified.m

```
l = 1;
d = size(temp_acceptor_em_norm); % length of array (exceeding couse an error)

while l<=d(1,1)   % the first condition is redundant
    if acceptor(l,3)>0
        unified((acceptor(l,3)), 5) = temp_acceptor_em_norm(l);
    end
    l=l+1;
end

l = 1;
d = size(temp_donor_em_norm);
```

```matlab
while l<=d(1,1)
    if donor(l,3)>0
        unified((donor(l,3)), 3) = temp_donor_em_norm(l);
    end
    l=l+1;
end

clearvars l d;
```

copy_transferable_energy_to_unified.m

```matlab
d=size(temp_transferable_energy);
l=1;

while l<=d(1,1)
    if donor(l,1)>0
        unified((donor(l,1)), 6) = temp_transferable_energy(l);
    end
    l=l+1;
end

clearvars l d;
```

generate_signal_map.m

```matlab
ex=imposed_ex_min;
delta = floor(emission_monochromator_band_width/2); %equal half the
bandwidth, round down
micro_transfered_energy = (1/(1+(fluorophore_distance/R0).^6));
n_acceptors_micro_transfered_energy = n_acceptors * micro_transfered_energy /
(1+(n_acceptors-1)*micro_transfered_energy); %assuming more than one acceptor
per donor, equation taken fro the article: Strength in Numbers: Effects of
Acceptor Abundance on FRET Efficiency, chemphyschem,
http://onlinelibrary.wiley.com/doi/10.1002/cphc.201000568/full
no_spectrum_overlap = -1;  %  assuming no spectrum overlap

if laser_wavelength==0
    while ex<999 && ex<imposed_ex_max;
        ex=ex+1;
        em = imposed_emission_min;
        if em < ex+20
            em=ex+20;
        end

        while em<999 && em<imposed_emission_max

            em=em+1;
```

```matlab
                check_if_define_for_all;
                if local_overlap==1
                    no_spectrum_overlap = 1; %meaning - overlap WAS found.

                    % extract relevent data from unified, average over 3
wavelengths
                    %%
                    donor_em_fraction = 0;
                    i_em_sum = -1*delta;
                    while(i_em_sum<delta+1)
                        donor_em_fraction = donor_em_fraction +
unified(em+i_em_sum, 3);
                        i_em_sum = i_em_sum+1;
                    end
                    if donor_em_fraction<0
                        donor_em_fraction=0;
                    end
                    donor_energy = (unified(ex+1, 2) + unified(ex, 2) +
unified(ex-1, 2));        % before FRET
                    %%


                    %%
                    acceptor_em_fraction = 0;
                    i_em_sum = -1*delta;
                    while(i_em_sum<delta+1)
                        acceptor_em_fraction = acceptor_em_fraction +
unified(em+i_em_sum, 5);
                        i_em_sum = i_em_sum+1;
                    end
                    acceptor_energy = (unified(ex+1, 4) + unified(ex, 4) +
unified(ex-1, 4));      % before FRET
                    if acceptor_energy<0
                        acceptor_energy=0;
                    end
                     %%
                    % calculate transfered energy
                    if(endogenous_player == 1)    % the donor is external and needs
to escape endosome
                        macro_transfered_energy =
n_acceptors_micro_transfered_energy * delivered_fraction * donor_energy;
                    else if (endogenous_player == 2)    % the acceptor is the
externaly adinistered player, and need to escape the endosome
                            macro_transfered_energy = (donor_energy /
donor_concentration) * micro_transfered_energy * acceptor_concentration *
delivered_fraction * n_acceptors;    % article: Strength in Numbers: Effects
of Acceptor Abundance on FRET Efficiency, chemphyschem,
http://onlinelibrary.wiley.com/doi/10.1002/cphc.201000568/full
                        else return;
                        end
                    end


                % final result, representing the signal of a specific Ex and
Em wavelengths
```

```matlab
                nominator = real_noise_interpolated(em,ex) +
(donor_em_fraction * (donor_energy * (1-quenched_donor_fraction) -
macro_transfered_energy) + acceptor_em_fraction * ((1-
quenched_acceptor_fraction) * acceptor_energy + macro_transfered_energy));
                denominator = real_noise_interpolated(em,ex) +
(donor_em_fraction * donor_energy * (1-quenched_donor_fraction) + (1-
quenched_acceptor_fraction) * acceptor_em_fraction * acceptor_energy);


                signal_map(ex, em, (i_protein-
1)*num_of_organic_dyes+j_organic, i_concentration) = nominator / denominator;
% excitation in the y axis...



            end
        end
    end
else
    ex=laser_wavelength;
    em = imposed_emission_min;
        if em < ex+20
            em=ex+20;
        end

    while em<999 && em<imposed_emission_max

        em=em+1;
        check_if_define_for_all;
        if local_overlap==1
            no_spectrum_overlap = 1; %meaning - overlap WAS found.

            % extract relevent data from unified, average over 3
wavelengths
            %%
            donor_em_fraction = 0;
            i_em_sum = -1*delta;
            while(i_em_sum<delta+1)
                donor_em_fraction = donor_em_fraction +
unified(em+i_em_sum, 3);
                    i_em_sum = i_em_sum+1;
            end
            if donor_em_fraction<0
                donor_em_fraction=0;
            end
            donor_energy = (unified(ex+1, 2) + unified(ex, 2) +
unified(ex-1, 2));       % before FRET
            %%


            %%
            acceptor_em_fraction = 0;
            i_em_sum = -1*delta;
            while(i_em_sum<delta+1)
                acceptor_em_fraction = acceptor_em_fraction +
unified(em+i_em_sum, 5);
                    i_em_sum = i_em_sum+1;
            end
```

```matlab
                acceptor_energy = (unified(ex+1, 4) + unified(ex, 4) +
unified(ex-1, 4));    % before FRET
                if acceptor_energy<0
                    acceptor_energy=0;
                end
                 %%
                % calculate transfered energy
                macro_transfered_energy = n_acceptors_micro_transfered_energy
* delivered_fraction * donor_energy;
%(acceptor_concentration/donor_concentration);



                % final result, representing the signal of a specific Ex and
Em wavelengths

                nominator = real_noise_interpolated(em,ex) +
(donor_em_fraction * (donor_energy * (1-quenched_donor_fraction) -
macro_transfered_energy) + acceptor_em_fraction * ((1-
quenched_acceptor_fraction) * acceptor_energy + macro_transfered_energy));
                denominator = real_noise_interpolated(em,ex) +
(donor_em_fraction * donor_energy * (1-quenched_donor_fraction) + (1-
quenched_acceptor_fraction) * acceptor_em_fraction * acceptor_energy);

                signal_map(ex, em, (i_protein-
1)*num_of_organic_dyes+j_organic, i_concentration) = nominator / denominator;
% excitation in the y axis...


            end
        end
end


temp_signal_map = signal_map(:,:,(i_protein-1)*num_of_organic_dyes+j_organic,
i_concentration);  % current signal map
[max_signal, cell_number] = max(temp_signal_map(:));

if no_spectrum_overlap==1 %meaning - there WAS overlap (no overlap = -1)
    calculate_noise_contribution;
end



% clear variables
clearvars ex em donor_em_fraction donor_energy acceptor_em_fraction
acceptor_energy nominator denominator;
```

import_multiple_files.m

```matlab
%% import donor spectra
disp('select donor spectra folder')
fluorophore_type = 1;            % protein = 1, organic dye = 2
```

```matlab
spectra_dir = uigetdir;                                              % user
select dir
full_path_all_files = fullfile(spectra_dir, '*.*');                  %
add *.* to dir path
temp_file_names = dir (full_path_all_files);
% get file list, with some junk at top
protein_spectra_file_names = temp_file_names(3:end, 1);
% get rid of the junk
clearvars temp_file_names full_path_all_files;

raw_size = size(protein_spectra_file_names);        % the function size
return a vector, i need just the first number
num_of_spectra = raw_size(1,1);                                      % this
would be used for the next loop, importing the files
clearvars raw_size;
num_of_proteins=num_of_spectra;      % a global variable to be used by other
functions

all_spectra = zeros(1010, 4, num_of_spectra, 2);                    %
(protein/dye, specific dye/protein (equal num_of_spectra, x,y of each
spectrum
% protein = 1;
% organic_dye = 2;

while num_of_spectra>0
    spectra_path_and_name = fullfile(spectra_dir,
protein_spectra_file_names(num_of_spectra).name); % creating a full path name
for the import function
    temp_spectra = importfile(spectra_path_and_name);     % import spectra

    temp_spectra(1010,1:2) =
str2num(protein_spectra_file_names(num_of_spectra).name(end-14:end-4));   %
over size matrix to ensure dimentions matching with all_spectra
    temp_spectra(1010,2) = temp_spectra(1010,2)*1000;
    all_spectra(:, :, num_of_spectra, fluorophore_type) = temp_spectra; %
adding imported spectra to list

    num_of_spectra=num_of_spectra-1;
end

clearvars full_path_all_files fluorophore_type num_of_spectra spectra_dir
temp_full_path_name spectra_path_and_name temp_spectra
%%

%% import acceptor spectra
disp('select acceptor spectra folder')
fluorophore_type = 2;           % protein = 1, organic dye = 2
spectra_dir = uigetdir;                                              % user
select dir
full_path_all_files = fullfile(spectra_dir, '*.*');                  %
add *.* to dir path
temp_file_names = dir (full_path_all_files);
% get file list, with some junk at top
organic_dye_spectra_file_names = temp_file_names(3:end, 1);
% get rid of the junk
```

```matlab
clearvars temp_file_names full_path_all_files;

raw_size = size(organic_dye_spectra_file_names);         % size return a
vector, i need just the first number
num_of_spectra = raw_size(1,1);                                    % this
would be used for the next loop, importing the files
clearvars raw_size;
num_of_organic_dyes=num_of_spectra;      % a global variable to be used by
other functions

while num_of_spectra>0
    spectra_path_and_name = fullfile(spectra_dir,
organic_dye_spectra_file_names(num_of_spectra).name); % creating a full path
name for the import function
    temp_spectra = importfile(spectra_path_and_name);      % import spectra

    temp_spectra(1010,1:2) =
str2num(organic_dye_spectra_file_names(num_of_spectra).name(end-12:end-4));
% over size matrix to ensure dimentions matching with all_spectra
    temp_spectra(1010,2) = temp_spectra(1010,2)*1000;

    all_spectra(:, :, num_of_spectra, fluorophore_type) = temp_spectra; %
adding imported spectra to list

    num_of_spectra=num_of_spectra-1;
end

clearvars fluorophore_type num_of_spectra spectra_dir spectra_path_and_name
temp_spectra
%%
```

plot_signal_map.m

```matlab
mesh (signal_map(:,:));    % Excitation on the Y axis
%axis([(acceptor(1,3)-20), 820, (donor(1,1)-20), 820, 0.9, inf]);
xlabel('Emission wavelength [nm]');
ylabel('Excitation wavelength [nm]');
disp('1');
```

importfile.m

```matlab
function acceptor = importfile(filename, startRow, endRow)
```

```matlab
%IMPORTFILE Import numeric data from a text file as a matrix.
%   ACCEPTOR = IMPORTFILE(FILENAME) Reads data from text file FILENAME for
%   the default selection.
%
%   ACCEPTOR = IMPORTFILE(FILENAME, STARTROW, ENDROW) Reads data from rows
%   STARTROW through ENDROW of text file FILENAME.
%
% Example:
%   acceptor = importfile('acceptor.csv', 2, 242);
%
%    See also TEXTSCAN.

% Auto-generated by MATLAB on 2016/02/24 17:53:40

%% Initialize variables.
delimiter = ';';
if nargin<=2
    startRow = 2;
    endRow = inf;
end

%% Format string for each line of text:
%   column1: double (%f)
%   column2: double (%f)
%   column3: double (%f)
%   column4: double (%f)
% For more information, see the TEXTSCAN documentation.
formatSpec = '%f%f%f%f%[^\n\r]';

%% Open the text file.
fileID = fopen(filename,'r');

%% Read columns of data according to format string.
% This call is based on the structure of the file used to generate this
% code. If an error occurs for a different file, try regenerating the code
% from the Import Tool.
dataArray = textscan(fileID, formatSpec, endRow(1)-startRow(1)+1,
'Delimiter', delimiter, 'EmptyValue' ,NaN,'HeaderLines', startRow(1)-1,
'ReturnOnError', false);
for block=2:length(startRow)
    frewind(fileID);
    dataArrayBlock = textscan(fileID, formatSpec, endRow(block)-
startRow(block)+1, 'Delimiter', delimiter, 'EmptyValue' ,NaN,'HeaderLines',
startRow(block)-1, 'ReturnOnError', false);
    for col=1:length(dataArray)
        dataArray{col} = [dataArray{col};dataArrayBlock{col}];
    end
end

%% Close the text file.
fclose(fileID);

%% Post processing for unimportable data.
% No unimportable data rules were applied during the import, so no post
% processing code is included. To generate code which works for
```

```
% unimportable data, select unimportable cells in a file and regenerate the
% script.

%% Create output variable
acceptor = [dataArray{1:end-1}];
```

Instruction for spectra file formatting compatible with this code:

file name:

"name" "quantum yield" "extinction coefficient".csv

Example:

"alexa 488 0.92 00072.csv"

Name: alexa 488

Quantum yield: 0.92

Extinction coefficient: 72000 cm^{-1}M^{-1}

----

name - unlimited, as variable extraction is done from end of name.

quantum yield - using 0.## format

extinction coefficient - using ##### format, with leading zeros. this is the coefficient devided by 1000. so 270K would be 00270.

----

spectra must be normalized to the wavelength of the extinction coefficient (absorption at that wavelength must be equal to 1 in the file)

best way to edit files:

edit files in excel to look like this:

	A	B	C	D
1	Wavelength Abs	FlAsH (Adams) (EX)	Wavelength Em	FlAsH (Adams) (EM)
2	300	0.188	482	0.001
3	301	0.194	483	0.001
4	302	0.202	484	0.001
5	303	0.208	485	0.001
6	304	0.217	486	0.001
7	305	0.222	487	0.002
8	306	0.227	488	0.002
9	307	0.235	489	0.003
10	308	0.239	490	0.004
11	309	0.244	491	0.005
12	310	0.248	492	0.006
13	311	0.25	493	0.007
14	312	0.253	494	0.009
15	313	0.254	495	0.012
16	314	0.254	496	0.014
17	315	0.254	497	0.019
18	316	0.255	498	0.031
19	317	0.256	499	0.071
20	318	0.252	500	0.096

	A	B	C	D
216	514	0.891	696	0.005
217	515	0.853	697	0.005
218	516	0.806	698	0.005
219	517	0.752	699	0.004
220	518	0.7	700	0.005
221	519	0.644		
222	520	0.587		
223	521	0.527		
224	522	0.476		
225	523	0.423		

249	547	0.008		
250	548	0.007		
251	549	0.006		
252	550	0.005		
253				
254				

Than import to matlab as a table, and export as .csv file using

writetable(flash, 'Flash.csv', 'Delimiter', ';')